UNIVERSITY OF TWENTE

MASTER'S THESIS

Hydrodynamic Forces Acting on Vertically Rising Bubbles

Author:
Swen VAN DEN HEUVEL

Committee:
Prof. Dr. Ir. Wilko ROHLFS
Ir. Maarten BOTMAN
Dr. Ir. Jim KOK
Dr. Ir. Vatsal SANJAY

A thesis submitted in fulfilment of the requirements for the degree of Master of Science

in the

Engineering Technology
Mechanical Engineering

September 14, 2023

UNIVERSITY OF TWENTE

Abstract

Engineering Technology
Thermal and Fluid Engineering

Master of Science

Hydrodynamic Forces Acting on Vertically Rising Bubbles

by Swen VAN DEN HEUVEL

The physics involved with bubbles cover a vast range of different phenomena, ranging from the creation and merging of bubbles to their eventual break-up and the many different rising paths a (pair of) bubble(s) may take. Therefore, two literature studies were initially carried out. The first literature study focused on bubble generation, coalescence (the merging of two bubbles into a larger one), break-up and the effect of surfactants on these several phenomena. This study was carried out to form a basic understanding and for scoping purposes, narrowing down the subjects to be covered. It can be found in Appendix A.

The second literature study of Chapter 1 goes into depth about the physics of one or two air bubbles rising in water, following the general subject of this thesis. If the diameter of a single bubble exceeds a critical value ($\sim$ 1.8 mm [1]), a zigzagging or spiralling motion instead of straight rise can be seen. Although the existence of this so-called path instability has been known for centuries, a consensus on its exact workings has not yet been achieved. With the addition of a second bubble, interactions between the two bubbles may occur at significantly smaller sizes. Depending on the size and distance between the bubbles, side-by-side rise (horizontal bubble alignment) or in-line rise (vertical alignment) can both lead to attraction or repulsion between the bubble pair. Whereas an equilibrium distance, where the repelling and attractive force nullify each other, has experimentally and numerically been proven to exist for side-by-side bubble rise, the presence of such a distance for in-line rise is still a topic for debate.

The literature covered in Chapter 1 lays a foundation for the material discussed in the subsequent chapters. Chapter 2 thoroughly discusses single stable bubble rise. The terminal rise velocity of a single bubble can be of great importance, as it can be used to assess the performance of industrial processes employing bubbles, such as bubble column reactors or heat exchangers. By utilising a force balance to retain an understanding of the involved physics on a fundamental level, the terminal rise velocity of a bubble will be determined. The ability of the force balance to correctly model the rise velocity will be validated by literature and simulations carried out in Basilisk. Moreover, Basilisk is used to gather insight into the acceleration phase of bubbles. Since experimental data is scarce due to the small timescales involved, creating a continuous rise velocity during these early stages of a bubble's life through simulation is of great assistance. The results show that the terminal rise velocity can accurately be determined by employing force balances. Furthermore, the rise velocity in the acceleration regime of bubbles with diameters between $\sim$ 0.5 mm and $\sim$ 1.5 mm shows good agreement with the simulated behaviour. As the current study only focuses on air bubbles rising in water due to buoyancy, the scope of the research can be extended. Verifying whether the derived expressions also hold for several other standard bubble systems can be of interest for further studies.

Following the topic discussed in the second literature study, Chapter 3 dives deeper into the side-by-side rising configuration. The theoretical modification of the drag force, added mass and lift force with the introduction of the second bubble are covered. The different types of

bubble interaction are analysed qualitatively for a variety of Reynolds numbers with the help of Basilisk. Side-by-side bubble rise at Re $\lesssim$ 10 yields higher rise velocities than observed for a single bubble, for which the exact underlying phenomenon causing this behaviour is not yet well understood. The simulations for a bubble pair with Re $\sim$ 1 at terminal velocity show two interesting phenomena: 1) the pressure evolution is substantially different than at higher Reynolds numbers and 2) although the bubble rise velocity is 2.5 times lower compared to a bubble pair with Re $\sim$ 13, the upward fluid velocity through the bubble gap caused by vorticity interactions is slightly larger. While it is not apparent whether the above findings are a result or a cause of the higher rise velocity for a bubble pair compared to a single bubble, they are intriguing observations that may serve as a starting point for future research.

Contents

Chapter 1

Literature Study: Bubble Rise Behaviour and Bubble Interactions

This literature study focuses on the rise behaviour of single bubbles and bubble pairs. While small bubbles follow a straight rising path, bubbles above a critical diameter undergo a path instability, leading to a zigzagging or helical spiralling motion. The existence of such an instability has been known for centuries, as it was first noticed by Leonardo da Vinci in the 1500s [2], being deemed 'Leonardo's paradox' [3]. Even 500 years later, the exact workings of the path instability remain incredibly difficult, where a variety of explanations over the last decades are elaborated.

Since large bubble groups are often applied in industrial processes (such as in heat exchangers and bubble column reactors to enhance heat and mass transfer [2, 4, 5]), the interaction between two bubbles is also of interest. Therefore, side-by-side and in-line rise will be investigated, in which the properties of the fluid and the bubbles can lead to attraction or repulsion. The underlying physics for both mechanisms will be explained, while the existence of an equilibrium position for both configurations is investigated as well.

1.1 Introduction

In this literature study, bubble rise and bubble interactions will be investigated. When considering a singular bubble rising due to buoyancy, the bubble can either follow a rectilinear rise path or an oscillatory path above a certain critical bubble diameter. In addition to single bubble rise, bubble interactions in a side-by-side and in-line rising configuration will be treated as well. Depending on the properties of the bubble and the surrounding fluid, the bubble pair might show repulsive or attractive behaviour, of which the latter may lead to coalescence. The subsequent report (Chapter 2) will elaborate on the force balances acting on single bubbles below the path instability threshold at the terminal rise velocity and during its acceleration phase. The material described here can be seen as supplementary to that covered in Chapters 2 & 3.

1.2 Single Bubble Rise

The simplest case of bubble rise is a single bubble rising solely due to buoyancy. Even though only a single bubble is rising, it might follow a variety of paths depending on its size. The mechanisms leading to the different types of rise behaviour will be elaborated below by considering several regimes of the Bond and Galilei numbers. These dimensionless numbers describe the ratio of the gravitational force to the surface tension force and the ratio of the gravitational force to the viscous force, respectively.

1.2.1 Path Instability

At low Bond $\left(\mathrm{Bo} = \frac{\Delta\rho g D_\mathrm{b}^2}{\sigma}\right)$ and Galilei $\left(\mathrm{Ga} = \frac{\rho_\mathrm{L}\sqrt{g D_\mathrm{b}} D_\mathrm{b}}{\mu_\mathrm{L}}\right)$ numbers (where $\Delta\rho$ gives the density difference between both fluids, g the gravitational acceleration, D_b the bubble diameter, σ the surface tension, ρ_L the density of the liquid and μ_L the dynamic viscosity of the liquid), the surface tension of the bubble is significantly higher than the gravitational forces, such that the bubble keeps its integrity and takes a spherical or ellipsoidal shape [6]. Experiments from Duineveld [7] using 'hyper clean' water showed that rising air bubbles in water follow a rectilinear path for diameters up to approximately 1.8 mm. The water in his experiments was cleaned by a purification system to eliminate the effect of impurities (contaminants such as surfactants) on the rise velocity [7].

Once the critical diameter is surpassed, bubbles will not follow a rectilinear path anymore. Instead, either a zigzagging path or a spiralling path will be taken by the bubble, which was first noticed by Leonardo da Vinci in the 1500s [6]. Prosperetti [3] deemed this 'Leonardo's paradox', as it was not known at the time why an axisymmetric bubble would suddenly change its straight rising path to a spiralling or a zigzagging path. At the transition point, a path instability occurs, which, even to this day, is not understood well. Initially, based on the work of Haberman & Morton [8] in the 1950s, it was believed that vortex shedding from the bubble was the cause of the path instability [6, 7, 9]. They substantiated this by the fact that such vortex shedding has also been observed experimentally for rigid spheres at the same magnitude of Reynolds numbers as for bubbles [8, 10].

In the same period, Saffman [11] suggested the existence of a wake behind the bubble and that the instability of the rectilinear motion might trigger instability of the wake [12]. This notion was further investigated by Mougin & Magnaudet [12] and De Vries et al. [13] in the 2000s, revealing that a wake instability leading to a double-threaded wake is the primary cause of the path instability instead of vortex shedding. The two threads of the double-threaded wake have opposite circulation, creating a lift force [3]. This lift force, acting normal to the direction of motion, then causes the bubble to follow a curved/zigzag path [13].

In the last few years, additional mechanisms have been proposed. Cano-Lozano et al. [14] discovered a chaotic regime in 2016, in which bubbles experience small horizontal displacements. Interestingly, no standing eddy (a recirculation zone behind the bubble [9]) exists at the back of the bubble in the chaotic regime. This observation is in contrast to what was earlier described by Legendre et al. [15] and Leal [16], who state there are strong indications that the formation of a standing eddy is required for the occurrence of a wake instability. Since such a standing eddy was not observed, the path instability had to be seen as an outcome due to an interplay between the bubble and the surrounding flow [14].

In 2023, Herrada & Eggers [1] continued this way of thought and presented the first quantitative agreement between a numerical technique and high-precision measurements of the instability. At a critical diameter of 0.926 mm, a Hopf bifurcation[1] could be seen, causing instability of the bubble. As the bubble undergoes a periodic tilt, the side of the bubble pointing up possesses a higher degree of curvature. This increased curvature causes an increase in surface vorticity, leading to a higher rising velocity. The difference in rise velocities then causes the tilt of the bubble. By Bernoulli's law, an increased fluid velocity leads to a decreased pressure at the side of the bubble with high curvature, pushing the bubble back to its original position. The pushing back of the bubble causes a reversal of the distribution of curvature, leading to the repeating process of the zigzagging motion [1].

The publication from Herrada & Eggers [1], however, led to a response from Bonnefis et al. [18] merely a week later, stating that "some previously established results were overlooked or misinterpreted" by Herrada & Eggers [1]. It is stated that "the instability mechanism actually at play results from the hydrodynamic fluid-body coupling made possible by the unconstrained motion of the bubble which behaves essentially, in the relevant size range, as a rigid, nearly spheroidal body on the surface of which water slips freely" [18].

While a single instability causes the existence of a zigzag path, it was hypothesised by De Vries [9] that a spiralling or helical motion occurs due to a second instability of the zigzagging path. When this instability does not take place in the same plane as the already occurring zigzag, it is likely that a helical motion results. Similar to that of the zigzagging bubble, the double-threaded wake of a spiralling bubble consists of two counter-rotating vortex filaments, leading to a lift force on the bubble. This wake-induced lift force is directed towards the middle of the spiralling path, conserving the spiralling motion [9]. In addition, Mougin & Magnaudet [12] carried out simulations in which a zigzag path was always seen first as its growth rate is significantly larger than that of a spiral, corresponding s with experimental observations, while the reverse transition has not yet been reported [19].

1.2.2 Experimental and Numerical Results from Literature

A substantial amount of experimental and numerical research has been performed on single bubble rise, where Haberman & Morton [8] carried out the first modern study, distinguishing three different paths: rectilinear, spiral and straight rocking (later often deemed zigzagging) [14]. This initial work has led to many subsequent studies, amongst which by Tripathi et al. [6], who carried out a three-dimensional numerical analysis on an initially spherical bubble rising from rest. They describe that the boundaries between the different regimes generally agree well with experimental studies [8, 20–22]. Their overview can be seen in Figure 1.1, where five different regions are shown. It should be noted that the Galilei and Bond numbers shown in the figure are based on the radius instead of the diameter, which is used in the rest of the report. Therefore, Ga and Bo based on the diameter have to be divided by $2\sqrt{2}$ and 4, respectively, to achieve Ga and Bo based on the radius.

[1] A Hopf bifurcation is the development of a periodic oscillation as a parameter (in this case the bubble diameter) crosses a critical value [17].

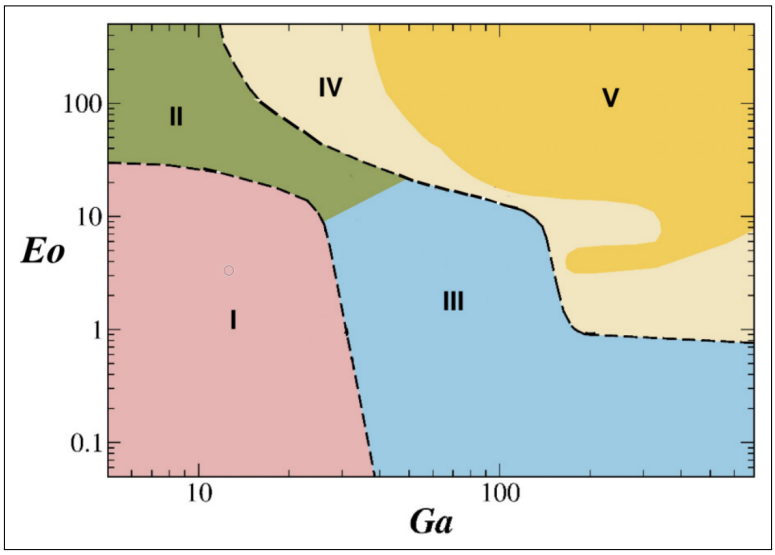

FIGURE 1.1: The different regimes for bubbles during rise as defined by Tripathi et al. [2] as a function of the Galilei and Eötvös (Bond) number (based on the bubble radius). Region I: axisymmetric, region II: skirted, region III: oscillatory, region IV & V: break-up. Adapted from Tripathi et al. [2].

The axisymmetric rectilinear path is indicated by region I, while a bubble in region III rises in an oscillatory fashion, either spiralling or zigzagging. The remaining regimes, where region II indicates a bubble with a thin skirt trailing from the body and bubbles in regions IV & V experiencing break-up [2], will not be covered in this research. Since air bubbles up to a diameter of 2 mm rising in water are investigated, only regions I and III are of interest.

In addition to the results from Tripathi et al. [2, 6], Cano-Lozano et al. [14] carried out three-dimensional numerical simulations close to the path instability region. By fixing a bubble in a constant velocity inlet equal to the terminal velocity of that bubble (yielding so-called 'frozen' bubbles), the wake instabilities could be investigated, leading to the definition of the different regimes [6]. A similar regime overview to that of the previous figure, now focused on the transition between stable and oscillatory rise, is obtained and shown in Figure 1.2, where Bo and Ga are based on the diameter. Besides the already covered rectilinear, zigzagging and helical spiralling regions, Cano-Lozano et al. [14] distinguish two additional regimes: the flattened spiralling and chaotic regime. The former is described as a transient regime that eventually converges towards the zigzagging or the helical spiralling regime. However, as this temporary regime may exist over a large distance ($\mathcal{O}(100D_b)$), it is considered to be a stable state. In the remaining chaotic regime, slight lateral displacements of the bubble occur ($\mathcal{O}(0.1D_b)$) before the transition to the zigzagging or flat-spiralling regime takes place. The most interesting feature of the chaotic regime is that no standing eddy exists at the back of the bubble, as described earlier. Therefore, the path instability does not result from wake instability but likely follows from an interplay between the bubble and the surrounding flow [14].

1.3 Side-by-side Bubble Rise

In many applications, such as in the chemical or petrochemical industry where bubbles play a large role in bubble column reactors and heat exchangers to enhance heat and mass transfer [2, 4, 5], bubbles will not be isolated from other bubbles. Therefore, the side-by-side rise of bubbles will be investigated theoretically numerically in which interactions occur between the two bubbles. These interactions may lead to different behaviours, amongst which attraction (possibly leading to coalescence) and separation are two of the most common results.

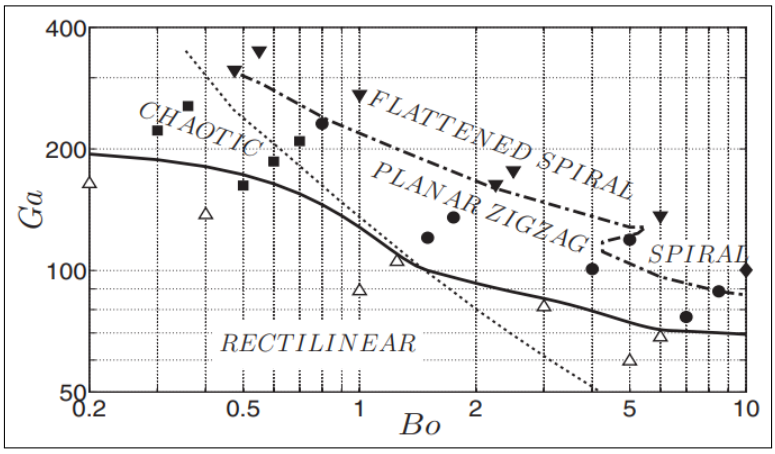

FIGURE 1.2: The different regimes near the path instability transition. The triangle (rectilinear), square (chaotic), circle (planar zigzag), inverted triangle (flattened spiral) and diamond (helical spiral) symbols indicate the results of the simulations from Cano-Lozano et al. [14]. The solid line describes the transition from stable rise to zigzag obtained with frozen bubble shape simulation [23] while the dash-dotted line indicates the transition from stable to unstable rise achieved with linear stability analysis for fixed bubbles [24]. The dotted line indicates the critical curve beyond which a standing eddy exists. Obtained from Cano-Lozano et al. [14].

1.3.1 Attraction and Repulsion

Based on numerical analysis, Legendre et al. [25] showed that the interactive behaviour between two side-by-side rising bubbles depends on the Reynolds number ($\mathrm{Re} = \rho_\mathrm{L} D_\mathrm{b} g / \mu_\mathrm{L}$). For a Reynolds number of $\mathcal{O}(100)$, attraction occurs, caused by a Venturi effect in the gap between the bubbles. As the bubbles rise, fluid will flow along the bubble surface, also entering the gap between the bubbles. Due to the incompressibility of the water, the fluid inside the gap has to be accelerated as the gap is narrowed (the Venturi effect). This acceleration leads to a decrease in the pressure between the bubbles by Bernoulli's principle. Since the pressure between the bubbles is lower than in the rest of the surrounding fluid, the bubbles will experience an attractive force, causing them to approach each other [25]. The exact value of the Reynolds number at which attraction occurs, also deemed $\mathrm{Re}_c(S)$, depends on the initial separation distance between the bubbles (S) as they are released. The separation is measured in bubble radii (R_b) from the centres of the bubbles, i.e. $S = 2(R_\mathrm{b})$ corresponds to the two bubbles touching.

The numerical analysis from Legendre et al. [25] also investigated bubble behaviour for Reynolds numbers below $\mathrm{Re}_c(S)$. One might expect the Venturi effect to also exist at lower Reynolds numbers, albeit to a lesser extent. This is, however, untrue due to the vortices being generated at the bubble surface. Legendre et al. [25] describe that at low Reynolds numbers, the presence of the second bubble blocks the diffusion of the vorticity in the gap between the bubbles, as can be seen in the upper-left part of Figure 1.3. In the figure, the right bubble can be seen (the symmetry axis being located at $x/R_\mathrm{b} = 0$). While the vorticity is diffused freely around its free surface on the right, the vorticity on the left part of the bubble is blocked by the other bubble. This blocked vorticity causes upward velocities in the gap, lowering the vertical fluid velocity through it. Instead of the Venturi effect taking place, the fluid is now decelerated. The deceleration causes a pressure gradient towards the symmetry plane between the bubbles, resulting in a repulsive force [26]. For high Reynolds numbers, the diffusion of the vorticity along the bubble surface is significantly higher, preventing any potential flow blockage in the gap (yielding attraction as discussed above), as can be seen from the lower-right part of Figure 1.3 [25].

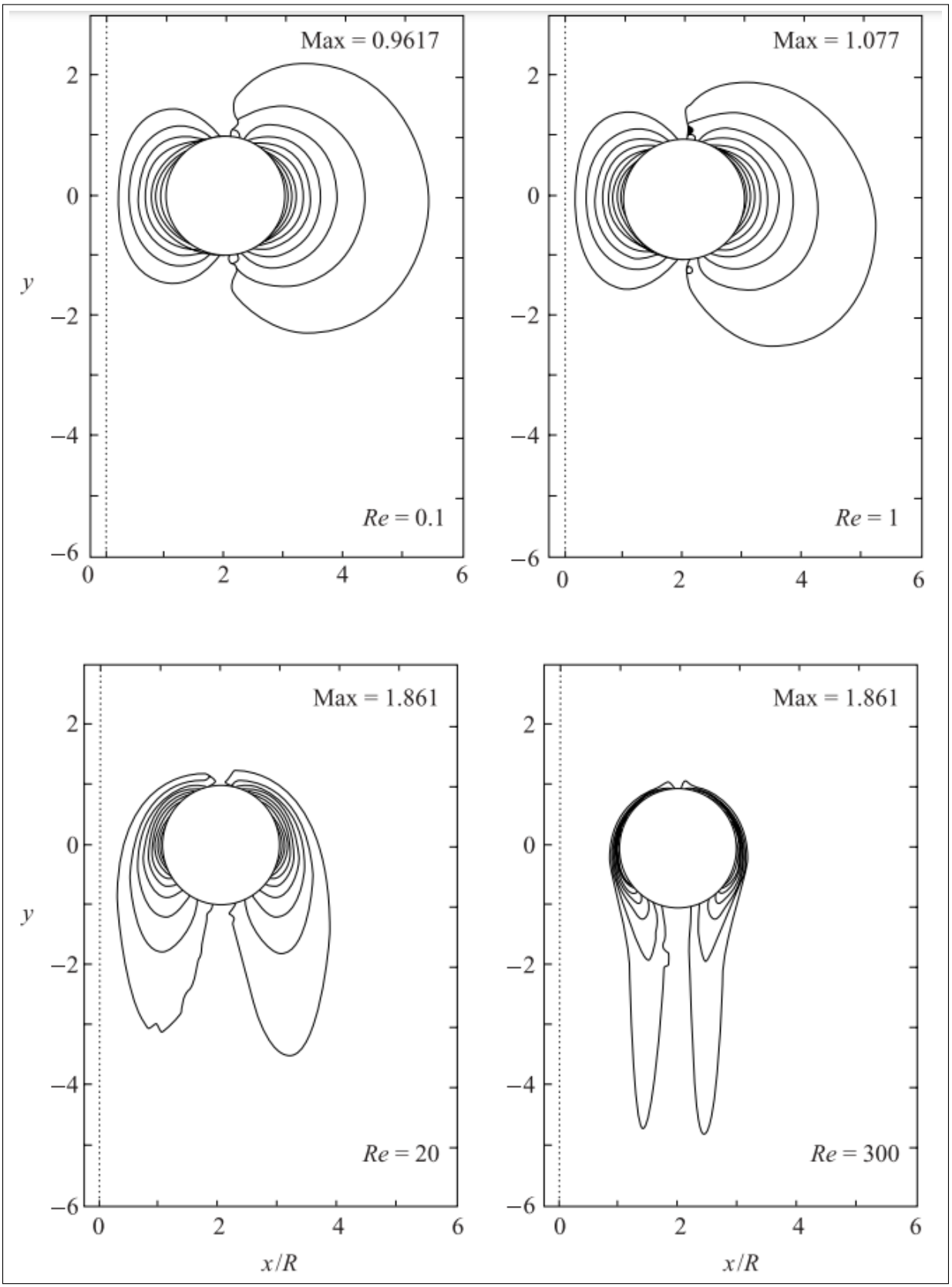

FIGURE 1.3: Iso-contours of the normalised vorticity in the $z = 0$ symmetry plane for a bubble pair at different Reynolds numbers with $S = 4$. The symmetry axis is located at the left at $x/R = 0$. Adapted from Legendre et al. [25].

1.3.2 Further Experimental and Numerical Results from Literature

To deepen the knowledge about bubble encounters, Duineveld [27] carried out a series of experiments on bubble pairs rising in pure water. One of the main questions was what minimum bubble size and approach velocity are required for bubbles to bounce instead of coalescing. By studying bubbles with a radius between 0.36 and 2.00 mm and an initial distance between the bubbles varying from $2.7R_b$ to $10R_b$, two different critical Weber numbers were defined. The first one (We_U) is based on the approach velocity of the bubbles (U):

$$We_U = \frac{\rho_L U^2 R_{eq}}{\sigma}, \tag{1.1}$$

in which R_{eq} is the equivalent radius, given by $R_{eq}^{-1} = 1/2(R_1^{-1} + R_2^{-1})$. When the Weber number based on the approach velocity exceeds a critical value $We_{U,cr}$ of 0.18 ± 0.03, bubbles would bounce, whereas they coalesce otherwise. Duineveld [27] related the bouncing to the fact that the liquid film between the bubbles cannot be drained fast enough. Subsequently, the repelling force caused by the increasing pressure in the film exceeds the driving force for the bubble approach (the inertia of the bubbles), leading to rebound. For bubbles with $R_b < 0.71$ mm, coalescence was found to take place for all initial separation S smaller than $10R_b$. Bubbles of such size cannot obtain a sufficiently high approach velocity to cause bouncing [27]. As described by Van Wijngaarden [28], the maximum approach velocity of two side-by-side rising bubbles is $0.86V_T$ (with V_T being the terminal rise velocity), causing the approach velocity to be dependent on the terminal rising velocity and thus on the bubble size.

Once bouncing has occurred, bubbles might coalesce or separate. Duineveld [27] describes that it depends on the Weber number (We_V) based on the rising velocity V of a bubble which phenomenon occurs, where We_V is given by:

$$We_V = \frac{2\rho_L V^2 R_b}{\sigma}. \tag{1.2}$$

As a result of the experiments, a critical Weber number based on the rise velocity $We_{V,cr}$ was defined, being approximately 2.6 ± 0.3 for the first bounce. Above this value, separation occurs, while coalescence takes place below it. It should be noted that attraction after the initial bounce does not automatically mean that coalescence follows. Repeated bouncing may occur, in which the approach velocity in a later bounce can exceed that of the initial bounce, eventually leading to separation, caused by a decrease in rise velocity. After bouncing, shape oscillations of the bubbles generally take place, reducing the total kinetic energy of the bubble [27].

The bouncing-separation phenomena was seen to take place above a bubble radius of approximately 0.86 mm, which is quite similar to the value at which a path instability occurs [7] ($R_b \approx 0.91$ mm [1]) as described earlier. Additionally, $We_{V,cr}$ is near the critical Weber number for instability of single bubbles as well ($We = 3.3$) [27]. As single bubble path instability and wake development are closely related, it is proposed that the wake of the approaching bubbles plays an essential role in the bouncing behaviour [27, 29, 30]. Duineveld [27] attributes the separation phenomenon to a trigger of the wake instability by the bubble bounce, causing the shedding of vortices. The bounce leads to considerable distortion, such that path instability arises at lower Weber numbers than for a single bubble. Sanada et al. [29] used an activated photochromic dye to visualize the bubble wakes and identified wake collision as the bubbles bounced. As the bubbles collided, both wakes entered between the bubbles during bubble deformation, ultimately overtaking the bubbles. Based on image visualization, the decrease in rise velocity after bouncing (as was also noticed by Duineveld [27] and De Vries et al. [13]) was attributed to the motion of the surrounding liquid, mainly caused by the bubble wake.

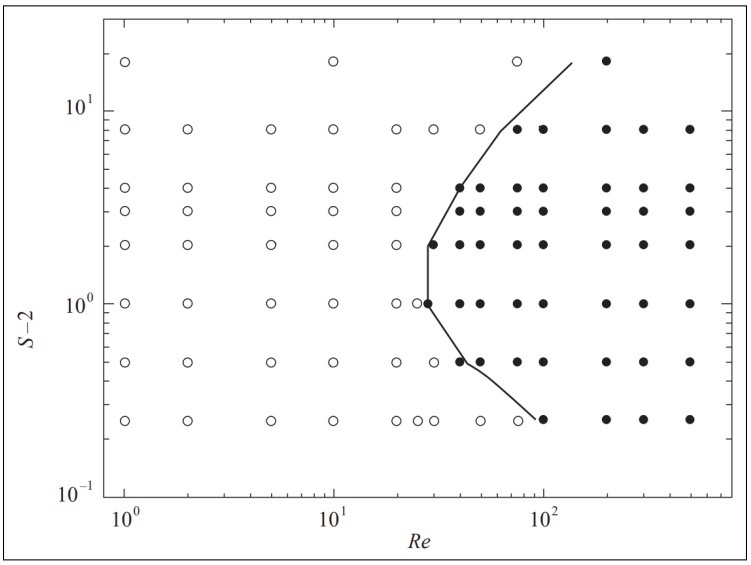

FIGURE 1.4: Values for the Reynolds number and separation for which side-by-side rising bubbles attract (●) or repel (○) each other. Adapted from Legendre et al. [25].

In addition to the experimental results from Duineveld [27], the numerical study from Legendre et al. [25] investigated the interaction between two spherical bubbles rising side-by-side in-depth as well. Amongst their results, they created a graph where the result of the side-by-side rise (either attraction or repulsion) was plotted as a function of the initial separation distance S and the Reynolds number Re, as can be seen in Figure 1.4. As shown in the figure, the transverse force between the bubbles is always repulsive, no matter the value of the initial separation, below a Reynolds number of Re $\approx$ 28. At this number, deemed $\mathrm{Re}_{\mathrm{rep}}$, the transverse force between the bubbles changes sign, indicating the existence of an equilibrium position. To their surprise, the numerical results suggested the presence of two equilibrium separation distances for Reynolds numbers greater than $\mathrm{Re}_{\mathrm{rep}}$. From Figure 1.4, it was deduced that only the smallest of the equilibrium values (deemed S_1) has a stable configuration. If the distance between the bubbles is decreased, a repulsive transverse force will occur, bringing the bubbles back to their equilibrium position. Similarly, if the distance between them is increased, an attractive transverse force occurs, re-establishing the equilibrium position. For the larger of the two equilibrium values (S_2), this effect is swapped: any slight deviation below the equilibrium position yields an attractive force, causing the bubbles to approach S_1, while a deviation above S_2 leads to the bubbles moving away infinitely far. Although the above holds for a Reynolds number larger than $\mathrm{Re}_{\mathrm{rep}}$, bubbles will be repelled infinitely far away if the Reynolds number does not exceed $\mathrm{Re}_{\mathrm{rep}}$ as no equilibrium position exists in this domain [25].

Numerical experiments from Kusuno & Sanada [31] have recently shown that deformable bubbles can repel each other even if the velocity inside the gap is larger than that of the surrounding fluid. Spherical bubbles, on the other hand, still attracted each other due to high rise velocities at large Re. In Figure 1.5, the smaller spherical bubble pair on the left ($D_{\mathrm{b}} = 1.10$ mm) can be seen to show coalescence, while the larger deformable bubble pair on the right ($D_{\mathrm{b}} = 1.50$ mm) shows repulsion in the same simulated liquid. Therefore, Kusuno & Sanada [31] stated that the repulsion of (deformable) bubbles cannot be explained by only taking into account the velocity inside the gap (which is larger than the rise velocity in both cases) but also by considering the wake interaction generated behind the bubbles. It was shown that the rotation direction of the vorticity within the wake participates in repulsion, regardless of bubble attraction or repulsion. This notion led to the statement that bubbles repel each other when the strength of the vortex pair behind the bubbles is amplified due to the bubble interaction. Otherwise, the conventional approach described by Legendre et al. [25] takes place [32].

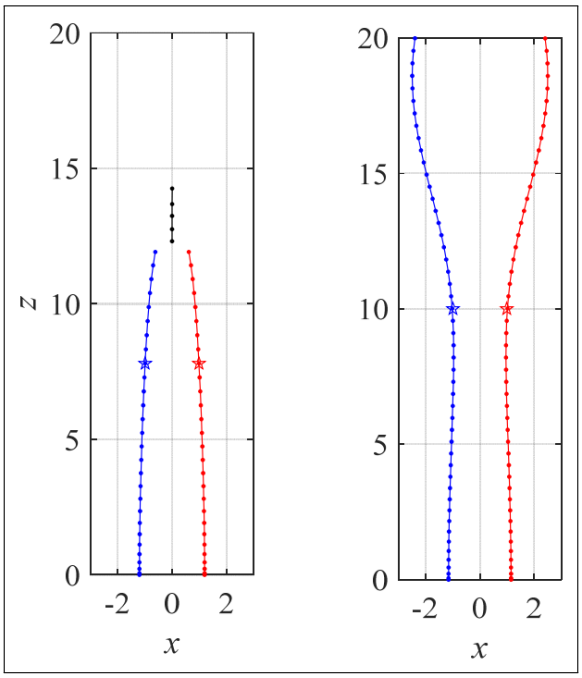

FIGURE 1.5: Trajectories of two bubble pairs. The left figure shows coalescence for Ga = 117 and Bo = 0.6, the right figure shows repulsion for Ga = 186 and Bo = 1.1. Adapted from Kusuno & Sanada [31].

1.4 In-line Bubble Rise

Besides the horizontal configuration of side-by-side bubble rise, bubbles can also rise in a vertically aligned arrangement. In general, the wake of the leading bubble causes an attractive force for the trailing bubble as it experiences a lower drag [33]. Initially, this will cause the trailing bubble to approach the leading bubble. This approaching behaviour, however, does not necessarily have to result in coalescence between the two bubbles. Other results, such as the ejection of the trailing bubble from the wake might also occur depending on the bubble and flow characteristics [33–36]. Below, the (non-) existence of an equilibrium position for in-line rise will be discussed.

1.4.1 Equilibrium Position

In contrast to the proposed existence of an equilibrium separation between side-by-side rising bubbles by Legendre et al. [25] and also later experimentally confirmed by Kong et al. [30], the existence of such an equilibrium distance between in-line rising bubbles is a topic for debate. Harper [37] analytically derived the presence of an equilibrium distance based on many simplifying assumptions, amongst which are a spherical bubble shape, an irrotational flow pattern and not taking the vorticity diffusion in the wake between the bubbles into account. The equilibrium position was shown to be stable for small vertical disturbances, but unstable for horizontal ones.

Yuan & Prosperetti [38] later carried out a numerical study, considering the effect of the vorticity shedding from the surface of the bubbles. Their results confirmed the existence of Harper's described equilibrium distance, whatever the initial separation, which is expressed as a balance between the attractive wake effect lowering the drag on the trailing bubble and the potential repulsive force caused by pressure gradients [39]. Their results, however, did not agree with the experimental outcome from Katz & Meneveau [40], who describe that all bubbles in their experiments catch up with each other and collide, leading to the conclusion

that the wake-induced relative motion is powerful enough to overcome any repulsive potential force. The discrepancy between the numerical analysis from Yuan & Prosperetti [38] and the experiments from Katz & Meneveau [40] was attributed to bubble deformation, which was neglected in the numerical analysis.

Based on the results from Yuan & Prosperetti [38] and the above-described discrepancy about the existence of an equilibrium position, Harper [41] again theoretically investigated the in-line rising behaviour. Vorticity diffusion in the wake between bubbles was found to be only negligible at (impossibly) high Reynolds numbers. Filella et al. [26] describe that further experimental research was also motivated due to the difference between the numerical and experimental analysis, leading to experiments from, amongst others, Watanabe & Sanada [35]. In their study, both experimental and numerical validation, taking into account the aforementioned surface deformation effects, for the existence of an equilibrium distance was found. At low Reynolds numbers (Re = 5), the same coalescing behaviour as described in Katz & Meneveau [40] could be seen in their experiments. For bubbles at intermediate Reynolds numbers ($5 < \text{Re} < 150$), however, the behaviour as predicted by Yuan & Prosperetti [38] was seen, showing an initial approach after which it ceased, leading to a constant distance between the bubbles. The difference between the results from Yuan & Prosperetti [38] and Katz & Meneveau [40] is assigned to the difference in Re. It should be noted, however, that the distance between the pair of bubbles as experimentally measured by Watanabe & Sanada [35] is significantly larger than that predicted by Yuan & Prosperetti [38] and that the equilibrium distance is also often unstable, leading to a varying distance which is dependent on the initial bubble separation distance for constant Re [35]. This difference is considered to originate from bubble deformation and three-dimensional effects of bubble motion, which were both not included in the analysis from Yuan & Prosperetti [35, 38]. Additionally, the numerical results from Watanabe & Sanada [35] showed an equilibrium distance smaller than that predicted by Yuan & Prosperetti [38] due to the incorporation of the bubble deformation.

Later numerical research by Ramírez-Muñoz et al. [42], using simple models for the trailing bubble drag, again showed the existence of stable equilibrium distances, agreeing well with the results from Yuan & Prosperetti [36, 38]. Recent research from Gumulya et al. [43] using 3D numerical simulations, however, was not able to reproduce the stable balance between the attractive forces of the wake and potential repulsion ahead of the trailing bubble within the parameters of their study ($0.1 \leq \text{Bo} \leq 1$ and $\text{Re} \leq 890$). On the other hand, they were able to reproduce the unstable in-line configuration for moderate Re values as described by Watanabe & Sanada [35]. The presence of the equilibrium distance as shown by Yuan & Prosperetti [38] and Watanabe & Sanada [35] is attributed towards the axisymmetric assumption taken in both studies [43].

1.4.2 Comparison Stable Configuration

In 2011, Hallez & Legendre [44] performed a numerical study on the three-dimensional flow around two spherical bubbles for a range of Reynolds numbers, separation distances and angular positions of the bubbles. Their results indicate that the side-by-side configuration for a pair of rising spherical bubbles is the only stable position due to the destabilizing effect of the wake in the in-line configuration [26]. A torque action exists for the in-line motion which tends to position the bubbles horizontally. Therefore, at a certain Reynolds number and separation (for instance $\text{Re} = 200$ and $S = 3.75$), the in-line motion proves to be unstable while the side-by-side configuration is stable [44]. Additionally, they describe that a stable in-line bubble configuration could be seen in controlled experiments [40, 45]. It is thought that this stability is caused by deformation from a spherical shape or by contaminants such as surfactants [37, 46–48].

1.5 Conclusion

In this literature study, the path instability of a single bubble and the side-by-side & in-line rise behaviour of bubble pairs were covered. Although the reason for the occurrence of a path instability has been a topic of discussion for centuries, its presence causes rectilinear bubble rise to switch towards either a zigzagging or a helical path, depending on the number of path instabilities occurring. While it has been thought for a long time that a standing eddy is required for a path instability to occur, a new regime has recently been discovered in which such an eddy does not occur. Therefore, the interplay between the bubble and the surrounding flow is thought to cause the path instability.

As bubbles often rise in large groups, the effect of bubbles rising side-by-side and in-line was investigated as well. Whether side-by-side bubbles attract or repel each other depends on a critical Reynolds number (Re_c) as a function of the separation distance (S) between the bubbles. The Venturi effect causes attraction between the bubbles at high Re, while vorticity interactions leading to flow blockage cause repulsion at low Re. Additionally, Duineveld [27] defined a Weber number based on the approach velocity of the bubble pair based on experiments, describing whether bubbles coalesce or bounce. Moreover, the Weber number based on the rise velocity determines if the bubble pair coalesces or separates after bouncing has occurred.

Whereas there is a consensus on the existence of an equilibrium position for side-by-side bubble rise, such agreement does not exist for in-line bubble rise. Multiple studies have experimentally and numerically confirmed or denied the existence of such a position, albeit by using (sometimes) rather crude simplifications. While experiments have shown a stable in-line configuration, it is thought that this is caused by the non-sphericity of the bubbles or surface contamination, still yielding disagreement about the existence of an equilibrium position for spherical bubbles rising in-line in pure water.

Chapter 2

Derivation of Analytical and Numerical Expressions for the Rise Velocity of Air Bubbles in Water

A single air bubble rises in water due to buoyancy. As it accelerates through the liquid, the drag from the surrounding medium increases. Ultimately, the bubble reaches a terminal velocity when the two forces (buoyancy and drag) balance. We investigate both the outcome of such a force balance and the transients preceding it. Comparison with experimental data and expressions from literature show good agreement with the analytical expressions for the terminal rise velocity of the spherical and deformed bubbles: the terminal rise velocities are within the experimental uncertainty of 10%. Such experimental uncertainties may occur from surfactants or contaminants. We use fully resolved finite volume-based direct numerical simulations in Basilisk to validate the rise velocity during acceleration. The acceleration, as obtained from these simulations, is captured reasonably well with the modified force balances, showing the best agreement for bubbles across different sizes. We also compare these simulations with the experiments and show an excellent agreement for the aspect ratio (a measure of the deformation of the bubbles) up to a bubble diameter of 1.6 mm.

2.1 Introduction

The dynamics of rising bubbles are an essential phenomenon that has been studied for centuries [3] due to its importance in understanding the basic principles of two-phase flows and their application in industrial processes [49]. Bubbles fulfil a vital role in heat exchangers and bubble column reactors, where they enhance heat and mass transfer by increasing the interfacial area between the gas and liquid phase [6, 50, 51]. Inside bubble column reactors, the mass transfer is often considered to be the limiting factor [52]. Therefore, sub-millimetre bubbles are considered to increase the interfacial area even further [50], where the terminal velocity of a single bubble can already give great insights [53]. In bubble column loop reactors, the slip velocity between the liquid and gas phase of the downward two-phase flow can be approximated by the terminal velocity of a single bubble [54]. When the terminal velocity is combined with the gas volume fraction, the slip velocity in conventional bubble column reactors can be determined [55, 56]. Further, it is crucial in power plant accidents to determine the shape and rising velocity of gas bubbles as the radioactive aerosol removal efficiency depends on bubble size, shape and rising velocity carrying the aerosols [57]. A fundamental understanding will be created by constructing force balances for rising bubbles. Based on the forces acting on the bubbles, equations for the terminal rise velocity of spherical and deformable bubbles will be constructed and compared to other expressions, experimental data from literature and simulations carried out by Basilisk. The comparison aims to validate the ability of force balances to accurately determine the terminal rise velocity for a multitude of bubble sizes.

The application of the force balances is not limited to establishing the terminal rise velocity. Moreover, the velocity over time can be calculated, which is of interest in the acceleration regime of bubble rise. The initial acceleration of a bubble has already been covered extensively in literature. It has theoretically [58–61], numerically [60, 62] and experimentally [63, 64] been determined that a bubble rises with an acceleration of $2g$ during the early stages of its life. Dominik & Cassel [65], however, found an initial acceleration greater than $3g$ by solving the Navier-Stokes equations for two-phase flow with the level-set method. Therefore, by utilising the relatively simple force balance expressions and Basilisk simulations, the velocity evolution during the initial stages of bubble rise is determined, which is difficult to capture by experimental means. As the number of expressions for the rise velocity, terminal rise velocity, spherical and deformable regime is quite large, an overview is given in Appendix 2.E.

Although the above describes single bubble behaviour, bubbles rarely rise isolated. In industrial processes, such as in bubble column reactors or heat exchangers [30, 39], the interaction between two bubbles rising in a side-by-side configuration is of interest as well. In Chapter 3, the effects causing and resulting from repulsion and attraction between the bubble pair are elaborated. Additionally, the effect on the rise velocity of a side-by-side configuration is compared in-depth to that of a single rising bubble.

2.2 Numerical Methodology

The simulation results in this study are obtained by Basilisk, which is an open-source flow solver that couples the Volume of Fluid (VOF) method with an adaptive mesh refinement (AMR) technique to efficiently solve multiphase flow problems [51]. The solver, developed by Popinet, is a successor of Gerris, of which the underlying equations and workings are elaborated in their publications [66, 67]. The Basilisk and Gerris flow solvers have already been validated by multiple authors simulating bubble motion, amongst others by Tripathi et al. [2, 6], Cano-Lozano et al. [14, 23] and Zhang et al. [33, 34, 51], showing its applicability for the simulation of bubble rise and bubble interactions.

When using a numerical solver to, for instance, simulate bubble behaviour, the obtained results should be within a certain degree of accuracy of the mesh-independent results. Due to the

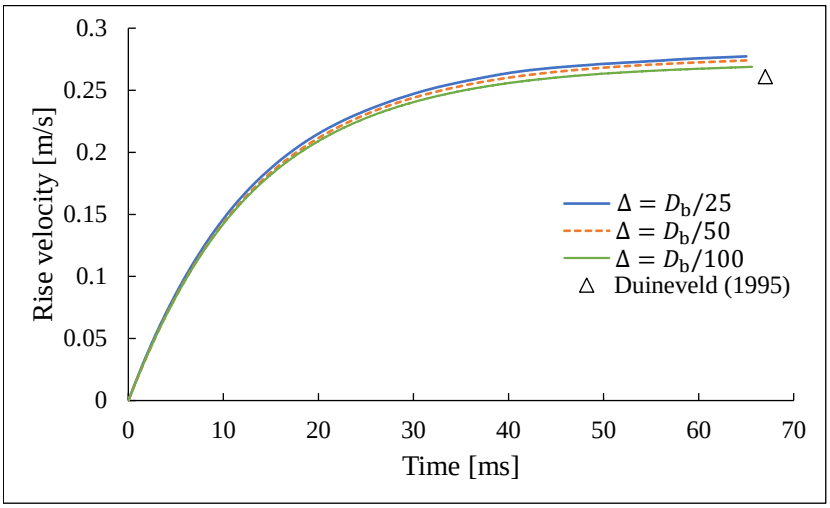

FIGURE 2.1: Mesh convergence for the case of a 1.0 mm diameter bubble compared to experimental data from Duineveld [7], indicating the terminal rise velocity.

relatively limited amount of available time and computational power, some concessions have to be made regarding the simulation accuracy achievable in the current study. The simulations are stopped when the bubble acceleration has declined to approximately 0.5 m/s^2. In this way, relatively representative values of the terminal rise velocity are still provided while large simulation times are prevented. In addition, it is decided that a minimum cell size of $\Delta = D_b/50$ is used for the simulations, where D_b is the bubble diameter. The introduction of these two simplifications leads to an over- or underestimation of the terminal velocity of approximately 5% compared to the simulation result achieved when the bubble acceleration is roughly 0 m/s^2 at the finer grids (i.e. $\Delta = D_b/100$ or finer). This accuracy is deemed acceptable in the current study.

As can be seen in Figures 2.1 & 2.2, the terminal velocity of two different bubble sizes (1.0 mm and 1.66 mm) slowly approaches the experimental value as obtained by Duineveld[1] [7] when refining the mesh size. The minimum cell size (Δ) of the simulation is governed by the AMR algorithm of Basilisk, which is further elaborated in the publication from Van Hooft et al. [68]. Figure 2.2 reveals that $\Delta = D_b/100$ shows a result which is close to being grid independent, which is not yet achieved at $\Delta = D_b/50$. Previous publications employing Gerris or Basilisk have seen a similar result for the minimum grid size requirement. The studies from Tripathi et al. [6], Cano-Lozano et al. [14] and Zhang et al. [51], respectively utilised 70, 128 and 64 grid cells per bubble diameter for their simulations.

From both figures, one may notice that a change in simulation behaviour occurs. While grid refinement for the smaller 1.0 mm bubble results in a decrease of the terminal rise velocity, the opposite is true for the larger 1.66 mm bubble. In both cases, however, the experimental value from Duineveld [7] is approached as the grids are refined. What exactly causes this shift in behaviour could not yet be determined. The influence of the deformability of a bubble, which might play a role, is further discussed in Section 2.5.2.

The simulated domain in this study is a cube with sides of 20 times the bubble diameter for small spherical bubbles and 40 times the bubble diameter for larger deformable bubbles, see Figure 2.3. The bubbles are initiated three diameters above the bottom plane to minimise boundary effects from the walls. This choice also means that bubble generation is not taken into account, saving computational effort and creating the same initial state for all simulated bubbles.

[1] In his experiments, errors were proven to be small due to perfect stationary rise velocities, at most 0.03 m/s.

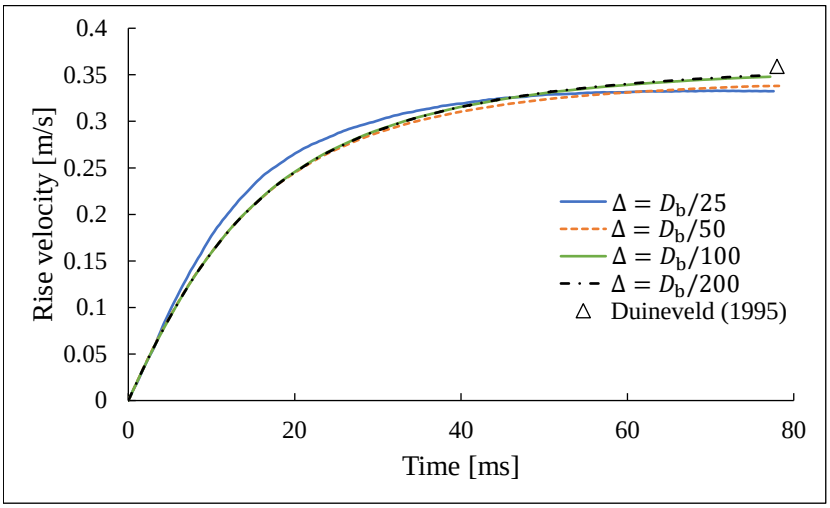

FIGURE 2.2: Mesh convergence for the case of a 1.66 mm diameter bubble compared to experimental data from Duineveld [7], indicating the terminal rise velocity.

2.3 Spherical Bubbles

A bubble rising from rest will initially have a perfectly spherical shape due to the absence of any external force on the bubble surface. As the rise velocity increases due to buoyancy, the drag force acting on the interface may deform the bubble, yielding an ellipsoidal shape. To compare the size of perfectly spherical and ellipsoidal bubbles, a characteristic length is defined. The typical length used in the derivations for spherical or deformable bubbles is the so-called volume equivalent bubble radius R_b (where D_b is further defined as $2R_b$):

$$R_b = \left(\frac{3V_0}{4\pi}\right)^{1/3}, \tag{2.1}$$

where the bubble volume V_0 is given by $V_0 = (4\pi/3)R_h^2 R_v$ with R_h and R_v being the horizontal and vertical radius of an ellipsoidal bubble, respectively [69]. The aspect ratio $\chi = R_h/R_v$ can subsequently be defined to indicate the degree of sphericity of a bubble, where a large aspect ratio ($\chi \gtrsim 2$) indicates a bubble with a high degree of deformation. Spherical bubbles are described in this study as bubbles for which fluid inertia cannot be neglected (i.e. a Reynolds number larger than one, which occurs for $D_b \gtrsim 0.1$ mm for an air bubble in water, both at 20°C) but also do not show any significant deformation. The Reynolds number (Re) based on the rise velocity V is given by:

$$\mathrm{Re} = \frac{\rho_L D_b V}{\mu_L}, \tag{2.2}$$

in which ρ_L indicates the liquid density and μ_L the dynamic viscosity of the liquid. Legendre et al. [25] established that deformation can be neglected up to a Reynolds number of about 250 for high-surface-tension liquids like water, which corresponds to a bubble with a diameter of approximately 1.0 mm at terminal velocity. This result is in close agreement with experiments from Duineveld [7], who measured an aspect ratio of 1.1 for bubbles with a 1.0 mm diameter [69]. Manica et al. [69] determined that for $D_b < 0.6$ mm, no deformation and thus a spherical shape can be assumed, being lower than the diameter described by Legendre et al. [25]. The main difference is that no deformation, and thus $\chi \approx 1.0$, can be assumed at a diameter of 0.6 mm, while a bubble diameter of 1.0 mm indicates $\chi \approx 1.1$, leading to non-significant deformation [25]. The quantification of the diameter of a spherical bubble will be further elaborated in Section 2.3.3. There, the terminal rise velocity of a bubble with a diameter of 1.0 mm will be calculated, considering both the inclusion and omission of deformation.

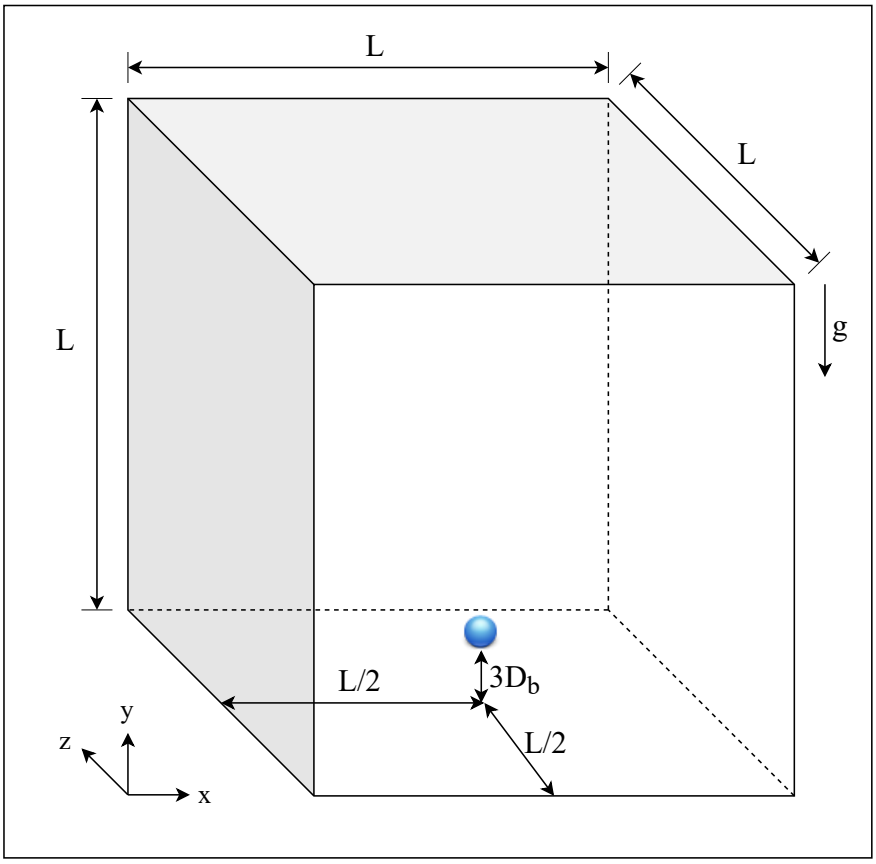

FIGURE 2.3: Initial configuration of the computational domain. Dimension L is $20D_b$ for spherical bubbles and $40D_b$ for deformable bubbles. The gravitational acceleration g acts in negative y-direction.

2.3.1 Force Balance Set-up

The force balance of a bubble rising due to buoyancy in a quiescent liquid is assumed to be given by the equation of motion of a 'point particle' [69]:

$$\Sigma F = \mathbf{F}_A + \mathbf{F}_B + \mathbf{F}_D = m\mathbf{a} \approx 0. \tag{2.3}$$

In the above equation, $\mathbf{F}_A$ is the added mass, $\mathbf{F}_B$ the buoyancy force and $\mathbf{F}_D$ the drag force. These different components will be discussed individually in the coming sections. It can also be seen that the contribution of $m\mathbf{a}$ is set to 0 due to the negligible mass of the bubble. However, there exists a finite acceleration of the bubble. This accelerating effect is taken into account because the fluid around the bubble has to be accelerated as well, which is a non-negligible effect [69].

Starting from its generation, a bubble following a straight path will accelerate during its rise until it has reached the terminal rising velocity. At this constant velocity, two forces are in balance with one another, being the buoyancy force that pushes the bubble upwards and the drag force providing the counteracting force, which can be seen in Figure 2.4. The buoyancy force is given by:

$$F_B = -\frac{4}{3}\pi R_b^3 \rho_L g \mathbf{k}. \tag{2.4}$$

Here, the unit vector $\mathbf{k}$ points in the vertical direction of the gravitation acceleration given by g [69]. Further, the density of the air in the bubble is neglected as it is significantly lower than the density of the fluid [69].

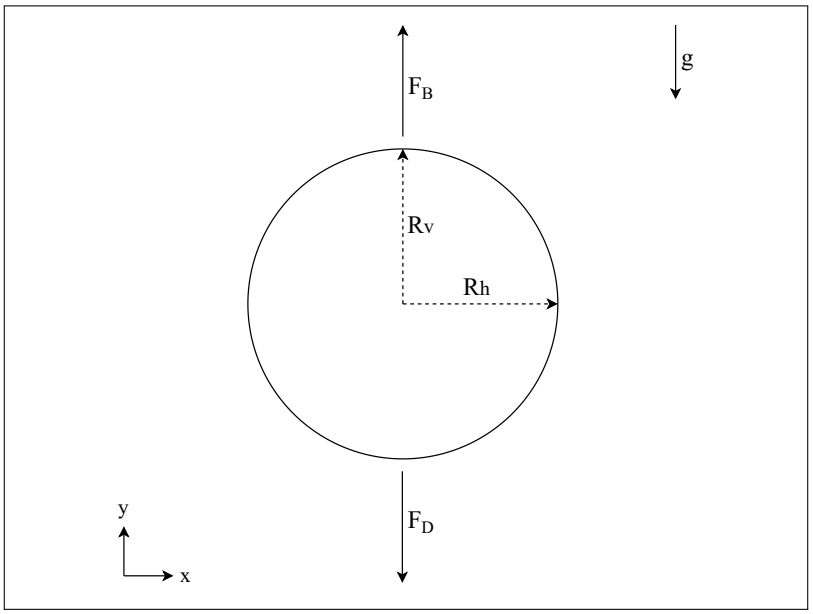

FIGURE 2.4: Force balance acting on a bubble at the terminal rise velocity from a front view. The buoyancy and drag force are indicated by F_B and F_D, respectively. For spherical bubbles $R_h = R_v$, while $R_h > R_v$ for the deformable case.

During bubble rise, the buoyancy force does not vary as it only depends on the bubble volume and density difference between the two phases, which both remain constant. The counteracting drag force, however, is altered during acceleration as it is a function of the bubble rise velocity V, as can be seen by:

$$F_D = \frac{1}{2}\rho_L A V^2 C_D \mathbf{k}, \tag{2.5}$$

in which A is the frontal area of the bubble, given by πR_b^2, and C_D is the drag coefficient [70]. A variety of expressions exist for the drag coefficient, each being used in different circumstances. For instance, the coefficient depends on the mobility of the bubble interface. A mobile, stress-free interface is achieved for experiments conducted in so-called 'hyper-clean' water [71]. A system containing surfactants or contaminants may cause bubbles to behave as solid spheres with an immobile boundary condition, yielding zero tangential velocity at the bubble interface [58]. Since the simulations carried out by Basilisk use 'pure' water without any contaminants, a bubble with a mobile interface will be assumed for the use in the force balances. Therefore, when validated against experiments, it is ensured that those experiments are carried out in clean water that aim to minimise or eliminate the effects of surfactants and contaminants. The selection and calculation of a variety of drag coefficient expressions will be covered in the following section.

2.3.2 The Drag Coefficient

Determining a suitable drag coefficient depends on the treated geometry and the order of the Reynolds number. One of the most simple definitions is given by Stokes [72], which holds for the drag on a sphere in the low Reynolds number regime ($\mathrm{Re} < 1$):

$$C_{D,\mathrm{Stokes}} = \frac{16}{\mathrm{Re}}. \tag{2.6}$$

While momentum convection had been ignored by Stokes, Oseen [73, 74] could not justify this simplification [75]. The inclusion of a correction term for the momentum convection leads to

an improved expression for flows at low Re, shown by Equation (2.7) [76]:

$$C_{D,Oseen} = 3 + \frac{16}{Re} = 3 + C_{D,Stokes}. \tag{2.7}$$

Spherical bubble rise at large Reynolds numbers is characterised by a different drag coefficient. The well-known result from Levich [77] can be used as a starting point, derived via a dissipation method in the limit of irrotational flow (Re = ∞) [78, 79]:

$$C_{D,Levich} = \frac{48}{Re}. \tag{2.8}$$

Subsequently, Moore [78] derived the following expression for a spherical gas bubble as a correction to the drag coefficient from Levich:

$$C_{D,Moore_1} = \frac{48}{Re}\left(1 - \frac{2.21}{\sqrt{Re}}\right). \tag{2.9}$$

The adaptation by Moore as shown above, deemed Moore's correction, takes into account the diffusion and transport of vorticity in the wake which is produced at the bubble surface [78]. The expression shows that the generated vorticity lowers the drag that the bubble experiences [44] and holds for bubbles with a zero tangential stress boundary condition (mobile interface) [25, 69]. It can also clearly be seen that the bracket term becomes negative at low Reynolds numbers ($< 2.21^2$), resulting in a negative drag coefficient and yielding non-physical behaviour. Therefore, the drag coefficient given by Moore only holds for high enough Reynolds numbers ($Re \gtrsim 15$), at which sufficient vorticity is produced at the bubble surface.

Small bubbles can already acquire their terminal rise velocity in the viscous Stokes regime, for which Moore's correction is invalid. Since one may not know beforehand in which regime a bubble exists, a transition function can be applied that initially makes use of the drag coefficient in the Stokes regime, after which it switches to the drag coefficient given by Moore at high enough Re. An expression following the same thought process is given by Mei et al. [80] for spherical bubbles [81]:

$$C_{D,Mei} = \frac{16}{Re}\left[1 + \left(\frac{8}{Re} + \frac{1}{2}\left(1 + \frac{3.32}{\sqrt{Re}}\right)\right)^{-1}\right]. \tag{2.10}$$

The above expression transitions between two regimes: for high Re, Moore's drag law as given by Equation (2.9) is approached, while the drag coefficient formulation by Taylor & Acrivos [82] is obtained at low Re. The definition by Taylor & Acrivos takes into account small amounts of deformation at low Re [81]:

$$C_{D,T\&A} = 1 + \frac{16}{Re}\left[1 + \frac{Re}{8} + \frac{8}{15}(\chi - 1)\right]. \tag{2.11}$$

Since the aspect ratio has a value of approximately unity in the spherical regime, the drag coefficient as given by Taylor & Acrivos approaches the expression of Oseen as $\chi \to 1$ [81].

The transition behaviour from Equation (2.10) is shown in Figure 2.5, in which both separate expressions can be seen as well. It should be noted that the formulations for the drag coefficient are based on a bubble rising in a steady state. During acceleration, the Reynolds number is constantly altered by the increasing rise velocity, such that a steady state is not achieved for the drag coefficient. For simplicity, however, it is decided to utilise the steady-state drag coefficient expressions during bubble acceleration.

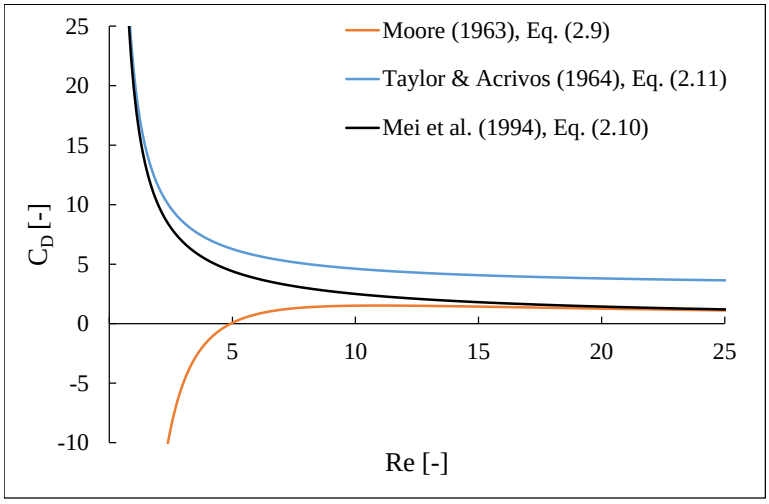

FIGURE 2.5: Transition from the drag coefficient at low Re (Taylor & Acrivos [82]) to that at high Re (Moore [78]) as given by Mei et al. [80].

Small Deformations in the Spherical Regime

While the above expressions all hold for spherical bubbles, small deformations might occur, resulting in a slightly deformed bubble. Moore [70] extended his original correction by incorporating bubble deformation via the aspect ratio χ:

$$C_{D,\mathrm{Moore}_2} = \frac{48}{\mathrm{Re}} G(\chi) \left(1 - \frac{2.21 H(\chi)}{\sqrt{\mathrm{Re}}}\right), \tag{2.12}$$

where the functions $G(\chi)$ and $H(\chi)$ are factors given by Moore [70] and change as bubble deformation increases. Loth [83] derived a simple approximation for both factors [81], given by:

$$\begin{aligned} G(\chi) &\simeq 0.1287 + 0.4256\chi + 0.4466\chi^2, \\ H(\chi) &\simeq 0.8886 + 0.5693\chi - 0.4563\chi^2. \end{aligned} \tag{2.13}$$

For spherical bubbles with little deformation, i.e. 0.6 mm $< D_\mathrm{b} <$ 1.0 mm as discussed earlier, one may use the constant aspect ratio of a bubble at terminal velocity during the entire bubble rise:

$$\chi^{-1} = \frac{0.74 + 0.45\lambda}{1 - 1.17\lambda + 2.74\lambda^2}, \tag{2.14}$$

where λ is equal to R_b/R_0 and $R_0 = 1$ mm [69]. Due to the small aspect ratio for spherical bubbles, χ can be assumed to be constant during rise as the deformation remains small [69]. For larger bubbles, the aspect ratio changes as a function of the rise velocity, which is further discussed in Section 2.4.

2.3.3 Terminal Rise Velocity of a Spherical Bubble

By setting the buoyancy force from Equation (2.4) equal to the drag force given by Equation (2.5) and using the drag coefficient defined by Mei et al. [80] (Eq. (2.10)), the following balance between drag and buoyancy must hold at the terminal rise velocity:

$$\frac{4}{3}\pi R_\mathrm{b}^3 \rho_\mathrm{L} g = \frac{\pi}{2} \rho_\mathrm{L} R_\mathrm{b}^2 V_{\mathrm{T,s}}^2 C_{D,\mathrm{Mei}}, \tag{2.15}$$

where $V_{\mathrm{T,s}}$ is the terminal rise velocity for a spherical bubble. The above equation overestimates the terminal rising velocity for $D_\mathrm{b} > 0.6$ mm as it does not take deformation into account, which

slows down bubble rise. The degree of overestimation for spherical bubbles up to a diameter of 1.0 mm can be determined by incorporating deformation (substituting Equation (2.14) into Equation (2.12)) instead of Equation (2.10) into the force balance. For a 1.0 mm bubble, this incorporation leads to a terminal rise velocity that is 19% lower compared to using Equation (2.15) without taking into account bubble deformation. The decrease is caused by the increased drag due to the deformed bubble shape having a larger frontal area. As a 19% difference in rise velocity is not negligible, it is decided that the above expression can only be used for perfect spherical bubbles. Bubbles larger than 0.6 mm will be covered by the deformable regime, which are further discussed in Section 2.4.

Since the drag coefficient expression in Equation (2.15) contains the Reynolds number to three different powers, it is not possible to rewrite the equation to a simple expression of $V_{T,s}$. Therefore, Equation (2.15), further referred to as the implicit spherical expression, should be solved iteratively for a prescribed bubble size and fluid to obtain a drag force that is equal to the buoyancy force, leading to a terminal rise velocity. However, a second approach is possible such that an explicit expression for the terminal rise velocity can be obtained, which is facilitated by employing the relation of Jamialahmadi et al. [84]. With the relation shown by Equation (2.16), further referred to as explicit spherical expression, the terminal rise velocity ($V_{T,J}$) over a large domain can be determined. The explicit expression combines the terminal velocity in the Stokes regime at low Re ($V_{T,low}$) and the terminal velocity in the spherical regime at high Re ($V_{T,high}$). Since $V_{T,high}$ is now used to indicate the terminal rise velocity at high Re, Moore's expression can be used for the drag coefficient without the requirement for a transition.

$$V_{T,J} = \frac{1}{\sqrt{\frac{1}{V_{T,low}^2} + \frac{1}{V_{T,high}^2}}}. \tag{2.16}$$

Bubbles in the Stokes regime with a mobile interface have a drag force $\mathbf{F}_D$ given by [58, 72]:

$$\mathbf{F}_{D,Stokes} = 4\pi\mu_L R_B V \mathbf{k}. \tag{2.17}$$

By setting the drag force equal to the buoyancy force, the terminal velocity in the Stokes regime ($V_{T,low}$) is achieved:

$$V_{T,low} = \frac{\rho_L g R_b^2}{3\mu_L}. \tag{2.18}$$

For $V_{T,high}$, the force balance at the terminal rise velocity of a spherical bubble when using Moore's drag coefficient yields:

$$\frac{4}{3}\pi R_b^3 \rho_L g = \frac{\pi}{2}\rho_L R_b^2 V_{T,high}^2 C_{D,Moore_1}. \tag{2.19}$$

$V_{T,high}$ can then be determined by rewriting the above equation (see Appendix 2.A):

$$V_{T,high} = \frac{1}{4}\left(\frac{2.21\sqrt{\mu_L}}{\sqrt{\rho_L D_b}} + \sqrt{\left(\frac{-2.21\sqrt{\mu_L}}{\sqrt{\rho_L D_b}}\right)^2 + \frac{4}{9\mu_L}R_b^2\rho_L g}\right)^2. \tag{2.20}$$

Combining Equations (2.18) & (2.20) with Equation (2.16) then yields an explicit expression for the terminal rise velocity.

The analytically derived expressions given by Equations (2.15) & (2.16) can be compared to a general correlation from Wallis [85] for spherical bubbles in the low-inertial range ($1 \lesssim \mathrm{Re} \lesssim 100$) [57]:

$$V_{\mathrm{T,s_{Wallis}}} = 0.14425 g^{5/6} \left(\frac{\rho_L}{\mu_L}\right)^{2/3} D_\mathrm{b}^{3/2}. \tag{2.21}$$

In addition to the above formula, which is only valid in the spherical regime, Baz-Rodríguez et al. [53] designed an expression for the terminal rising velocity of single bubbles in a pure liquid which is valid for both spherical and deformable bubbles. Two separate formulations for these regimes are used, after which they are combined into one equation via the relation proposed by Jamialahmadi et al. [84]:

$$V_{\mathrm{T,s_{B-R}}} = \frac{1}{\sqrt{\frac{1}{V_{\mathrm{T},1}^2} + \frac{1}{V_{\mathrm{T},2}^2}}}, \tag{2.22}$$

where $V_{\mathrm{T},1}$ and $V_{\mathrm{T},2}$ are the terminal rise velocities when viscosity dominates and when surface tension and inertia are dominant, respectively [53].

For the definition of $V_{\mathrm{T},1}$, Baz-Rodríguez et al. used Moore's expression for the drag force based on the solution of equations governing the boundary layer [50]. Combined with the buoyancy force, an equation was formed by expanding a Taylor series around the potential flow solution as derived by Levich [86]:

$$V_{\mathrm{T},1} = V_{\mathrm{T,pot}} \left[1 + 0.73667 \frac{(g D_\mathrm{b})^{1/2}}{V_{\mathrm{T,pot}}}\right]^{1/2}, \tag{2.23}$$

with:

$$V_{\mathrm{T,pot}} = \frac{1}{36} \frac{g D_\mathrm{b}^2 \Delta\rho}{\mu_\mathrm{L}}. \tag{2.24}$$

Once inertial and surface tension effects are becoming more dominant, an expression for $V_{\mathrm{T},2}$ is required. Lehrer [87] derived a mechanical energy balance, in which the introduction of a spherical particle into the continuous phase increases the potential energy (left-hand side of Equation (2.25)) of the phase due to surface tension and buoyancy effects (right-hand side of Equation (2.25)):

$$\frac{1}{12} \pi D_\mathrm{b}^3 \rho_\mathrm{L} V_\mathrm{L} = \sigma \pi D_\mathrm{b}^2 + \frac{1}{6} \pi D_\mathrm{b}^3 \Delta\rho_\mathrm{L} g D_\mathrm{b}, \tag{2.25}$$

where V_L indicates the displaced liquid velocity due to the rising bubble and σ the surface tension [53]. According to Lehrer [87], as the bubble rises through the continuous phase, the potential energy which exists in front of the bubble is converted into kinetic energy as the fluid moves around and to the aft side of the bubble. At the rear, the kinetic energy is dissipated in the wake. Lehrer [87] defined a time t which describes the time required for the conversion of potential to kinetic energy, which can be determined by the time it takes for a bubble to move a distance D_b at terminal velocity V_T. All of the above subsequently leads to the following expression for the terminal velocity when inertia is dominant [53, 87]:

$$V_{\mathrm{T},2} = \left(\frac{3\sigma}{\rho_\mathrm{L} D_\mathrm{b}} + \frac{g D_\mathrm{b} \Delta\rho}{2\rho_\mathrm{L}}\right)^{1/2}. \tag{2.26}$$

By combining Equations (2.23) and (2.26) in Equation (2.22), an expression for the terminal velocity of a bubble over a wide range of bubble sizes is achieved.

Next to the four discussed expressions, three experimental data sets for spherical bubbles of Sanada et al. [88], Pawliszak et al. [89] and Li et al. [50], all using clean water to create fully mobile bubble surfaces, are plotted in Figure 2.6. One can see Equation (2.16) and the formula

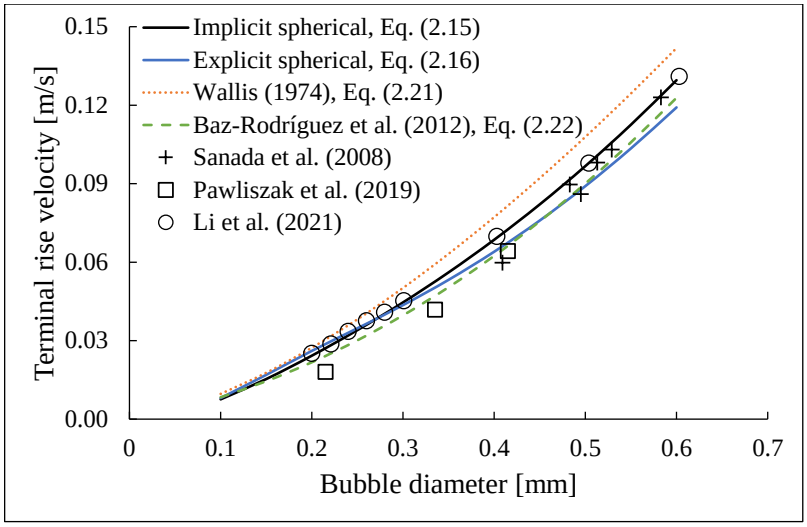

FIGURE 2.6: Comparison of the terminal rise velocity given by the various expressions and experiments of a spherical bubble.

from Baz-Rodríguez et al. showing good agreement over their entire range. Considering the different sets of experimental data as well, one can see that the two derived expressions quite accurately match the experimental data, with Equation (2.15) showing great agreement with the experimental data from Sanada et al. [88] and Li et al. [50] (3.8% error). Although Eq. (2.15) shows the best agreement with experiments at larger bubble sizes, the explicit expression does not deviate much and also does not require iteration to determine the terminal rise velocity for a particular bubble size. Therefore, both expressions are of interest, due to their accuracy or relative simplicity. Compared to the equations from Baz-Rodríguez et al. and Wallis, the implicit expression keeps its physical intuition, while that is lost when combining multiple regimes (such as the explicit formula) or data fitting.

2.3.4 Acceleration of a Spherical Bubble

The formulations given by Equations (2.15) & (2.16) only hold for the terminal rise velocity of a bubble. To determine the rise velocity during the acceleration phase as well, an additional force is required. The added mass force incorporates acceleration by considering the fact that the surrounding fluid around the bubble has to be accelerated as well as the bubble itself [69]. It is given by:

$$\mathbf{F}_{\mathrm{A}} = \frac{4}{3}\pi R_{\mathrm{b}}^3 \left(\rho_{\mathrm{L}} C_{\mathrm{m}} + \rho_{\mathrm{b}}\right) \frac{\mathrm{d}V}{\mathrm{d}t}\mathbf{k}, \tag{2.27}$$

in which C_{m} is the added mass coefficient, taking into account the fluid acceleration [58]. For a spherical bubble, $C_{\mathrm{m}} = 0.5$, while it increases for deformable bubbles [90] as more surrounding fluid has to be accelerated, slowing down bubble rise. Additionally, the density of the air in the bubbles (ρ_{b}) may be ignored as it is ~ 1000 times lower than that of the surrounding fluid [69]. Combining Equations (2.15) and (2.27) leads to a differential equation for the rise velocity of a spherical bubble (V_{s})[69]:

$$\frac{4}{3}\pi R_{\mathrm{b}}^3 \rho_{\mathrm{L}} C_{\mathrm{m}} \frac{\mathrm{d}V_{\mathrm{s}}}{\mathrm{d}t} = \frac{4}{3}\pi R_{\mathrm{b}}^3 \rho_{\mathrm{L}} g - \frac{\pi}{2}\rho_{\mathrm{L}} R_{\mathrm{b}}^2 V_{\mathrm{s}}^2 C_{\mathrm{D,Mei}}. \tag{2.28}$$

This expression can be solved for each time step by time integration until the terminal velocity is reached. Rewriting the equation as a function of the velocity of a spherical bubble at the

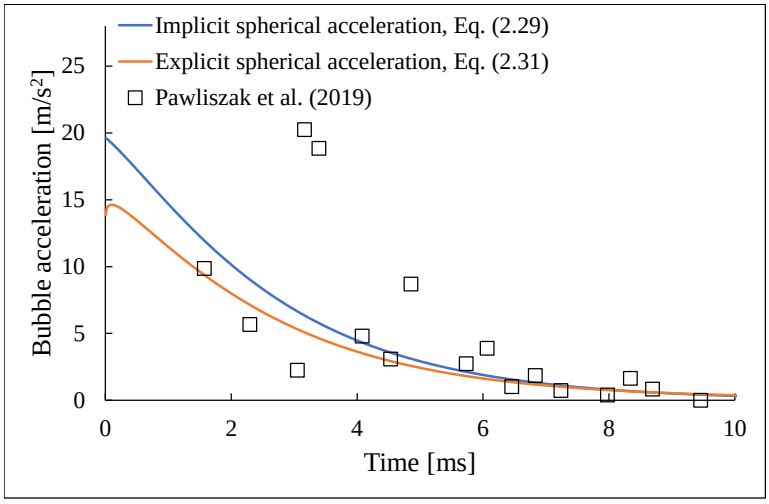

FIGURE 2.7: Acceleration path of a bubble with a diameter of 0.34 mm according to the implicit and explicit expression, including experimental data from Pawliszak et al. [89].

current time step n ($V_{n,s}$) by using the Forward Euler method leads to (see Appendix 2.B):

$$V_{n,s} = V_{n-1,s} + \Delta t \left(\frac{g}{C_m} - \frac{3}{8} \frac{C_{D,Mei}(V_{n-1,s}) V_{n-1,s}^2}{R_b C_m} \right). \tag{2.29}$$

One can already obtain some insight from the above Equation in a simple manner. At $t = 0$, there is no initial velocity yet (the bubble is released from rest in the surrounding fluid), such that $V_{n-1,s}$ equals 0. This yields $V_{n,s}$ to be equal to:

$$V_{0,s} = \Delta t \frac{g}{C_m}. \tag{2.30}$$

As C_m is equal to 0.5 all bubbles at t = 0 as no deformation has occurred yet, it can be seen that the initial acceleration of any bubble must be equal to $2g$ [69]. This result is also shown in Figure 2.7 for a bubble with a 0.34 mm diameter, shown in blue. After the initial acceleration of $2g$, the drag force starts to rise as the bubble velocity increases. Once the acceleration has decayed to approximately 0 m/s^2, the terminal rise velocity of the bubble is reached.

In addition to the rise velocity as obtained from the original force balance, the explicit expression combining the rise velocities of the low and high Re regimes is shown as well in orange in Figure 2.7. Since this simple expression can relatively accurately determine the terminal rise velocities of bubbles, it is utilised as well to show the rise velocity during the acceleration phase. The rise velocities over time at low and high Re as given by Equations (2.B.3) & (2.C.2) (see Appendix 2.B & 2.C), respectively, are combined by the expression from Jamialahmadi et al. [84]:

$$V_{n,J} = \frac{1}{\sqrt{\frac{1}{V_{n,low}^2} + \frac{1}{V_{n,high}^2}}}. \tag{2.31}$$

One of the shortcomings of Equation (2.31), however, is that it is only suitable for combining terminal velocities of different regimes. Applying it to every velocity in the acceleration phase will lead to incorrect acceleration behaviour, which can easily be seen by looking at the acceleration at $t = 0$. The velocity of any bubble in the low or high Re regime must be equal to $2g\Delta t$

at $t = 0$. Combining the two expressions with Equation (2.31) yields:

$$V_{0,\mathrm{J}} = \frac{1}{\sqrt{\frac{1}{(2g\Delta t)^2} + \frac{1}{(2g\Delta t)^2}}} = \frac{1}{\sqrt{\frac{2}{(2g\Delta t)^2}}} = \frac{2g\Delta t}{\sqrt{2}}. \tag{2.32}$$

From the above derivation, it can be seen that the velocity at $t = 0$ is divided by $\sqrt{2}$, resulting in an underestimated initial acceleration which can also be seen in Figure 2.7. Despite showing a too low initial acceleration, the terminal rise velocity close to that acquired in experiments is achieved as was shown in Figure 2.6. Therefore, Equation (2.31) is used to display a bubble's path to the terminal velocity in addition to Equation (2.29), albeit with an incorrect initial acceleration.

Next to the two expressions, experimental measurements from Pawliszak et al. [89] are also shown in Figure 2.7. In their study, the average rise velocity of at minimum 20 independent measurements was determined. From this, the acceleration was subsequently calculated. At early time steps, it can be seen that quite a large discrepancy exists between the experimental values and those from the implicit & explicit expressions due to the small time intervals and relatively large error margins. After approximately 4 ms, a better correspondence between the experimental values and both expressions is shown. In Section 2.5, the analytic and experimental results will be further compared to the simulations carried out by Basilisk.

2.4 Deformable Bubbles

Once the diameter of the bubble starts to exceed the limit for a spherical bubble, bubble deformability has to be taken into account. In this study, the deformable region is characterised as the regime following up spherical bubbles, but before path instability occurs, which holds for $100 \lesssim \mathrm{Re} \lesssim 750$ ($0.6\,\mathrm{mm} \lesssim D_\mathrm{b} \lesssim 2.0\,\mathrm{mm}$) [18]. The drag force and added mass are functions of the bubble shape and, thus, of the deformability. The aspect ratio affects the drag coefficient, as could be seen in Equation (2.12). For deformable bubbles, the aspect ratio can be related to the Weber number (We) of a bubble, which was first done by Moore [70]. By coupling the Weber number and the aspect ratio, χ is altered during the acceleration phase of bubble rise, affecting the rise velocity, the added mass and the drag force. Legendre et al. [91] derived a relation for the bubble deformation in water for $1 < \chi < 3$ as a function of the Weber number, where We is given by $\mathrm{We} = 2R_\mathrm{b}\rho_\mathrm{L}V^2/\sigma$:

$$\chi = \frac{1}{1 - \frac{9}{64}\mathrm{We}}. \tag{2.33}$$

In addition, according to Klaseboer et al. [90], the added mass coefficient C_m and aspect ratio are related by:

$$C_\mathrm{m}(\chi) = 0.62\chi - 0.12, \tag{2.34}$$

which holds for $1 < \chi < 2.5$.

2.4.1 Terminal Rise Velocity of a Deformable Bubble

Due to the same reasons as discussed in Section 2.3.3, it is difficult to define a relatively simple expression for the terminal rising velocity of a deformable bubble. Therefore, the following force balance between the drag force and buoyancy force must be solved iteratively to obtain the terminal velocity for a deformable bubble ($V_\mathrm{T,d}$):

$$\frac{4}{3}\pi R_\mathrm{b}^3\rho_\mathrm{L}g = \frac{\pi}{2}\rho_\mathrm{L}R_\mathrm{b}^2V_\mathrm{T,d}^2C_\mathrm{D,Rastello}(\chi), \tag{2.35}$$

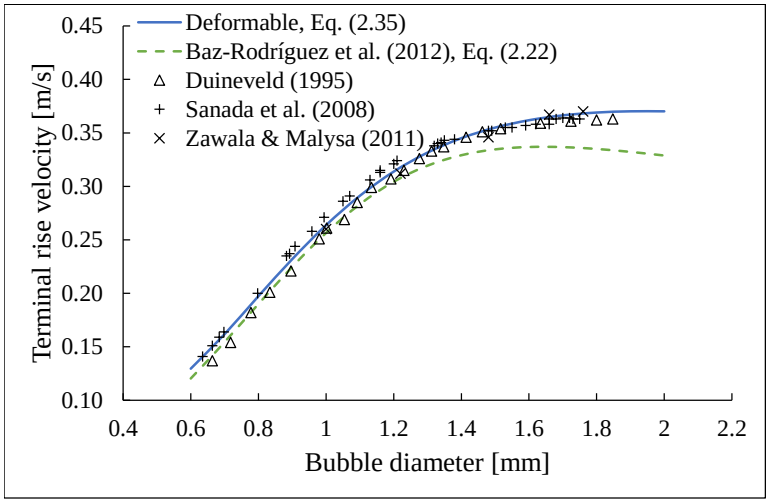

FIGURE 2.8: Comparison of the terminal rise velocity given by the various expressions and experiments of a deformable bubble.

where $C_{D,\text{Rastello}}(\chi)$ is a correction by Rastello et al. [81] on the drag coefficient by Mei et al. [80] to take into account bubble deformation:

$$C_{D,\text{Rastello}}(\chi) = \frac{16}{\text{Re}}\left[\frac{1+\frac{8}{15}(\chi-1)+0.015(3G(\chi)-2)\text{Re}}{1+0.015\text{Re}} + \left[\frac{8}{\text{Re}}+\frac{1}{2}\left(1+\frac{3.315H(\chi)G(\chi)}{\sqrt{\text{Re}}}\right)\right]^{-1}\right]. \tag{2.36}$$

By considering deformation during bubble rise, the rise velocity is lowered. A bubble with $D_b = 1.0$ mm and an aspect ratio of 2 yields a 58% lower terminal rise velocity than a similar-sized bubble with $\chi = 1$.

Similar to the methodology employed for spherical bubbles, the terminal rise velocity as given by Equation (2.35) is compared to the expression from Baz-Rodríguez et al. [53] by Equation (2.22) and experimental results from Duineveld [7], Sanada et al. [88] and Zawala & Malysa [92], all carried out in (ultra) clean water. From Figure 2.8, it can be seen that the analytical expression and the experimental values show excellent agreement over the entire range of bubble diameters (2.4% error). For the smaller deformable bubbles, good agreement can also be seen between the analytical expression and the expression from Baz-Rodríguez et al. Once larger bubble sizes are reached, diverging behaviour between both formulas is observed. The three experimental data sets, however, almost perfectly match the analytically derived expression. So, although iteration is required to obtain the correct terminal rise velocity from Equation (2.35), the terminal rise velocity for deformable bubbles seems to be very well-captured by the derived force balance.

2.4.2 Acceleration of a Deformable Bubble

In the same manner as was done previously for spherical bubbles, the rise velocity per time step of a deformable bubble ($V_{n,d}$) can be obtained by including the added mass with the χ-dependent C_m (Eq. (2.34)) into Equation (2.35) and rewriting it to an expression for $V_{n,d}$ (as was done as well in Appendix 2.B):

$$V_{n,d} = V_{n-1,d} + \Delta t\left(\frac{g}{C_m(\chi)} - \frac{3}{8}\frac{C_{D,\text{Mei}}(\chi)V_{n-1,d}^2}{R_b C_m(\chi)}\right). \tag{2.37}$$

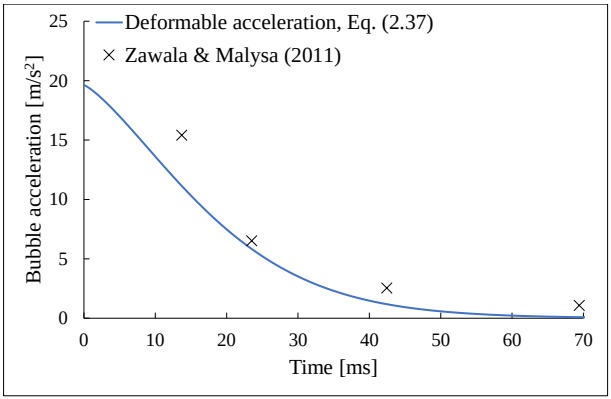

FIGURE 2.9: Acceleration path of a bubble with a diameter of 1.66 mm, including experimental data from Zawala & Malysa [92].

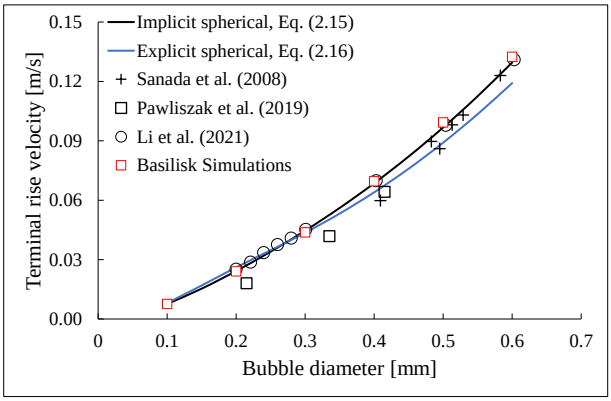

FIGURE 2.10: Comparison of the terminal rise velocity of spherical bubbles as achieved by Equations (2.15) & (2.16), three experimental data sets [50, 88, 89] and Basilisk simulations.

Compared to spherical bubbles, a transition between the viscous and inertial drag coefficients is not necessarily required as the bubble almost instantly surpasses the Stokes regime during the initial time steps (with $\Delta t = 1 \times 10^{-4}$ s). Therefore, the drag coefficient by Moore already accurately describes the drag over the entire acceleration path.

Figure 2.9 shows the result for a 1.66 mm diameter bubble and experimental data from Zawala & Malysa [92]. The deformable expression follows the general behaviour of the experimental results. However, the acceleration is continuously slightly underestimated. Despite this slight underestimation, the analytic terminal rise velocity showed good agreement with the experimental values as discussed before. The applicability of the deformable expression will be further elaborated in Section 2.5.2, where it is compared to the simulation results.

2.5 Basilisk Results

In Figures 2.6 & 2.8, the comparison between analytically derived formulas, expressions obtained from literature and data from experiments could be seen for the terminal rise velocity. In addition, simulation data from Basilisk will now be used to determine how well the bubble rise behaviour is captured. First, it is examined how accurately Basilisk determines the terminal rise velocity of spherical bubbles by comparing it to the results from the analytical expressions and experimental data. In Appendix 2.D, the terminal rise velocity from Basilisk is shown in a table for reference. After that, spherical bubble acceleration and deformable bubbles are investigated. Since it is challenging to experimentally measure the rise velocity of small spherical bubbles due to the small time scales involved, simulations can assist in creating a continuous evolution of the rise velocity over time. This problem of the lack of experimental data could also be seen in Figures 2.7 & 2.9, where little data is available at early time steps. Therefore, the simulations will be used to study the rise velocity during these early time steps. The results obtained on a grid with $\Delta = D_b/50$ are shown in the coming section, which, as discussed in Section 2.2, will result in a terminal rise velocity difference of approximately 5% compared to the finer grids with no remaining bubble acceleration.

2.5.1 Spherical Bubbles

Terminal Rise Velocity

The terminal rise velocities obtained from the simulations of Basilisk are shown in Figure 2.10, where a simulation was performed each 0.1 mm up to a bubble diameter of 0.6 mm. The figure

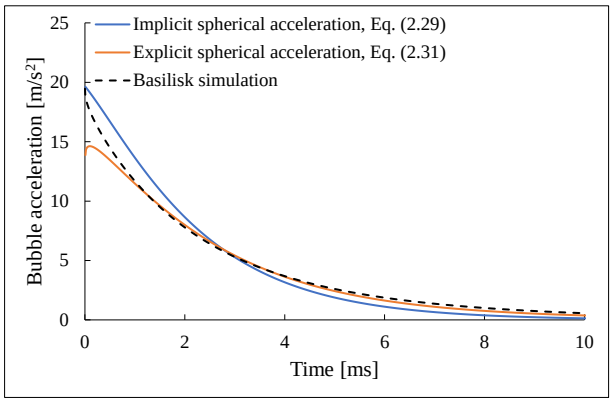

FIGURE 2.11: Simulated acceleration compared to the earlier obtained expressions for $D_b = 0.3$ mm.

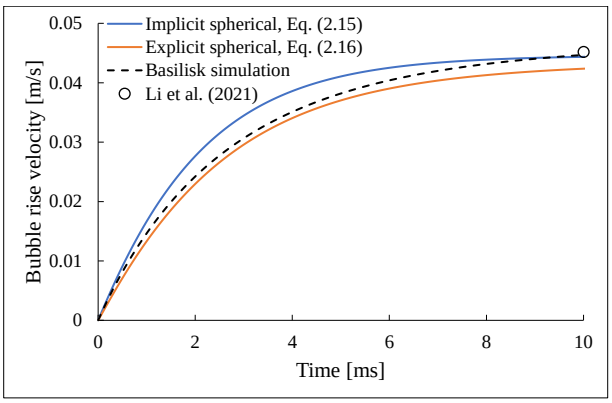

FIGURE 2.12: Simulated rise velocity compared to the earlier obtained expressions and an experimental terminal value from Li et al. [50] for $D_b = 0.3$ mm.

displays that Basilisk can determine the terminal rising velocity of different-sized spherical bubbles quite well. Good correspondence with the experiments from Li et al. [50] and Sanada et al. [88] can be seen while precisely following the implicit expression (1.6% error). Knowing that Basilisk can accurately determine the terminal rising velocity of a spherical bubble, it will be used to analyse the rise velocity during the acceleration phase.

Acceleration Regime

Figure 2.11 shows the simulation of a 0.3 mm diameter bubble in black starting with an acceleration of around $2g$, after which it quickly decreases[2]. In orange, the explicit expression can be seen, which shows the $2g/\sqrt{2}$ initial acceleration. Although the acceleration is too low for the early time steps, great agreement is shown once t $\sim$ 1 ms is surpassed. The blue line, making use of the drag coefficient from Mei et al. [80], does show a correct initial acceleration. The simulation, however, decelerates more quickly during the initial phase. As time passes, the simulation can be seen to decelerate slightly slower compared to the implicit expression, which can also be concluded from Figure 2.12 showing the rise velocity over time. An interesting aspect is observed during the early time steps: although the initial acceleration given by the explicit expression is too low, the rise velocity shows significant agreement with the simulation at early time steps. After 4 ms, the simulation shows diverging behaviour due to a slightly higher acceleration. While the implicit expression displays a larger difference regarding the initial phase of bubble rise, the simulation seems to approach it during the later stages, leading to a slightly more accurate terminal rise velocity as compared to the explicit expression.

When moving to the end of the spherical regime, better correspondence between simulation and implicit expression is obtained. Figure 2.13 gives the acceleration of a 0.6 mm bubble, showing good agreement between the implicit expression and the simulation. From t $\sim$ 10 ms, the explicit expression starts to show the same behaviour as well. The rise velocity, shown in Figure 2.14, reinforces the similarity between the implicit expression and the simulation. In addition, the terminal rise velocity from the experiment from Li et al. [50] shows a similar value as obtained by the expression and the simulation. The explicit expression shows a comparable rise velocity evolution once the acceleration has achieved a similar value of around 10 ms. In this case, the lower initial acceleration causes the explicit expression to be unable to follow the simulated behaviour.

[2]Due to the small time steps taken by Basilisk, large oscillations in the acceleration follow, disturbing the graph. Therefore, a curve fitting method is used for the simulated acceleration that might show a slightly different initial value.

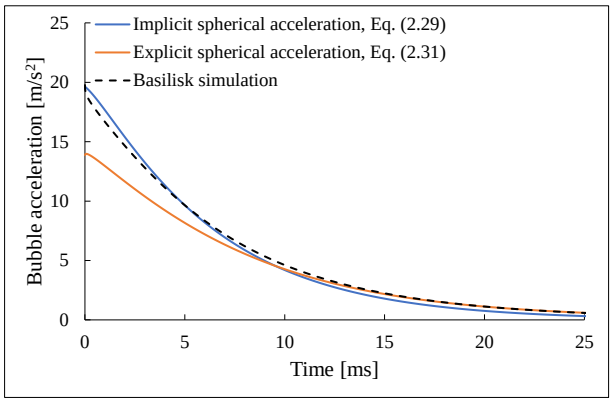

FIGURE 2.13: Simulated acceleration compared to the earlier obtained expressions for $D_b = 0.6$ mm.

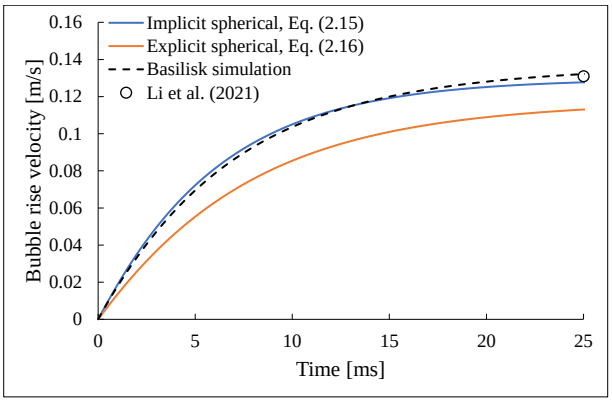

FIGURE 2.14: Simulated rise velocity compared to the earlier obtained expressions and an experimental terminal value from Li et al. [50] for $D_b = 0.6$ mm.

The difference between the expressions and the simulation at low bubble diameters is thought to be caused by the history force, which takes into account that the 'drag force needs some time to establish itself' [58]. The history force is commonly referred to as the Boussinesq-Basset force, owing to the pioneering observations made by Boussinesq [93] and Basset [94] regarding its existence. In the initial set-up of the force balance (Eq. (2.3)), the effect of the history force was neglected and is given by:

$$\mathbf{F}_H = 6\pi\mu_L R_b \int_0^t \frac{4}{3} e^{\xi^2} \operatorname{erfc}(\xi) \frac{dV}{d\tau} d\tau \mathbf{k}, \tag{2.38}$$

where $\xi = \sqrt{\frac{9\mu_L(t-\tau)}{R_b^2 \rho_L}}$, $\operatorname{erfc}(\xi) = \frac{2}{\sqrt{\pi}} \int_\xi^\infty \exp(-s^2) ds$ and $dV/d\tau$ indicates the past acceleration [58]. The incorporation of the history force would significantly complicate the expressions for the analytic derivations, which is why it was initially neglected. Manica et al. [58] state that the expressions including ξ in Equation (2.38) only hold for low Reynolds number flows. In addition, Takagi & Matsumoto [95] observed that 'the history force is negligible for a bubble rising through a clean liquid at Re $>$ 50'. This observation agrees with the fact that the terminal rise velocity for a 0.3 mm diameter bubble lies around Re $\approx$ 13 (Figure 2.11 displaying a rough fit), while the Reynolds number lies around 77 for a 0.6 mm diameter bubble (Figure 2.13 showing better agreement). Therefore, the inclusion of the history force for bubbles with a diameter smaller than 0.5 mm (Re $\approx$ 50 at terminal velocity) is required to obtain good agreement between simulations and the derived expressions for the rise velocity over time.

2.5.2 Deformable Bubbles

Terminal Rise Velocity

In Figure 2.15, the simulation results from Basilisk are shown for the terminal rise velocity of deformable bubbles and are compared to experimental data and the theoretical result from the force balance. For smaller deformable bubbles (up to $D_b \sim 1.2$ mm), the simulation somewhat overestimates the terminal rise velocity compared to the experimental data from Duineveld [7] and theoretical data (3.1% error). It does, however, show good agreement with the data from Sanada et al. [88]. Once the bubble diameter is increased past $\sim$ 1.5 mm, and thus more deformability takes place, the simulation starts to underestimate the terminal rise velocity compared to the theoretical expression (5.8% error). Since the terminal rise velocity and deformability influence each other greatly, the simulated and theoretically determined aspect ratio are

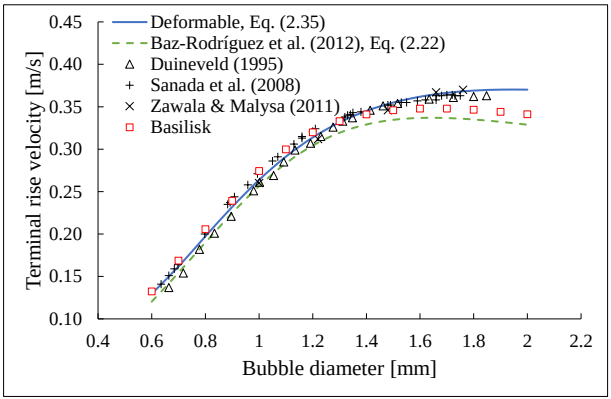

FIGURE 2.15: Comparison of the terminal rise velocity of deformable bubbles as achieved by Equation (2.35), several experiments [7, 88, 92] and Basilisk simulations.

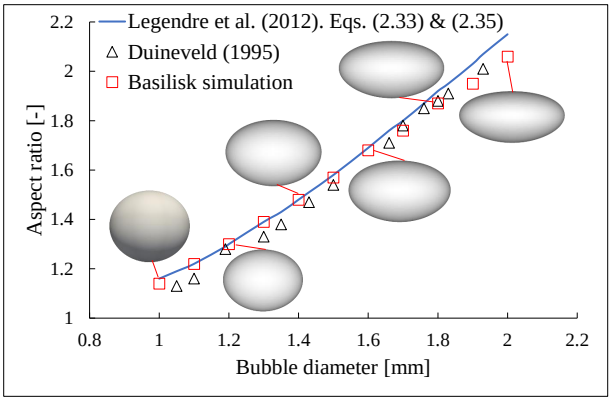

FIGURE 2.16: Comparison of the aspect ratio at terminal velocity between experiments from Duineveld [7], the expression from Legendre et al. [91] and simulations from Basilisk. Additionally, several bubble shapes at terminal velocity by Basilisk are shown.

plotted together with experimental data from Duineveld to determine whether the disagreement originates from the aspect ratio. As shown in Figure 2.16, the same $\sim$ 1.5 mm threshold can be seen, above which the simulations start to deviate from the results of the derived expression. Interestingly enough, the simulated aspect ratio approaches that of Duineveld above this threshold, while it was initially higher than the experimental values. However, this does not lead to the simulations showing the same terminal rise velocity as the experiments, as can be seen in Figure 2.15.

The difference between the theoretical and simulated terminal velocity can partly be attributed to the simplifications made for the simulations. The mesh convergence study from Section 2.2 showed that the combination of a grid-independent solution and achieving approximately zero remaining acceleration, results in a $\sim$ 5% higher terminal velocity for large bubbles than that achieved at the $\Delta = D_b/50$ grid. Such an increase would significantly increase the agreement between the experimental and theoretical data. In contrast to the larger bubbles, where mesh refinement and zero acceleration both increase the terminal rise velocity, the effect of mesh refinement approximately cancels out reaching zero acceleration for smaller bubbles. Therefore, a good agreement between the simulated and experimental & theoretical terminal rise velocity can be seen until a bubble diameter of $\sim$ 1.5 mm is reached. Still, however, no explanation can be given yet that clarifies the change from a decrease in terminal rise velocity with grid refinement at low bubble diameters to increasing it for larger bubbles.

Acceleration Regime

In Figures 2.17 & 2.18, the evolution of the acceleration and rise velocity over time for a 1.0 mm diameter bubble can be seen. The simulation can be seen to follow the theoretical acceleration well during the initial stages of bubble rise. The simulated bubble shows a slightly longer deceleration path, eventually resulting in a marginal overestimation of the experimental terminal velocity from Duineveld [7]. Figure 2.19 shows the simulation of the more deformable 1.8 mm bubble. Initially, an overestimated acceleration from the derived expression can be seen compared to the simulation (in black), resulting in a higher rise velocity in the early time steps, also see Figure 2.20. Around $t \sim 35$ ms, the simulation result obtains a larger acceleration than Eq. (2.37), leading to the simulated rise velocity approaching the derived expression. For the 1.8 mm bubble, an increased discrepancy between simulation and theory can be seen compared to the 1.0 mm bubble as was explained earlier. The same can be seen in Figure 2.21, which shows

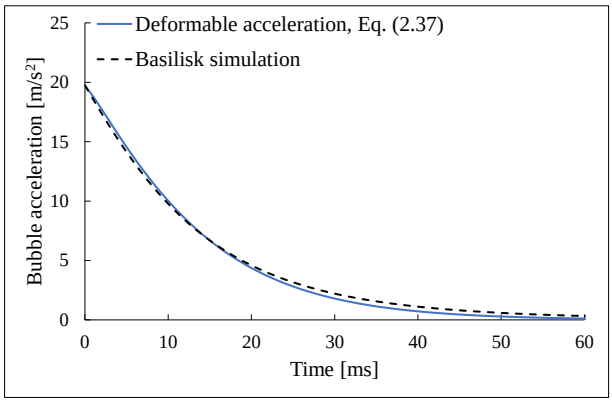

FIGURE 2.17: Simulated acceleration compared to the deformable expression for $D_b = 1.0$ mm.

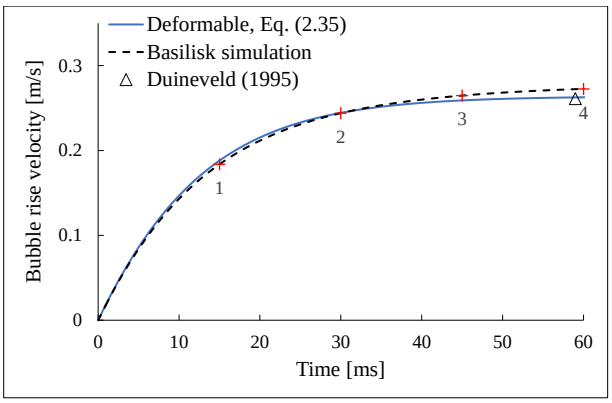

FIGURE 2.18: Simulated rise velocity compared to the deformable expression and an experimental value from Duineveld [7] for $D_b = 1.0$ mm. The shape of the bubble at numbers 1 to 4 during rise can be seen in Figure 2.21.

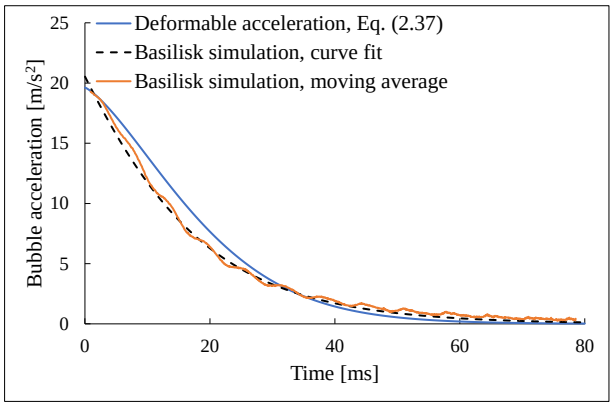

FIGURE 2.19: Simulated acceleration compared to the deformable expression for $D_b = 1.8$ mm.

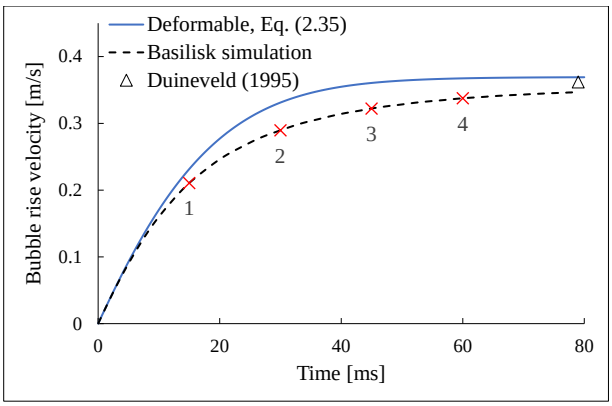

FIGURE 2.20: Simulated rise velocity compared to the deformable expression and an experimental value from Duineveld [7] for $D_b = 1.8$ mm. The shape of the bubble at numbers 1 to 4 during rise can be seen in Figure 2.21.

great agreement between the simulated and theoretical bubble shape (in dotted black) for the 1.0 mm bubble on the left. The underestimated simulated rise velocity for the 1.8 mm bubble, as shown in Figure 2.20, results in a less deformed bubble (right side of Figure 2.21).

Additionally, oscillations in the acceleration can be seen when using a moving average on the simulation data, given by the orange line in Figure 2.19. This behaviour is not observed in the rise velocity of the curve fitted line in black. The onset of path instability, at which straight bubble rise transforms into a zigzagging or spiralling path, is reached when a bubble obtains a volume equivalent radius of approximately $R_b = 0.91$ mm [18]. Therefore, the oscillations that can be seen in the acceleration are attributed to the fact that the instability threshold is approached by the simulations. At a diameter of 2.0 mm, however, no path instability could be seen yet in the simulations, which is likely caused by the inability of the coarser grid to capture the small-scale dynamics responsible for the transition.

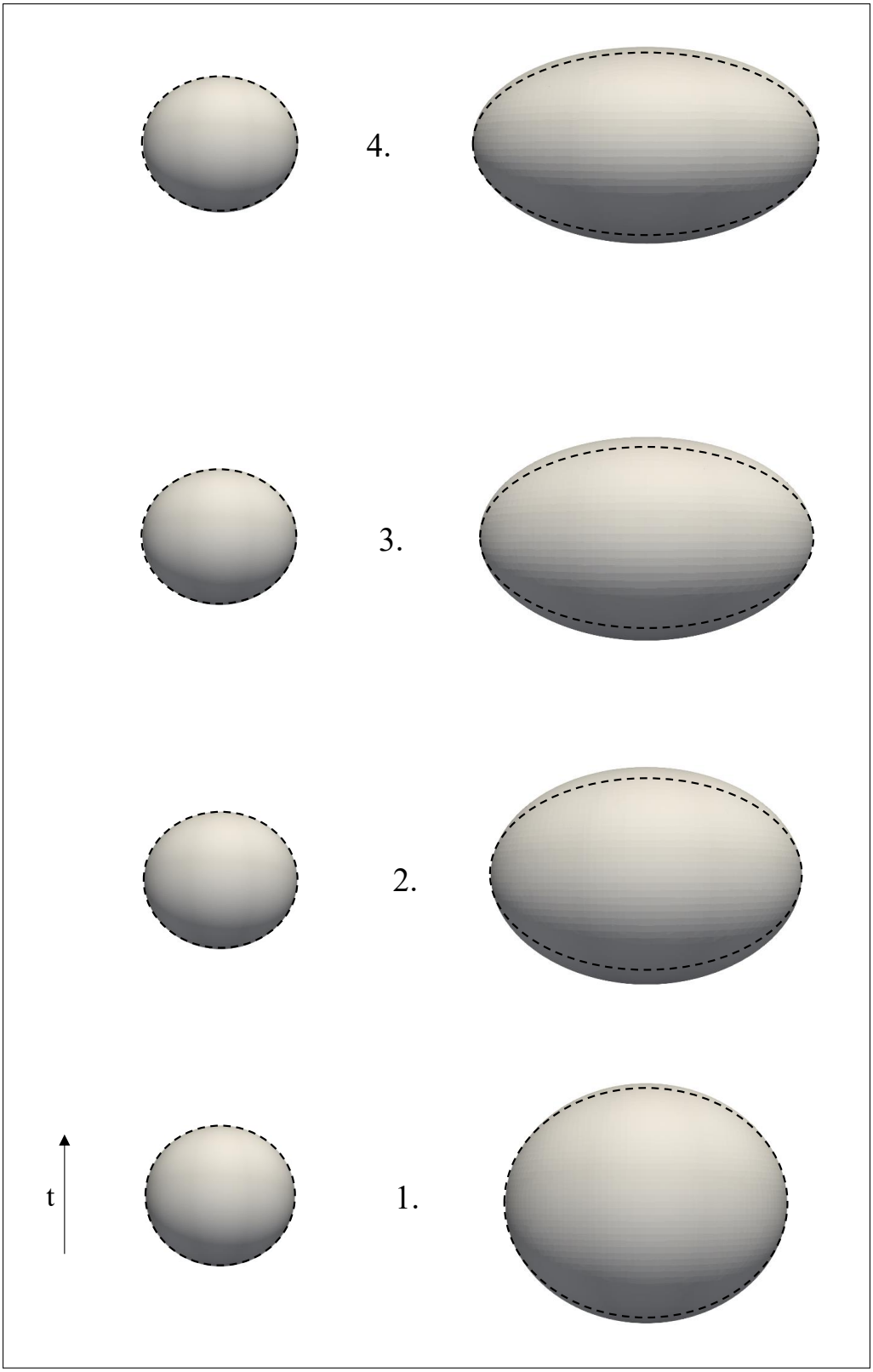

FIGURE 2.21: The shape of two bubbles as simulated by Basilisk, with in black the theoretical aspect ratio by Eq. (2.33). Left: a 1.0 mm bubble showing little deformation. Right: a 1.8 mm bubble showing a large degree of deformation. Starting from the bottom, t = 15 ms at point 1 and goes with intervals of 15 ms to t = 60 ms at point 4. See Figures 18 and 20 for the rise velocity evolution over these points.

2.6 Conclusion and Outlook

In this chapter, analytical and numerical expressions for the terminal rise velocity and the rise velocity over time for spherical and deformable bubbles were constructed. Expressions for the terminal velocity can be seen to show great correspondence with experimental data for spherical and deformable bubbles. Simulation results from Basilisk also showed to not differ much from the derived expressions and experimental data. A comparison between the simulation results and the derived equations for the rise velocity in the acceleration phase shows the best agreement for bubbles of intermediate size ($0.5\text{ mm} \lesssim D_\text{b} \lesssim 1.5\text{ mm}$). The results suggest less applicability of the expressions for bubbles relatively close to the Stokes regime (due to the neglected history force, of which the incorporation yields complex history terms) or experiencing a high degree of deformation ($\chi \gtrsim 1.5$). The latter, however, appears to be caused by too coarse grids and is not necessarily caused by the inability of the derived force balances to capture the rise velocity of deformable bubbles. Still, one can obtain relatively accurate indications for the rise behaviour of bubbles in these regimes.

Since the validation against data from literature is only carried out for air bubbles rising in water, it is interesting to determine whether the different expressions describe rise behaviour for other gaseous bubbles rising in a liquid as well. Therefore, further research into the validation of the derived equations might show applicability in other systems than the already covered air-water system. Additionally, rerunning the Basilisk simulations on finer grids yields the possibility of an improved comparative study between simulations and the derived expressions.

Appendix

2.A Derivation Terminal Rise Velocity Spherical Bubble

The terminal rise velocity as given by Equation (2.20) can be derived in the following way:

$$\begin{aligned}
\frac{4}{3}\pi R_b^3 \rho_L g &= \frac{\pi}{2}\rho_L R_b^2 V_{T,high}^2 C_{D,Moore_1}. \\
&= \frac{\pi}{2}\rho_L R_b^2 V_{T,high}^2 \frac{48}{Re}\left(1-\frac{2.21}{\sqrt{Re}}\right) \\
&= 12\pi\mu_L R_b V_{T,high}\left(1-\frac{2.21}{\sqrt{Re}}\right) \\
\rightarrow \frac{1}{9\mu_L}R_b^2\rho_L g &= V_{T,high}\left(1-\frac{2.21}{\sqrt{Re}}\right) \\
&= V_{T,high} - \frac{2.21\sqrt{\mu_L V_{T,high}}}{\sqrt{\rho_L D_b}}.
\end{aligned}$$

Substituting $U^2 = V_{T,high}$ gives:

$$\begin{aligned}
&U^2 - \frac{2.21\sqrt{\mu_L}U}{\sqrt{\rho_L D_b}} - \frac{1}{9\mu_L}R_b^2\rho_L g = 0 \\
&\rightarrow U = \frac{\frac{2.21\sqrt{\mu_L}}{\sqrt{\rho_L D_b}} \pm \sqrt{\left(-\frac{2.21\sqrt{\mu_L}}{\sqrt{\rho_L D_b}}\right)^2 + \frac{4}{9\mu_L}R_b^2\rho_L g}}{2} \\
&\rightarrow V_{T,high} = \\
&\frac{1}{4}\left(\frac{2.21\sqrt{\mu_L}}{\sqrt{\rho_L D_b}} + \sqrt{\left(\frac{-2.21\sqrt{\mu_L}}{\sqrt{\rho_L D_b}}\right)^2 + \frac{4}{9\mu_L}R_b^2\rho_L g}\right)^2.
\end{aligned} \tag{2.A.1}$$

The expression for U has a positive and a negative answer. However, changing the substitution to $U = \sqrt{V_{T,high}}$ instead of $U^2 = V_{T,high}$, one can see that the solution of U must be positive as $V_{T,high}$ cannot be negative. Therefore, only the '+'-contribution can be seen in the final expression for the terminal rise velocity as it leads to a positive U.

2.B Derivation Rise Velocity over Time Spherical Bubble

During the acceleration phase of a bubble, the added mass ensures an acceleration term is included in the force balance. The force balance is rewritten to an expression for the rise velocity

of a spherical bubble (V_s) at time step n in the following way:

$$\begin{aligned}\frac{4}{3}\pi R_b^3 \rho_L C_m \frac{dV_s}{dt} &= \frac{4}{3}\pi R_b^3 \rho_L g - \frac{\pi}{2}\rho_L R_b^2 V_s^2 C_{D,Mei}(V_s) \\ \rightarrow \frac{dV_s}{dt} &= \frac{g}{C_m} - \frac{3}{8}\frac{\pi R_b^2 V_s^2 C_{D,Mei}(V_s)}{\pi R_b^3 C_m} \\ &= \frac{g}{C_m} - \frac{3}{8}\frac{V_s^2 C_{D,Mei}(V_s)}{R_b C_m},\end{aligned} \tag{2.B.1}$$

which then leads to the expression shown in Equation (2.29) when applying time integration:

$$V_{n,s} = V_{n-1,s} + \Delta t \left(\frac{g}{C_m} - \frac{3}{8}\frac{C_{D,Mei}(V_{n-1,s}) V_{n-1,s}^2}{R_b C_m} \right). \tag{2.B.2}$$

When instead using Moore's drag coefficient, the following is obtained, which is used in Equation (2.31):

$$\begin{aligned}V_{n,high} &= V_{n-1,high} + \Delta t \left(\frac{g}{C_m} - \frac{3}{8}\frac{C_{D,Moore_1} V_{n-1,high}^2}{R_b C_m} \right) \\ &= V_{n-1,high} + \Delta t \left[\frac{g}{C_m} - \frac{9\mu_L V_{n-1,high}}{\rho_L R_b^2 C_m} \left(1 - \frac{2.21}{\sqrt{Re}} \right) \right].\end{aligned} \tag{2.B.3}$$

2.C Gravitational Acceleration in the Stokes Regime at $t = 0$

The force balance that holds for a bubble in the Stokes regime is similar to that shown in Equation (2.28) for a spherical bubble. The expression of the drag term, however, is exchanged with that of the Stokes drag (Eq. (2.17)), leading to the following force balance:

$$\frac{4}{3}\pi R_b^3 \rho_L C_m \frac{dV}{dt} = \frac{4}{3}\pi R_b^3 \rho_L g - 4\pi \mu_L R_B V. \tag{2.C.1}$$

Rewriting the above to an expression as a function of the current time step as was done in Equation (2.20), yields the following for the rise velocity of a bubble in the Stokes regime used in Equation (2.31):

$$V_{n,low} = V_{n-1,low} + \Delta t \left(\frac{g}{C_m} - 3\frac{\mu_L V_{n-1,low}}{\rho_L R_b^2 C_m} \right). \tag{2.C.2}$$

At $t = 0$, this then leads to the same expression of a spherical bubble, namely:

$$V_{0,low} = \Delta t \frac{g}{C_m}, \tag{2.C.3}$$

yielding an acceleration of $2g$ at $t = 0$ for a bubble in the Stokes regime, similar to a bubble in the spherical regime.

2.D Basilisk Results

Table 2.D.1 shows the simulation data for the terminal rise velocity shown in the various graphs, while Table 2.D.2 gives the values as seen in Figure 2.16.

TABLE 2.D.1: Terminal rise velocity as determined by Basilisk for various bubble diameters.

D_b [mm]	Terminal rise velocity [m/s]
0.1	0.008
0.2	0.024
0.3	0.044
0.4	0.070
0.5	0.099
0.6	0.132
0.7	0.169
0.8	0.206
0.9	0.239
1.0	0.274
1.1	0.300
1.2	0.320
1.3	0.333
1.4	0.341
1.5	0.346
1.6	0.348
1.7	0.348
1.8	0.347
1.9	0.344
2.0	0.341

TABLE 2.D.2: Comparison of the aspect ratio between experiments, theoretical expressions and simulations across a several bubble diameters.

D_b (mm)	Duineveld [7]	Legendre *et al.* [91] Eqs. (2.33) & (2.35)	Basilisk
1.00	-	1.16	1.14
1.05	1.13	1.19	-
1.10	1.16	1.22	1.22
1.19	1.29	1.28	-
1.20	-	1.30	1.30
1.30	1.33	1.39	1.39
1.35	1.38	1.43	-
1.40	-	1.48	1.48
1.43	1.47	1.51	-
1.50	1.54	1.58	1.57
1.60	-	1.69	1.68
1.66	1.71	1.76	-
1.70	1.78	1.80	1.76
1.76	1.85	1.87	-
1.80	1.88	1.92	1.87
1.83	1.91	1.95	-
1.90	-	1.98	2.03
1.93	2.01	2.07	-
2.00	-	2.15	2.06

2.E Overview Equations

Tables 2.E.1 & 2.E.2 show an overview of the most essential expressions used in this study. The application of each formula is given as well.

TABLE 2.E.1: Summary of main equations in this study, part 1

Equation	Eq. number	Application
$\frac{4}{3}\pi R_b^3 \rho_L g = \frac{\pi}{2}\rho_L R_b^2 V_{T,s}^2 C_{D,Mei}$	(2.15)	Force balance for spherical bubbles at the terminal rise velocity. Referred to as the implicit expression
$V_{T,J} = \frac{1}{\sqrt{\frac{1}{V_{T,low}^2} + \frac{1}{V_{T,high}^2}}}$	(2.16)	Different approach to achieve the terminal rise velocity of a spherical bubble. Referred to as the explicit expression
$V_{T,low} = \frac{\rho_L g R_b^2}{3\mu_L}$	(2.18)	Terminal rise velocity of spherical a bubble in the low Re regime ($1 < \mathrm{Re} \lesssim 10$ in this study), used in Eq. (2.16)
$V_{T,high} = \frac{1}{4}\left(\frac{2.21\sqrt{\mu_L}}{\sqrt{\rho_L D_b}} + \sqrt{\left(\frac{2.21\sqrt{\mu_L}}{\sqrt{\rho_L D_b}}\right)^2 + \frac{4}{9\mu_L} R_b^2 \rho_L g}\right)^2$	(2.20)	Terminal rise velocity of spherical a bubble in the high Re regime ($10 \lesssim \mathrm{Re} \lesssim 100$ in this study), used in Eq. (2.16)
$V_{n,s} = V_{n-1,s} + \Delta t\left(\frac{g}{C_m} - \frac{3}{8}\frac{C_{D,Mei}(V_{n-1,s})V_{n-1,s}^2}{R_b C_m}\right)$	(2.29)	Rise velocity of a spherical bubble per time step. Used for the acceleration phase, based on Eq. (2.15)
$V_{n,J} = \frac{1}{\sqrt{\frac{1}{V_{n,low}^2} + \frac{1}{V_{n,high}^2}}}$	(2.31)	Rise velocity of a spherical bubble per time step. Used for the acceleration phase, based on Eq. (2.16)
$V_{n,low} = V_{n-1,low} + \Delta t\left(\frac{g}{C_m} - 3\frac{\mu_L V_{n-1,low}}{\rho_L R_b^2 C_m}\right)$	(2.C.2)	Rise velocity of a spherical bubble per time step in the low Re regime ($1 < \mathrm{Re} \lesssim 10$ in this study), used in Eq. (2.31)
$V_{n,high} = V_{n-1,high} + \Delta t\left[\frac{g}{C_m} - \frac{9\mu_L V_{n-1,high}}{\rho_L R_b^2 C_m}\left(1 - \frac{2.21}{\sqrt{\mathrm{Re}}}\right)\right]$	(2.B.3)	Rise velocity of a spherical bubble per time step in the high Re regime ($10 \lesssim \mathrm{Re} \lesssim 100$ in this study), used in Eq. (2.31)

TABLE 2.E.2: Summary of main equations in this study, part 2

Equation	Eq. number	Application
$\frac{4}{3}\pi R_b^3 \rho_L g = \frac{\pi}{2}\rho_L R_b^2 V_{T,d}^2 C_{D,Rastello}(\chi)$	(2.35)	Force balance for deformable bubbles at the terminal rise velocity
$V_{n,d} = V_{n-1,d} + \Delta t \left(\frac{g}{C_m(\chi)} - \frac{3}{8}\frac{C_{D,Rastello}(\chi) V_{n-1,d}^2}{R_b C_m(\chi)} \right)$	(2.37)	Rise velocity of a deformable bubble per time step. Used for the acceleration phase, based on Eq. (2.35)
$C_{D,Stokes} = \frac{16}{Re}$	(2.6)	Stokes drag coefficient, valid at low Re ($1 < Re \lesssim 10$ in this study)
$C_{D,Moore_1} = \frac{48}{Re}\left(1 - \frac{2.21}{\sqrt{Re}}\right)$	(2.9)	Moore's drag coefficient for spherical bubbles, valid for $10 \lesssim Re \lesssim 100$ in this study
$C_{D,Mei} = \frac{16}{Re}\left[1 + \left(\frac{8}{Re} + \frac{1}{2}\left(1 + \frac{3.32}{\sqrt{Re}}\right)\right)^{-1}\right]$	(2.10)	Rastello's drag coefficient, valid over entire spherical range of covered Re ($1 < Re \lesssim 100$)
$C_{D,Moore_2} = \frac{48}{Re} G(\chi)\left(1 - \frac{2.21 H(\chi)}{\sqrt{Re}}\right)$	(2.12)	Moore's drag coefficient for deformable bubbles, valid for $10 \lesssim Re \lesssim 750$ in this study
$C_{D,Rastello}(\chi) = \frac{16}{Re}\left[\frac{1+\frac{8}{15}(\chi-1)+0.015(3G(\chi)-2)Re}{1+0.015Re} + \left[\frac{8}{Re} + \frac{1}{2}\left(1 + \frac{3.315 H(\chi) G(\chi)}{Re^{\frac{1}{2}}}\right)\right]^{-1}\right]$	(2.36)	Rastello's drag coefficient, valid over entire spherical and deformable range of covered Re ($1 < Re \lesssim 750$)

Chapter 3

Hydrodynamic Forces Acting on Side-by-side Rising Spherical Bubbles

Two bubbles rising in a side-by-side configuration are investigated. Whereas bubbles above a Reynolds number (Re) of $\sim$ 50 show attraction due to a Venturi effect, repulsion can be seen for Re $\lesssim$ 30 caused by vorticity interactions and flow blockage. The drag coefficient for bubble pairs at low Re (Re $\lesssim$ 10) has both numerically [25] and experimentally [30] been observed to be lower than for single bubble rise. Nevertheless, a clear explanation of the phenomenon is not yet present in current literature. Simulations are carried out in Basilisk for bubbles pairs at Re $\sim$ 1, showing a fundamentally different pressure field development than for bubbles at larger Re. Additionally, the upward fluid velocity through the gap between the two low Re (Re $\sim$ 1) bubbles is larger than that of bubble pair at Re = 13. Further research into the fluid velocity evolution, pressure evolution and separation mechanism for bubble pairs at low Re appears to be vital for a deeper understanding of the underlying physics.

3.1 Introduction

As a follow-up on the material covered in the literature study of Chapter 1, side-by-side bubble rise will be investigated in-depth. The attractive and repulsive behaviour will theoretically and numerically be analysed. In addition, low Re side-by-side bubble rise is simulated, for which it is not yet well-documented why a bubble pair may achieve higher rise velocities than a single bubble. Basilisk simulations aim to create a comparison with bubbles rising at higher Re to describe a variety of consequences and possibly causes of this behaviour. To do this, the (fluid) velocity field, pressure field, vorticity field and separation distance over time will be analysed.

3.2 Types of Bubble Interaction

Once a second bubble is introduced into the environment of a single rising bubble, the characteristics of the bubble behaviour may change quite drastically. In their studies, Kong et al. [30] and Mirsandi et al. [39] distinguish between three types of bubbles: spherical, ellipsoidal (deformed) and deformable bubbles, each showing different interactive behaviour. As described by Legendre et al., rising spherical bubble pairs at low Re (Re $\lesssim$ 30) were seen to repel each other [25]. The vorticity distribution around one of the bubbles is compressed due to the presence of the other bubble, causing flow blockage and a repulsive transverse force [39, 91]. The experiments from Kong et al. [30] confirmed the existence of an increased rising velocity for a pair of spherical bubbles compared to a single spherical bubble. Legendre; Magnaudet, and Mougin [25] attributed this effect to the alteration of the vorticity distribution.

Larger spherical bubbles at increased Re have experimentally (Kok [96]) and theoretically (Van Wijngaarden [97]) shown to attract each other [30]. The interaction between the larger spherical bubbles is essentially the same as for the second type of bubbles: deformed bubbles having a relatively stable ellipsoidal shape (Re $\sim$ 100, $\chi \sim 1.5$) [30]. At these larger Reynolds numbers, vorticity is diffused better around the bubble and advected downstream [25]. However, Magnaudet and Mougin [98] describe that an aspect ratio of 1.65 would have to be exceeded for a standing eddy to occur, which is a sign of the vorticity accumulation behind the bubble pair. Therefore, instead of any vorticity interactions, the Venturi effect in the gap between the bubbles, where a pressure drop due to increased fluid velocity causes the attractive force between the bubbles, is deemed to be the main driving force for bubble interaction [25, 39, 44]. Once the bubbles are in each other's vicinity, the bubbles may either coalesce or repel. During the 'kissing' of the bubbles, vortex pairs can be created in the gap during the collision, generating lift forces that may separate the bubbles [39] if coalescence has not occurred yet. In the study of Kong et al. [30], deformed bubbles only showed attractive behaviour for low separation distances ($S \sim 3$), where S indicates the distance in bubble radii between the centres of the two bubbles (i.e., bubbles touch for $S = 2$). For $S > 4$, weak interaction was seen, leading to almost the same rise behaviour as a single rising bubble. Therefore, the lift between two bubbles can be seen to be a function of both Re and S.

In contrast to the other two bubble types, larger deformable bubbles (at Re $\gtrsim$ 200) may undergo significant shape oscillations during their rise due to wake interactions [30, 39], which could subsequently lead to zigzagging of both bubbles. Mirsandi et al. [39] analysed the wake structures of the bubble pair to obtain insight into the underlying mechanics. After the initial attraction, vorticity accumulation at the inner sides of the bubbles causes a repulsive force (vortex-induced lift force), as was the case with the deformed bubbles. In this case, however, additional vortex pairs are generated at the outer sides of the bubbles, causing a tilt and, thus, a zigzagging motion. Depending on the Reynolds number of the bubble pair, the zigzagging motion might die out quickly as the vortex structures for each bubble start to show similarities with that of a single bubble after some time [39].

3.3 Drag, Added Mass and Lift for Spherical Bubble Pairs

While the buoyancy for each of the two bubbles is the same as for a single bubble, the added mass and the drag are changed due to the bubbles interacting with each other. Additionally, a lift force between the bubbles can be defined that describes whether attractive or repulsive behaviour occurs. These different components will be elaborated in the following section for spherical bubbles.

3.3.1 Drag Force

In the limit of irrotational flow (Re = ∞), Kok [99] derived the following expression for the drag coefficient [25]:

$$C_D = \frac{48}{Re}\left[1 + g(S)\right] + \mathcal{O}\left(Re^{-3/2}\right), \tag{3.1}$$

with:

$$g(S) = S^{-3} + \frac{3}{4}S^{-6} + \frac{11}{3}S^{-8} + \frac{1}{2}S^{-9} + \frac{39}{4}S^{-10} + \mathcal{O}\left(S^{-11}\right), \tag{3.2}$$

Subsequently, based on the numerical simulations from Legendre; Magnaudet, and Mougin [25], Hallez and Legendre [44] derived the drag at moderate Re ($50 \leq Re \leq 500$) by adding the potential viscous expression from Kok to Moore's expression for the drag coefficient of a bubble pair, yielding:

$$C_{D,1} = C_{D,2} = \frac{48}{Re}\left[1 + S^{-3} - \frac{3}{4}S^{-6} + \cdots - \frac{2.21}{\sqrt{Re}}\right], \tag{3.3}$$

where subscripts 1 and 2 indicate the left and right bubble, respectively. For high S, Moore's drag expression given by Equation (2.9) from Chapter 2 is achieved while low S can be seen to raise the drag due to an increased fluid strain rate between the two bubbles [25].

At low Reynolds numbers, the expression for Moore's drag coefficient yields incorrect behaviour as described in Chapter 2. Therefore, the limit for low Re should be investigated further. At low Reynolds numbers, the drag coefficient can be given as:

$$C_D(Re, S) = \frac{16}{Re}\left(1 + \frac{Re}{8} - \frac{1}{2}\frac{e^{-ReS/4}}{S}\right), \tag{3.4}$$

which is based on the theory from Vasseur and Cox [100], originally derived for two rigid spheres [25]. For large S, i.e. a single rising bubble, the negative term in the expression vanishes, while for bubbles in the vicinity of each other, the negative term will lower the drag force on the bubble pair. In other words, the interaction between the two bubbles at low Reynolds numbers may cause an increased terminal rise velocity compared to a single rising bubble, which was also seen in the experiments of Kong et al. [30]. This behaviour is the opposite of the limit of irrotational flow, where any (close) interaction between the bubbles yields an increased drag. The reason, however, for two bubbles at low Re experiencing a lower drag force is not well-understood. Legendre; Magnaudet, and Mougin [25] describe that this behaviour is caused by "vorticity generated by the shear-free condition at the bubble surface", but further elaboration is not given. To the author's best knowledge, such an explanation is also not present in further literature. In Section 3.4.2, the phenomenon will be investigated by making use of simulations carried out by Basilisk.

In Figure 3.1, the drag coefficient of a bubble pair (C_D) is compared to the drag of a single bubble ($C_{D,\infty}$ as $S \to \infty$). The simulations from Legendre; Magnaudet, and Mougin [25] show the described behaviour in the limit of high and low Re. For $Re \lesssim 10$, a drag coefficient ratio lower than one can be seen, indicating an increased terminal rise velocity for the bubble pair

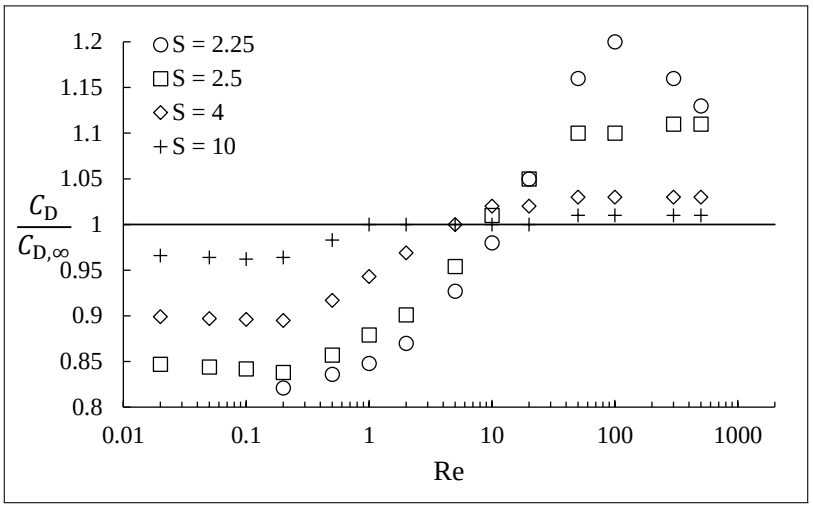

FIGURE 3.1: Drag coefficient ratio as a function of the Reynolds number for various separations, where (C_D) holds for a bubble pair and ($C_{D,\infty}$) for a single bubble. The results are obtained numerically by Legendre et al. [25].

compared to a single bubble. For Re $\gtrsim$ 20, the ratio is shown to be larger than one for any separation value, agreeing with the behaviour for irrotational flow as given by Kok. For $S = 10$, the drag coefficient ratio can be seen to be close to one for any value of Re, indicating the reduced interaction between bubbles located far away from each other.

3.3.2 Added Mass

For a single spherical bubble, the added mass coefficient is equal to 0.5, taking into account that in addition to the bubble, the fluid around the bubble has to be accelerated as well [69]. With the introduction of a second bubble, the fluid in between the two bubbles experiences an increased acceleration, such that the added mass coefficient increases as predicted by irrotational theory, shown by Van Wijngaarden [97] & Kok [99] [25]:

$$C_M(S) = \frac{1}{2}\left(1 + \frac{3}{2}S^{-3} + \frac{3}{4}S^{-6} + 3S^{-8} + \frac{3}{8}S^{-9} + \frac{27}{4}S^{-10}\right) + \mathcal{O}\left(S^{-11}\right). \tag{3.5}$$

In Chapter 2, it was described that the initial acceleration for any single bubble rising from rest is equal to $2g$. With the inclusion of another bubble in the vicinity of the first bubble, the added mass coefficient is increased (to 0.53 at $S = 3$, for instance), yielding decreased initial acceleration and, thus, a lower rise velocity in the acceleration regime. The evolution of the rise velocity of different-sized bubble pairs is further elaborated in Section 3.4.

3.3.3 Lift Force

While the two previous force terms already existed for single bubble rise, the inclusion of a second bubble also leads to the introduction of a lift force between both bubbles. Hallez and Legendre [44] defined the lift coefficient for a bubble pair based on the numerical work of Legendre; Magnaudet, and Mougin [25] for moderate Re ($50 \leq \text{Re} \leq 500$) by adapting the irrotational expression from Van Wijngaarden [97]:

$$C_{L,1} = 6S^{-4}\left(1 + S^{-3} + \frac{16}{3}S^{-5} + \cdots - \frac{40}{\text{Re}}\right). \tag{3.6}$$

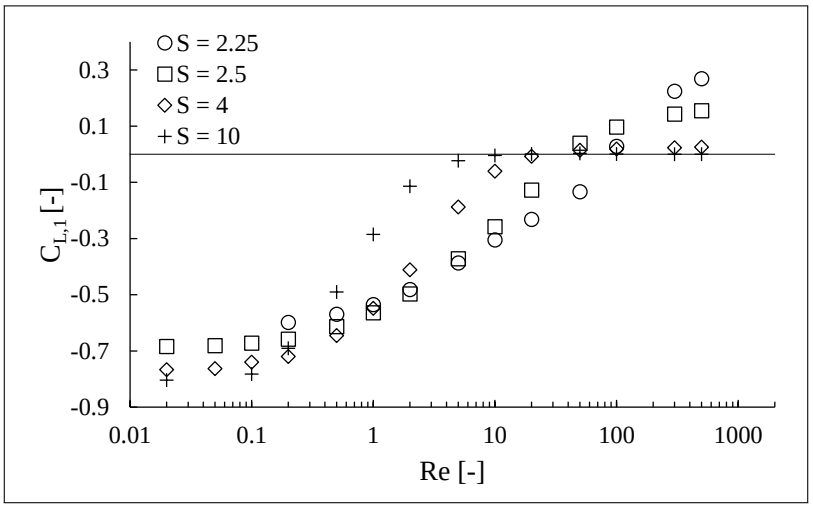

FIGURE 3.2: Lift coefficient of a the left bubble ($C_{L,1}$) as a function of the Reynolds number for various separations, where a positive lift coefficient indicates attraction. The results are obtained numerically by Legendre; Magnaudet, and Mougin [25].

The effect of decreasing Re can be seen to lower the lift coefficient for the left bubble, thus resulting in less attractive interaction between both bubbles compared to high Re. For both lift coefficient expressions in this section, the lift force approaches zero as $S \to \infty$, agreeing with the idea of no lift force being present for a single bubble rising in a straight line.

For low Reynolds numbers, the lift coefficient is given by Legendre; Magnaudet, and Mougin [25] and Vasseur and Cox [100]:

$$C_{L,1}(\mathrm{Re}, \mathrm{Re}S) = -\frac{32}{\mathrm{Re}^2 S^2}\left[1 - \left(1 + \frac{\mathrm{Re}S}{4}\right)\mathrm{e}^{-\mathrm{Re}S/4}\right]. \tag{3.7}$$

In contrast to Equation (3.6), $C_{L,1}$ obtained from Equation (3.7) is negative for any combination of Re and S, such that the interaction is repulsive instead of attractive [25]. This result agrees with the idea of flow blockage at low Re due to the produced vorticity, leading to repulsion. Additionally, smaller separation values can be seen to lead to a more negative lift coefficient and, therefore, more repulsion.

The lift coefficient over a range of Re and various separations is shown in Figure 3.2, which shows the numerical results from Legendre; Magnaudet, and Mougin [25]. At about a Reynolds number of 50, a transition between a positive and negative lift coefficient can be seen, leading to attraction for $\mathrm{Re} \gtrsim 50$ and repulsion for $\mathrm{Re} \lesssim 30$ for any separation distance. Small separation values can be seen to lead to a larger lift coefficient over a large range of Re, agreeing with the theoretical results from the two equations.

Interaction for Non-aligned Side-by-side Bubbles

In addition to rising perfectly horizontally side-by-side, bubbles may rise as well with an angle θ between their centreline and rise direction (see Figure 3.3). Between the well-defined in-line rise ($\theta = 0°$) and side-by-side rise ($\theta = 90°$), different effects may occur. Kok [99] defines a critical angle θ^* ranging between 35.0° for $S = 2$ and 54.7° for $S \to \infty$. For $\theta^* < \theta < 180 - \theta^*$ bubbles are described to always attract each other in the potential flow limit. Even for the other orientations, a hydrodynamic moment will always cause the bubbles to adopt a 90° angle [99]. The numerical work from Hallez & Legendre [44] confirms the side-by-side configuration to be the (only) stable position for two interacting rising bubbles over a large range of Reynolds numbers ($20 \leq \mathrm{Re} \leq 500$) and separations ($2.5 \leq S \leq 10$). The existence of a critical angle as

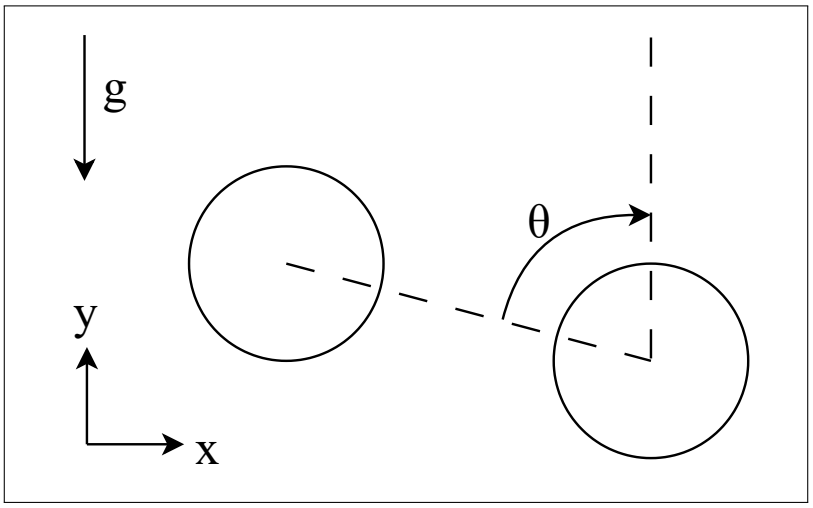

FIGURE 3.3: Definition of the angle (θ) between the two rising bubbles.

theorised by Kok was established as well by Hallez & Legendre: for Re $\geq$ 50, bubbles were attracted for $\theta^* < \theta < 180 - \theta^*$ with $\theta^* = 37°$.

3.4 Basilisk Results

3.4.1 Bubble Interaction Behaviour for Re $\gtrsim$ 10

The interaction between side-by-side rising bubbles is qualitatively investigated in Basilisk. Figures 3.4 to 3.6 show the evolution of the fluid velocity, vorticity field and pressure field for two 0.3 mm bubbles, respectively. A negative fluid velocity through the bubble gap can be seen in Figure 3.4.a, which will initially lead to a slightly attractive force. The attraction appears to occur since the vorticity asymmetry has not yet fully developed, as can be seen in Figure 3.5.a. Once the expected asymmetry starts to evolve (Fig. 3.5.b), almost no fluid is accelerated anymore through the gap (Fig. 3.4.b) due to vorticity blocking the fluid flow. Subsequently, a decreased pressure is achieved at the outside of the bubbles compared to the pressure in the gap, which is indicated by the darker blue colour around the outer sides of the bubbles in Figure 3.6.b. This pressure drop will then be the onset of the repulsive behaviour, indicated by the fact that the bubbles start to separate as shown in the last column of figures. The repelling motion slowly eliminates the asymmetry in vorticity, resulting in the growth of the inner vorticity field as shown in Figure 3.5.c. The flow blockage in the gap is eliminated afterwards, resulting again in a downward fluid motion (Fig. 3.4.c).

Figures 3.7 to 3.9 show the attractive behaviour between two 0.5 mm bubbles. Similar to the repulsive case, fluid acceleration through the gap occurs again (Fig. 3.7.a). In contrast, however, the vorticity evolution during rise is significantly more symmetric. Due to the higher rise velocity, more vorticity is diffused towards the back of the bubble, creating a narrower inner vorticity field which interacts less with the inner vorticity field of the other bubble [25] (Figs. 3.8.a & 3.8.b). Therefore, no flow blockage will occur, as can be seen by the relatively large negative fluid velocity through the gap in Figure 3.7.b. The accelerated fluid leads to a lower pressure in the gap than the surrounding fluid by Bernoulli's principle (Fig. 3.9.b), such that attraction takes place. In the last column of figures, the moment just before coalescence occurs is shown. Even while the bubbles are this close to each other, the vorticity field remains remarkably symmetric (Fig. 3.8.c).

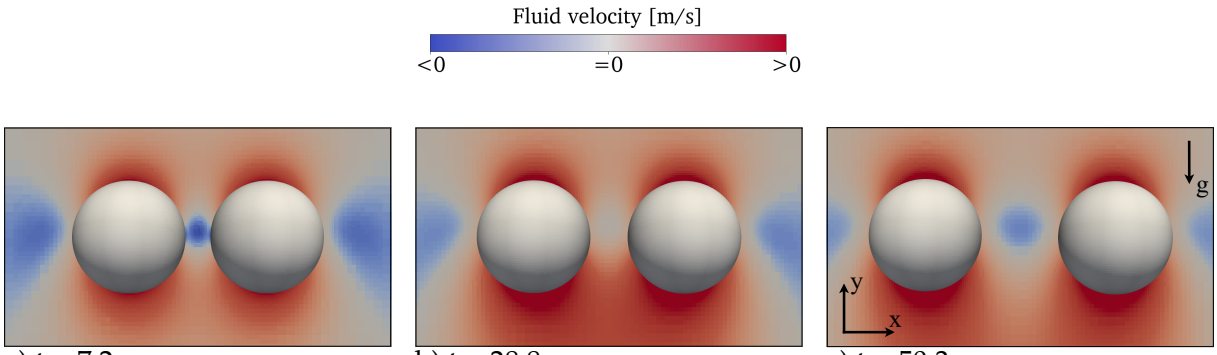

a) t = 7.2 ms b) t = 28.8 ms c) t = 50.3 ms

FIGURE 3.4: Repulsion: evolution of the fluid velocity during rise for two 0.3 mm diameter bubbles with an initial separation of 2.5. Figure c) shows the orientation used for all simulation snapshots in this study.

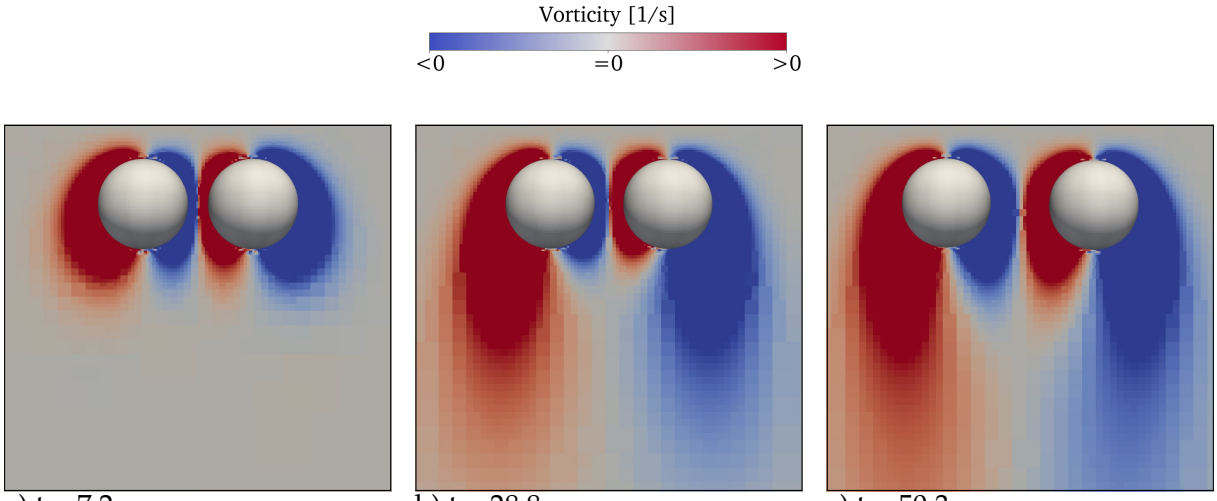

a) t = 7.2 ms b) t = 28.8 ms c) t = 50.3 ms

FIGURE 3.5: Repulsion: evolution of the vorticity field created at the bubble surfaces during rise for two 0.3 mm diameter bubbles with an initial separation of 2.5.

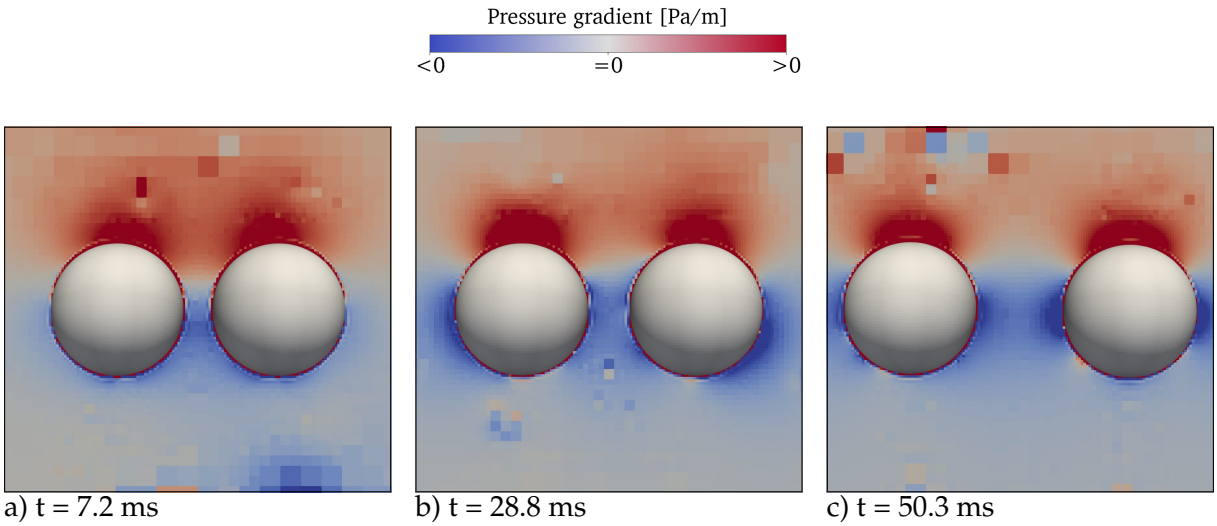

a) t = 7.2 ms b) t = 28.8 ms c) t = 50.3 ms

FIGURE 3.6: Repulsion: evolution of the pressure field during rise for two 0.3 mm diameter bubbles with an initial separation of 2.5.

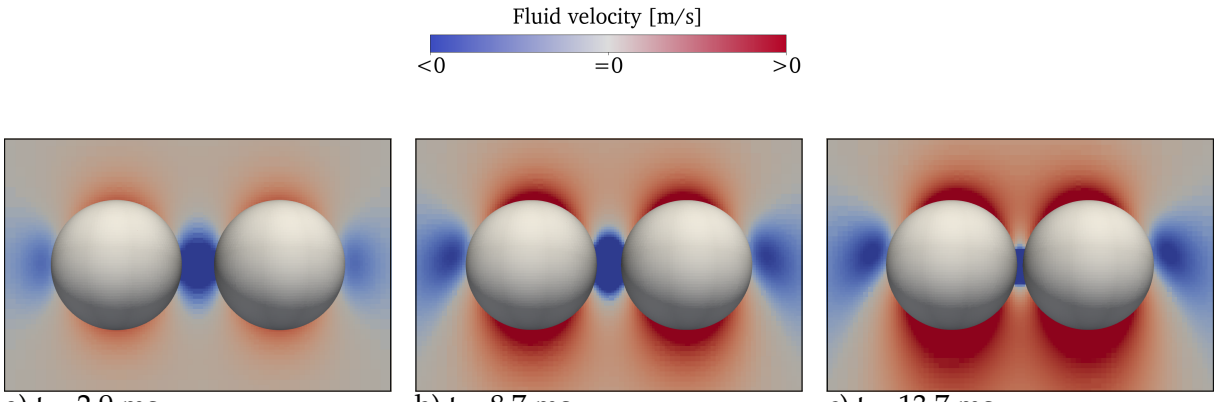

a) t = 2.9 ms b) t = 8.7 ms c) t = 13.7 ms

FIGURE 3.7: Attraction: evolution of the fluid velocity during rise for two 0.3 mm diameter bubbles with an initial separation of 2.5.

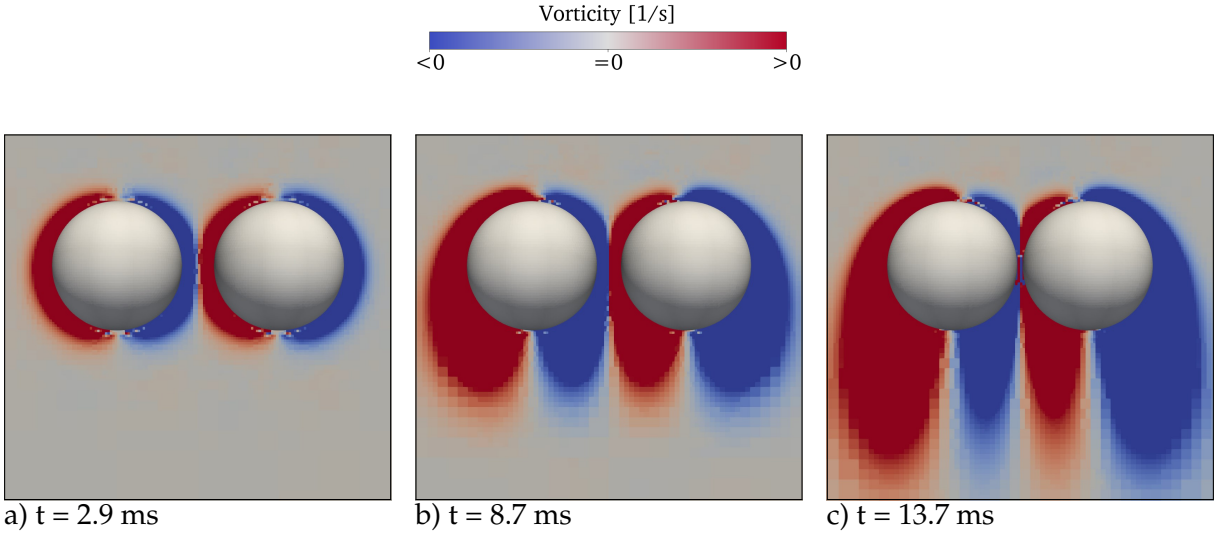

a) t = 2.9 ms b) t = 8.7 ms c) t = 13.7 ms

FIGURE 3.8: Attraction: evolution of the vorticity field created at the bubble surfaces during rise for two 0.3 mm diameter bubbles with an initial separation of 2.5.

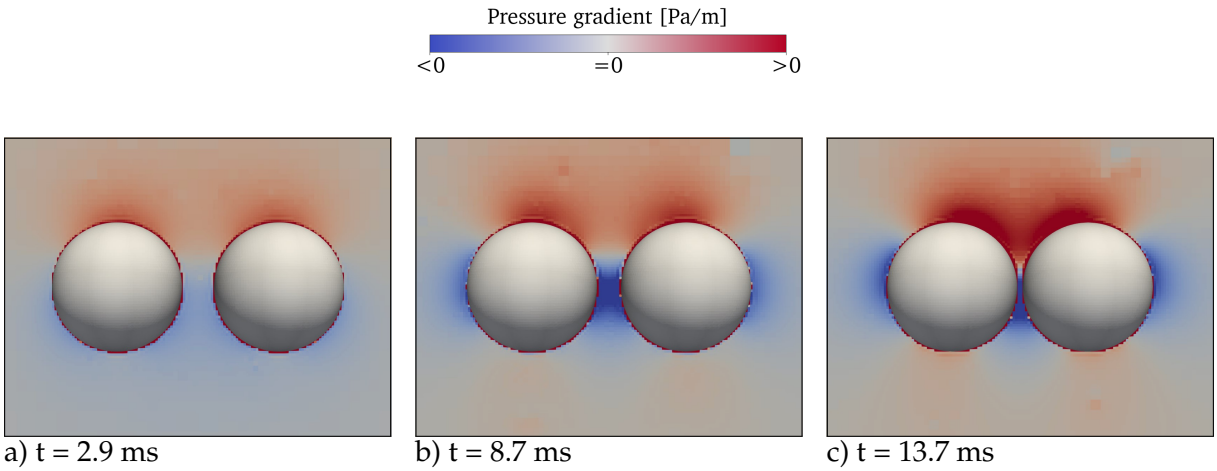

a) t = 2.9 ms b) t = 8.7 ms c) t = 13.7 ms

FIGURE 3.9: Attraction: evolution of the pressure field during rise for two 0.3 mm diameter bubbles with an initial separation of 2.5.

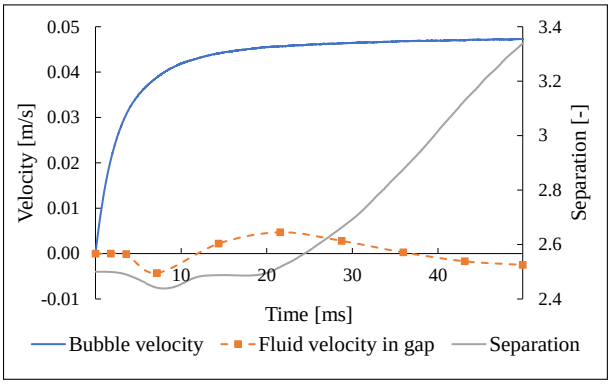

FIGURE 3.10: Vertical velocity evolution of a 0.3 mm bubble and the fluid in the centre of the gap (left axis) and the separation evolution (right axis) as simulated by Basilisk.

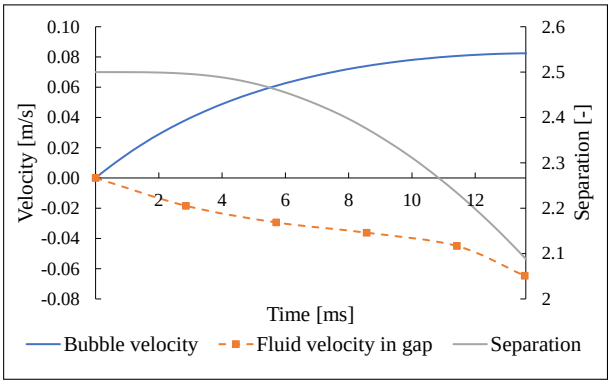

FIGURE 3.11: Vertical velocity evolution of a 0.5 mm bubble and the fluid in the centre of the gap (left axis) and the separation evolution (right axis) as simulated by Basilisk.

Evolution of Velocity and Separation Distance

Figures 3.10 & 3.11 show the development of the bubble velocity, the vertical fluid velocity through the centre point of the gap (both on the left axis) and the separation distance between the bubbles (on the right axis) for the two cases. Here, the fluid velocity (in orange) is obtained from several simulation snapshots (the squares) with the dotted line creating a fit through the measurements. The bubble rise velocity and separation are printed each simulation step, creating a continuous evolution. From Figure 3.10, it is evident that an initial negative fluid velocity leads to an attractive force between both 0.3 mm bubbles as discussed earlier. Once the fluid velocity in the gap starts to become positive, the separation distance can be seen to increase as well, following the expected repulsive behaviour. At approximately 35 ms, when the bubbles have repelled each other ~ 0.4 bubble radius, the fluid velocity becomes negative again, which is the onset of the bubble pair settling in its equilibrium position.

Compared to the bubble rise velocity, the fluid velocity achieves values of only 10% of the bubble velocity (0.0047 vs 0.047 m/s). The 0.5 mm bubble pair, on the other hand, shows significantly larger relative (negative) fluid velocities compared to the bubble rise velocity, as shown by Figure 3.11. Starting from 50%, the negative fluid velocity grows to almost 80% of the rise velocity just before coalescence. A steeper decrease in fluid velocity can be seen around $t = 11$ ms when the separation distance has lowered to $S \sim 2$. This decrease is likely caused by the bubbles approaching each other relatively quickly during the later stages, squeezing out any fluid before coalescence occurs. Such squeezing amplifies the already existing Venturi effect, creating an increased negative fluid velocity through the gap.

3.4.2 Bubble Interaction Behaviour for Re $\lesssim$ 10

For large enough Reynolds numbers (Re $\gtrsim$ 10), bubble interaction results in an increase of the drag coefficient compared to a single bubble as a higher strain rate in the fluid between the two bubbles is obtained [25, 51]. Figures 3.12 & 3.13 show the rise velocity evolution for the 0.3 & 0.5 mm bubble pair where the rise velocity of the two previously covered bubble pairs is lower over the entire acceleration phase compared to a single bubble. Lowering the Reynolds number to approximately within the Stokes regime should lead to the rise velocity of a bubble pair being higher than that of a single bubble as was indicated by Legendre; Magnaudet, and Mougin [25] and experimentally validated by Kong et al. [30]. Since this behaviour might appear to be counter-intuitive, simulations are carried out to aim for additional insight into the mechanisms at play.

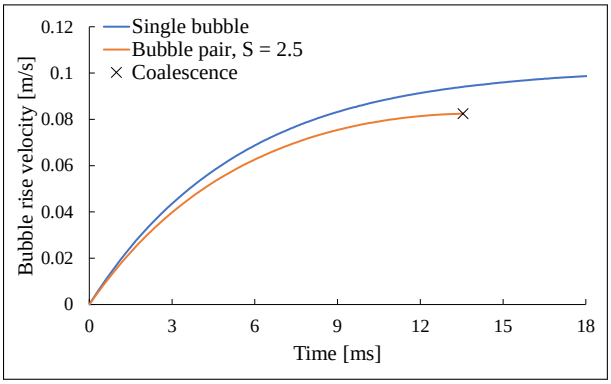

FIGURE 3.12: Rise velocity of a single 0.3 mm diameter bubble and a same-sized bubble pair with $S = 2.5$ as simulated by Basilisk.

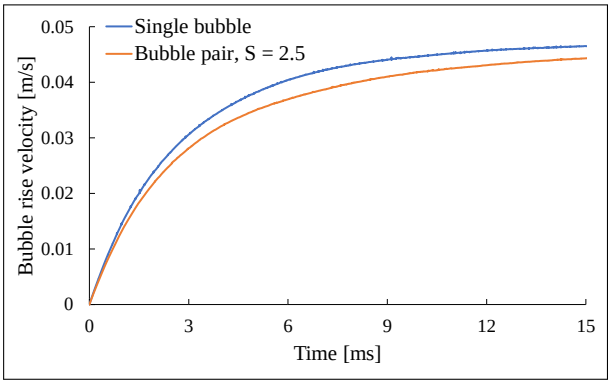

FIGURE 3.13: Rise velocity of a single 0.5 mm diameter bubble and a same-sized bubble pair with $S = 2.5$ as simulated by Basilisk.

To prevent small-scale dynamics from causing large simulation times, the rise of a 0.5 mm bubble pair is simulated. Instead of the standard viscosity of water, however, the viscosity is multiplied by 10 ($\mu_L = 10\mu_{water}$), resulting in Re = 0.86 at the terminal rise velocity of a single bubble. Figure 3.14 reveals that the simulated bubble pair achieves a larger rise velocity over time than the single bubble. Although the rise velocity of the single bubble initially exceeds that of the bubble pair, the bubble pair sustains an increased acceleration until the terminal rise velocity is reached. The transition behaviour can be explained by analysing the spherical bubble rise velocity formulas from Chapter 2:

$$V_T = \sqrt{\frac{\frac{4}{3}\pi R_b^3 \rho_L g}{\frac{\pi}{2}\rho_L R_b^2 C_D}} = \sqrt{\frac{8R_b g}{3C_D}}, \tag{3.8}$$

$$V_n = V_{n-1} + \Delta t \left(\frac{g}{C_m} - \frac{3}{8}\frac{C_D(V_{n-1})V_{n-1}^2}{R_b C_m} \right). \tag{3.9}$$

Here, Equation (3.8) indicates the terminal rise velocity and Equation (3.9) the rise velocity over time. Besides the added mass, buoyancy & drag, the lift force also plays a role in side-by-side bubble rise. It might initially seem that the lift force has no influence on the (terminal) rise velocity. The bubble pair experiences stable rise (no zigzagging or spiralling motion) at low Reynolds numbers, such that the bubbles will not undergo any rotation, causing the lift to always act perfectly perpendicular to the rise motion of the bubbles. On the other hand, the drag coefficient and added mass coefficient are a function of the separation S. Since the lift force determines how much S changes over time, the rise velocity is indirectly influenced by the lift force. However, as the separation increases only slightly until the terminal velocity is reached, as shown in Figure 3.15, the lift effect will be neglected in the force balances.

From the two above formulas, one can deduce that the only variables that may be altered when analysing side-by-side rise are the drag coefficient at terminal rise velocity and the added mass coefficient & drag coefficient for the rise velocity over time. These factors were already covered earlier, illustrating that C_D is lowered for side-by-side rise at low Re, while C_M is increased. An increased C_M causes more fluid to be accelerated by the bubble, causing an increased acceleration duration until the terminal velocity is reached. Therefore, the effect of increased C_M initially causes a lower rise velocity as was seen in Figure 3.14. As the bubble pair approaches the terminal velocity, the effect of the increased added mass coefficient decreases: C_M is namely not a factor in the expression for the terminal rise velocity (Eq. (3.8)).

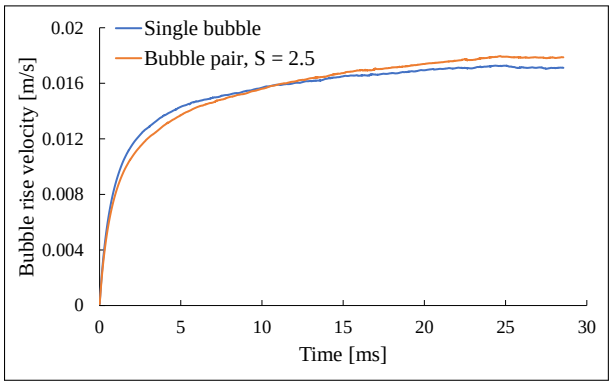

FIGURE 3.14: Rise velocity of a single 0.5 mm diameter bubble and a similar-sized bubble pair as simulated by Basilisk. Instead of the viscosity of water, the viscosity is increased 10-fold to achieve Re $\approx$ 1 at terminal velocity.

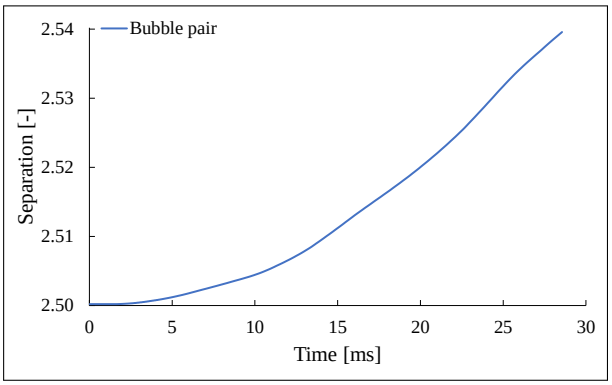

FIGURE 3.15: Evolution of the separation distance between two 0.5 mm diameter bubbles with $\mu_L = 10\mu_{water}$ as simulated by Basilisk.

Figure 3.16 shows the theoretical rise velocity of a single 0.5 mm air bubble in a fluid with ten times the viscosity of water ($\mu_L = 10\mu_{water}$) and a bubble pair (with S=2.5) by Eq. (3.9). To determine the effect of solely the added mass coefficient on bubble rise (which is 0.55 for the bubble pair and 0.5 for a single bubble), the drag coefficient expression for a single bubble is used instead of the side-by-side drag coefficient (Eq. (3.4)) for the bubble pair. As discussed, Figure 3.16 shows a lower rise velocity during the early stages of bubble rise. Although the single bubble obtains the terminal velocity sooner, the bubble pair achieves the same terminal rise velocity after an elongated period.

Figure 3.14 shows that the lower rise velocity lasts to approximately 10 ms. Since the rise velocity is now relatively close to the terminal value, the effect of the increased added mass for the bubble pair becomes relatively small. The result of the decreased drag coefficient, on the other hand, can now be noticed. The effect appears to be small during the early stages of bubble rise, such that the single bubble can obtain a higher rise velocity. The simulated rise velocity of the bubble pair eventually reaches a 4.3% higher value (1.71 cm/s vs. 1.79 cm/s) than the single bubble. Subsequently, the theoretical C_D reduction to cause the terminal rise velocity increase can be calculated by utilising Equation (3.4) with the accompanying Re (0.85 and 0.89, respectively) and S (80 and 2.5, respectively) for the single bubble and the pair (a separation distance of 80 can be used to obtain the result for a single bubble [25]). The C_D ratio can then be calculated to be:

$$\frac{C_D(0.89, 2.5)}{C_{D,\infty}(0.85, 80)} = \frac{17.9}{20.7} = 0.863 \tag{3.10}$$

The numerical analysis from Legendre; Magnaudet, and Mougin [25] achieved an approximate $C_D = 0.88C_{D,\infty}$ for Re = 1 (Fig. 3.1), which agrees reasonably well with the value obtained from the Basilisk simulations.

Graphical Analysis of Low Re Rise Behaviour

Figures 3.17 to 3.19 show the evolution of the fluid velocity, vorticity field and pressure field for the low Re bubble rise. When compared to the 0.3 mm bubble pair (which does not show an increased rise velocity for the bubble pair compared to a single bubble), several similarities can be seen. Figures 3.17.a to 3.17.c show a positive fluid velocity through the gap as well due to the generated vorticity producing upward velocities [25]. Additionally, a similar, albeit smaller development of the vorticity asymmetry can be distinguished from Figures 3.18.a to 3.18.c, creating the flow blockage. Deviations between the 0.3 mm bubble pair and the low Re case are

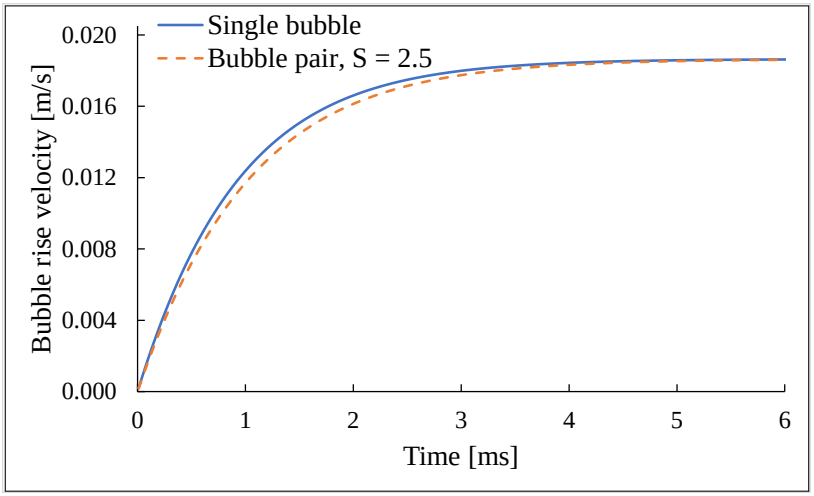

FIGURE 3.16: The theoretical effect of the altered added mass coefficient of a bubble pair on the rise velocity compared to a single bubble. In both cases, the diameter is 0.5 mm and $\mu_L = 10\mu_{water}$. Additionally, the single bubble drag coefficient is used for the bubble pair to focus on the influence of C_M.

also revealed from the figures. Whereas a negative fluid velocity appeared at the early and late time steps for the former case, the latter appears to only obtain positive fluid velocities through the gap. The most striking contrast, however, can be observed in the pressure fields. Previously, the pressure showed to be minimum around the outer side surface of the bubbles (leading to repulsion) or in the gap (leading to attraction), while the current case shows a pressure drop at the aft side of the bubbles (Figs. 3.19.a to 3.19.c). The fluid velocity around the bubble is minimal, whereas the previous cases showed a noticeable negative fluid velocity around the bubble. It is thought that only a small amount of decreased pressure is developed at the sides of the bubble due to the lack of fluid acceleration in the viscous flow regime. The absence of a decreased pressure at the outer side surfaces of the bubbles raises two questions: 1.) what mechanism is responsible for bubble interaction and 2.) how the pressure drop at the back of the bubbles is related to a decreased drag coefficient of the pair. These questions could be an interesting starting point for further research into the low Re bubble rise.

Evolution of Velocity and Separation Distance

The simulated low Re behaviour, given by Figure 3.20, shows no sign of any attraction between the bubbles, although a negative fluid velocity occurs at the early stages. A monotonic increase in the separation can be seen, displaying fundamentally different behaviour than the 0.3 mm case. However, since the separation distance is small compared to the other two cases (see Figure 3.21), it is uncertain whether repulsion is the final resulting behaviour of this interaction. Furthermore, the fluid velocity in the gap obtains up to 50% of the bubble rise velocity (0.0086 vs 0.018 m/s), compared to a maximum of 10% for the 0.3 mm bubble pair (0.0047 vs 0.047 m/s). Even though the bubble rise velocity of the 0.3 mm case is 2.5 times higher than the low Re case, the fluid velocity is almost 2 times lower. Whether this effect originates from the decreased drag coefficient or causes it, is to be determined.

Figure 3.21 shows the separation evolution for the three different cases. While repulsion and attraction can be distinguished clearly for the 0.3 mm and 0.5 mm bubble pair, respectively, the low Re rise case does not yet show an apparent interaction direction. Although a very slight repulsion can initially be seen, a longer simulation time would be required to ensure no attraction takes place quickly afterwards.

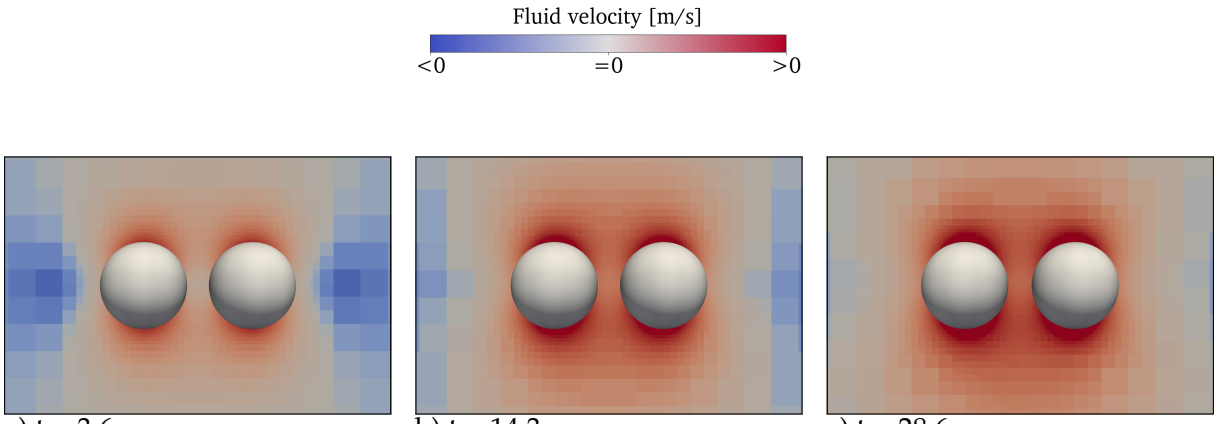

a) t = 3.6 ms b) t = 14.3 ms c) t = 28.6 ms

FIGURE 3.17: Repulsion: evolution of the fluid velocity during rise for two 0.5 mm diameter bubbles with an initial separation of 2.5 and $\mu_L = 10\mu_{water}$.

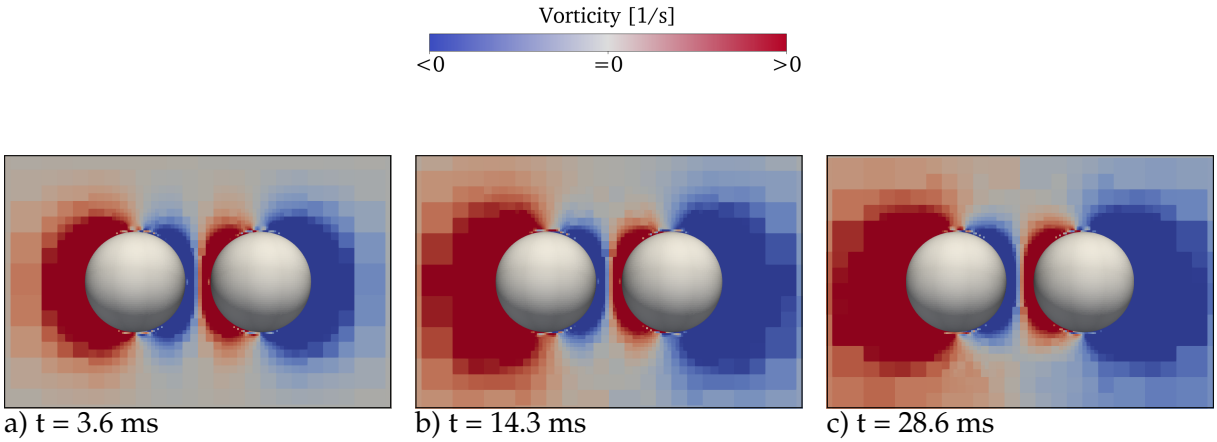

a) t = 3.6 ms b) t = 14.3 ms c) t = 28.6 ms

FIGURE 3.18: Repulsion: evolution of the vorticity field created at the bubble surface during rise for two 0.5 mm diameter bubbles with an initial separation of 2.5 and $\mu_L = 10\mu_{water}$.

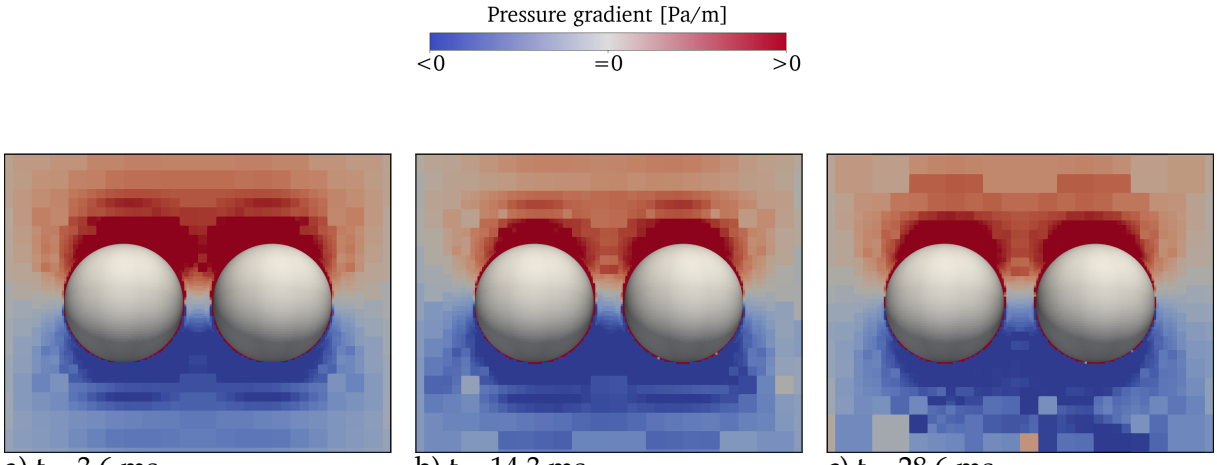

a) t = 3.6 ms b) t = 14.3 ms c) t = 28.6 ms

FIGURE 3.19: Repulsion: evolution of the pressure field during rise for two 0.5 mm diameter bubbles with an initial separation of 2.5 and $\mu_L = 10\mu_{water}$.

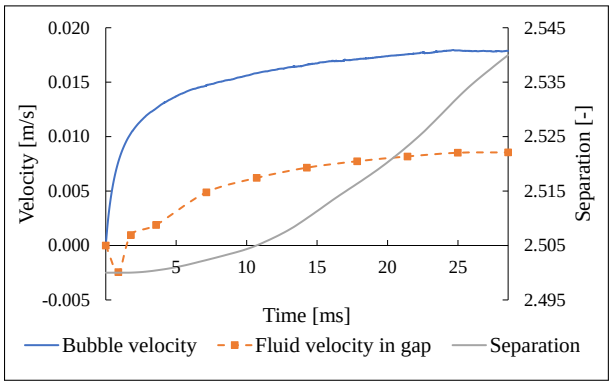

FIGURE 3.20: Vertical velocity evolution of a 0.5 mm bubble and the fluid (with $\mu_L = 10\mu_{water}$) in the centre of the gap (left axis) and the separation evolution (right axis) as simulated by Basilisk.

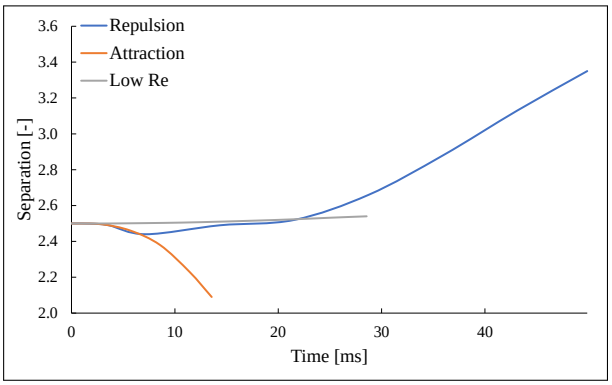

FIGURE 3.21: Separation evolution of the three different cases.

3.5 Conclusion and Outlook

Even though single bubbles rise in a straight fashion at low enough Re ($Re \lesssim 750$ [18]), bubble interactions between two spherical rising bubbles occur already at significantly lower Re. For $Re \gtrsim 50$, attraction between a bubble pair occurs, caused by a Venturi effect in the gap between the bubbles, accelerating the fluid. By Bernoulli's principle, the pressure of the accelerated fluid is lowered, resulting in an attractive force between the bubbles. For $Re \lesssim 30$, repulsion between the bubbles takes place. Vorticity is not easily diffused towards the back of the bubbles due to the low rise velocity. The vorticity interactions inside the gap cause the downward fluid to be blocked, which creates an upward flow [25]. The pressure gradient is now inverted compared to the attractive case, causing the bubbles to experience a repelling force. Once the bubbles have separated sufficiently far, the vorticity interactions are reduced, removing the flow blockage. Fluid acceleration through the gap occurs again, resulting in an attractive force and the onset of an equilibrium distance between the two bubbles. Simulations by Basilisk showed the upward fluid velocity for the separation case (0.3 mm bubbles) to be at maximum 10% of the bubble rise velocity. This finding is in sharp contrast to the case of attraction (0.5 mm bubbles), where the downward fluid velocity achieves 80% of the bubble rise velocity just before coalescence. These results suggest the influence of vorticity causing the upward fluid flow to be significantly less than the fluid flow caused by attraction between a bubble pair.

Legendre; Magnaudet, and Mougin [25] carried out numerical simulations on two bubbles rising side-by-side, showing that the drag coefficient of a bubble pair becomes lower than that of a single bubble below a Reynolds number of approximately 10. Simulations carried out in Basilisk confirmed that bubble pairs at $Re > 13$ show a decreased rise velocity compared to a single bubble, while at $Re \approx 1$ the opposite behaviour was seen. Since the exact workings of the increased rise velocity at low Re are not described well in literature, additional simulations were done to gather extra insight. It was shown that the upward fluid velocity through the gap for the low Re bubble pair is larger than that of the 0.3 mm bubble pair, suggesting stronger vorticity interactions at lower Re. However, this notion is somewhat contradictory since the rise velocity for the low Re bubble pair is 2-3 times lower than the 0.3 mm bubbles, creating less 'powerful' vortices even though larger upward fluid velocities are achieved.

Moreover, a deviation in the pressure field between the low Re and 0.3 mm case could be seen. While the latter shows a clear pressure drop at the side surfaces of the bubbles, the former shows an area of decreased pressure at the aft side of both bubbles. How the aft pressure drop influences the drag on the bubble pair and what mechanism causes the bubble interaction in the absence of decreased pressure at the bubble sides are intriguing questions for further research.

Chapter 4

Conclusion and Outlook

In this thesis, the hydrodynamic forces acting on bubbles have been covered. The literature study of Chapter 1 lays the groundwork for the material studied in the subsequent chapters, covering the main subjects of the thesis. A single bubble might undergo a path instability above a critical bubble diameter ($\sim$ 1.8 mm [1]), resulting in a zigzagging or spiralling motion. The underlying cause for a path instability has been debated for decades. While vortex shedding or the creation of a standing eddy was initially thought to be the origin, the discovery of a regime in which a standing eddy does not occur has led to the notion of a path instability resulting from the interplay between a bubble and its surrounding flow [14]. Furthermore, the interactions between side-by-side or in-line rising bubbles have been established. For side-by-side rise, a Venturi effect due to fluid acceleration in the gap between the bubbles leads to attraction, whereas flow blockage caused by vorticity interactions yields repulsion. An equilibrium distance exists for which the attractive and repulsive forces cancel each other, although its existence in in-line rise is still heavily debated.

Subsequently, Chapter 2 focuses on a single bubble below the path instability criterion, causing it to rise steadily. The terminal rise velocity of spherical and deformable bubbles is derived by constructing force balances, retaining a fundamental understanding of the involved physics. For spherical bubbles, the derived terminal rise velocity has a 3.8% error with experimental data and a 1.6% error with simulation data from Basilisk. Deformable bubbles showed small error margins as well, being 2.4% compared to experimental values and 3.1% with the simulations. For larger bubbles (above $\sim$ 1.5 mm in diameter), a greater discrepancy could be seen between simulations and the derived expressions (5.8% error) caused by the (too) coarse grids of the simulations. The same discrepancy at large bubble diameters could be seen in the acceleration regime. By time integration, the rise velocity during the initial stages of a bubble was calculated and compared to Basilisk, showing the best applicability for bubble sizes between 0.5 and 1.5 mm. Below the threshold, the history force should be considered to take into account the history effect of a rising bubble. Above the upper limit, it is interesting to determine to what degree of accuracy finer grids may lead. Additionally, further research into the applicability of the derived expressions for systems other than the covered air bubble in water could be of interest.

Finally, Chapter 3 investigates the interactions between two side-by-side rising bubble in-depth by employing Basilisk. The mechanisms leading to attraction (for two 0.5 mm bubbles) and repulsion (two 0.3 mm bubbles) are thoroughly examined, showing that repelling bubbles might initially show a slight attractive motion. Additionally, the maximum fluid velocity through the gap between the bubbles compared to the bubble rise velocity is significantly higher for bubble attraction ($\sim$ 80 %) than for repulsion ($\sim$ 10 %), indicating a stronger fluid acceleration by the Venturi effect than caused by vorticity interactions. At low Re (Re $\lesssim$ 10), it was numerically [25] and experimentally [30] observed that bubbles pairs achieve higher rise velocities than single bubbles, although a clear explanation is not present at the moment. Simulations showed similar fluid velocities through the gap of a bubble pair rising around Re $\sim$ 1 than a pair rising around Re $\sim$ 13, which is a surprising result that could be investigated

further. Moreover, the pressure field evolution around the bubbles was also shown to be fundamentally different compared to bubble rise above Reynolds numbers of 10. Whereas the former indicates a low-pressure zone at the aft side of the bubbles, the latter shows low-pressure zones at the inner or outer sides of both bubbles. Establishing whether the above-mentioned phenomena are a consequence or a cause of the increased rise velocity of a bubble pair at low Re compared to single bubble rise could be an intriguing starting point for future research.

Appendix A

Scoping Literature Study: General Bubble Behaviour and Numerical Methods

This initial literature study aims to create an overview of what phases a bubble goes through during its lifetime. The different mechanisms that determine how bubbles are generated, coalesce and break up are investigated. Introducing contaminants or surfactants into perfectly clean water influences bubbles greatly, affecting the three stages a bubble potentially experiences. Subsequently, several numerical methods used to simulate bubble behaviour are elaborated, constructing a basic understanding of the techniques. It should be noted that mainly scoping is carried out in this first chapter. The following chapters all focus on the rising behaviour of bubbles, being the main subject of this thesis.

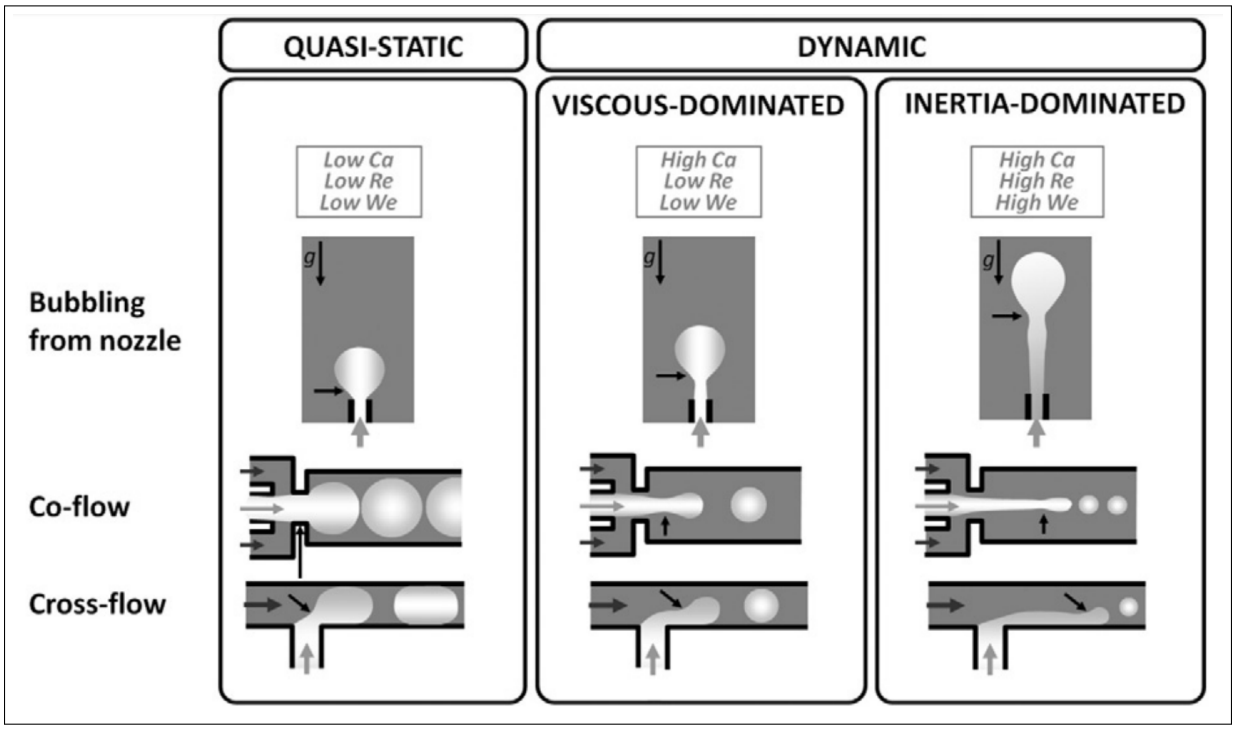

FIGURE A.1: Different bubbling regimes for a variety of the magnitude of dimensionless numbers. The black arrow indicates the break-up location. Obtained from Drenckhan & Saint-Jalmes [101].

A.1 Introduction

While the occurrence of bubbles might seem to be a trivial phenomenon, they are applied in a multitude of systems, fulfilling an essential role in a variety of fields within science and technology. Yet, the behaviour of bubbles during generation, coalescence (the coming together of two bubbles to form a single, larger bubble) and break-up remain incredibly complex problems, even to this day. Therefore, a literature study is performed to obtain a better understanding of the underlying mechanisms and the current consensus on bubble behaviour. Furthermore, the numerical techniques that are utilised to model bubble behaviour will be discussed as well.

A.2 Bubble Generation

In an air-liquid dispersion, air particles are distributed within a liquid environment. In the case of air bubbles, this liquid environment is often water. These bubbles can be introduced into the liquid in a variety of ways, where one can think of physical (mechanical action or phase transitions), chemical, or biological means [101, 102]. In the current literature research, attention will be paid to the mechanical generation of bubbles, that is, by blowing air through a nozzle, an orifice, or a porous medium, also called sparging. To generate the bubble, a topological change of the gas/liquid interface is required, i.e., the gas/liquid interface has to be deformed into a physically unstable filament that breaks, creating the bubble [101]. Detaching a bubble from a gas pocket can be done in multiple ways. For the small length scales involved in bubble generation through an orifice, gravity is not efficient. Therefore, a cross-flow or co-flow of the liquid is often utilised to ensure the detachment of the bubble by employing the viscous or inertial stresses [101].

The regimes depicted in Figure A.1 will be explained in detail in the subsequent sections. These regions will be discussed for the case of bubbling into a stationary liquid, as well as bubbling into a flowing liquid and a shear flow.

A.2.1 Bubbling into a Stationary Liquid

The subject of bubbling through orifices into a liquid has already been investigated intensively. The coming section on bubble generation is mainly based on the findings from Drenckhan & Saint-Jalmes [101], who studied foam generation. While slow bubbling (the quasi-static regime) can be described in a relatively simple way, dynamic bubbling has proven to be a sophisticated process. The system's complexity originates from the presence of multiple feedback mechanisms, the most notable of which is the coupling between the dynamic forces and bubble shape [101].

The Quasi-static Regime

In the quasi-static regime (the left column of Figure A.1), it is assumed that bubbling occurs sufficiently slow, such that both the Capillary number (Ca) and the Weber number (We) are much smaller than one. These dimensionless numbers are given by [101]:

$$\mathrm{Ca} = \frac{\mu_\mathrm{L} u}{\sigma}, \tag{A.1}$$

and

$$\mathrm{We} = \frac{\rho_\mathrm{L} u^2 L}{\sigma}, \tag{A.2}$$

where μ_L is the liquid viscosity, u the flow velocity, σ the surface tension, ρ_L the liquid density and L the characteristic length (often the diameter for bubbles). The Capillary number can be seen as the ratio between viscous stress and interfacial stress [101]. At relatively large Capillary numbers, viscous forces dominate, causing the effect of the interfacial tension to be reduced [103], with the opposite being true for low Capillary numbers. The Weber number, on the other hand, defines the ratio between inertial stress and interfacial stress. The Weber number indicates whether the inertial or surface tension forces are dominant, which can be used to describe whether a droplet is deformable. Low Weber numbers indicate that the surface tension dominates over the inertial forces, preventing a high degree of deformation and thus causing bubbles to be nondeformable [104]. The assumption of both Ca and We being much smaller than one leads the surface tension and gravitational forces (buoyancy) being dominant over the viscous and inertial stresses. Additionally, a constant gas flow rate (Q_G) will be assumed to bubble into a stationary solution using an orifice [101].

During the creation of a bubble in the quasi-static regime, the pressure goes through five well-defined states. Initially, it increases (nucleation) until a maximum is reached (under-critical growth). Once the bubble radius (R_b) is equal to that of the orifice (R_o), the bubble has become a hemisphere [101]. The maximum pressure is achieved at this point, given by [105]:

$$\Delta P_{max} = \frac{2\sigma}{R_\mathrm{o}}, \tag{A.3}$$

which has to be overcome for any bubbling application to generate bubbles. If the maximum pressure is applied, the bubble grows past the hemispherical shape (critical growth), leading to a pressure decrease. Subsequently, necking will occur, causing the bubble to detach if the surface tension force (keeping the bubble attached to the orifice) is of the same order as the buoyancy force [101].

The shape and size of the detached bubble depend on the orifice size R_o and the capillary length l_c, which is given by:

$$l_c = \sqrt{\frac{\sigma}{\Delta\rho g}}, \tag{A.4}$$

in which $\Delta\rho$ is the density difference between the two fluids and g the gravitational acceleration [101]. The capillary length is a characteristic length beyond which gravitational effects need to be taken into account in comparison to surface tension effects [101]. If the orifice size is much smaller than the capillary length, gravitational effects can be neglected, such that the shape of the detaching bubble can be approximated by a sphere of volume $4/3\pi R_b^3$ [101, 106]. The influence of the gravitational effects in a system can be described by the Bond number (Bo), which is defined as:

$$\text{Bo} = \frac{\Delta\rho g L^2}{\sigma}. \tag{A.5}$$

The Bond number can be described as the ratio between gravitational and interfacial stresses [101]. Equation (A.5) shows that a Bond number much greater than one indicates that gravitational forces dominate the system, whereas a Bond number much smaller than one suggests that the interfacial forces are in control.

As a consequence of neglecting the gravitational effects, the resulting bubble size can be determined by setting the buoyancy force F_G, which describes the influence of a hydrostatic pressure difference, equal to the surface tension force F_σ, which represents the surface tension acting over the bubble circumference [101]:

$$\begin{aligned} &F_G = F_\sigma \\ &\rightarrow \frac{4}{3}\pi\Delta\rho g R_b^3 = 2\pi\sigma R_o \\ &\rightarrow \frac{4}{3}\Delta\rho g R_b^3 = 2\sigma R_o \\ &\rightarrow R_b \sim \left(\frac{\sigma}{\Delta\rho g}\right)^{\frac{1}{3}} R_o^{\frac{1}{3}} = l_c^{\frac{2}{3}} R_o^{\frac{1}{3}} = Bo^{-\frac{1}{3}} R_o. \\ &\text{(For } R_o \ll l_c\text{)} \end{aligned} \tag{A.6}$$

Here, the length scale of the Bond number has been set to the radius of the orifice R_o. From Equation (A.6), it can be seen that the Bond number must be at least of order unity for the bubble to detach from the orifice [101].

If the orifice radius is of the order of the capillary length, i.e., $R_o \geq l_c$, the gravitational effects cannot be neglected [101]. Bari & Robinson [107] determined that Equation (A.6) can be slightly altered by modifying the exponent:

$$R_b \sim R_o \text{Bo}^{-\frac{\alpha}{3}}. \qquad \text{(For } R_o \geq l_c\text{)} \tag{A.7}$$

in which $\alpha \approx 1.06$.

The Dynamic Regime

When moving away from quasi-static conditions, various dynamic effects have to be accounted for, as can be seen in Figure A.2. Bubble detachment is, for instance, slowed down by the viscous drag of the liquid, leading to increased bubble size. While bubble size is increased as well by the inertial effects of the liquid, the inertial effects of the gas push the bubble away from the orifice, creating the opposite effect [101].

For a sufficiently low gas flow rate, i.e., $\text{We}_G < 1$, the surface tension and inertial forces of the gas can be neglected [101]. Therefore, at low flow rates, the buoyancy force only has to

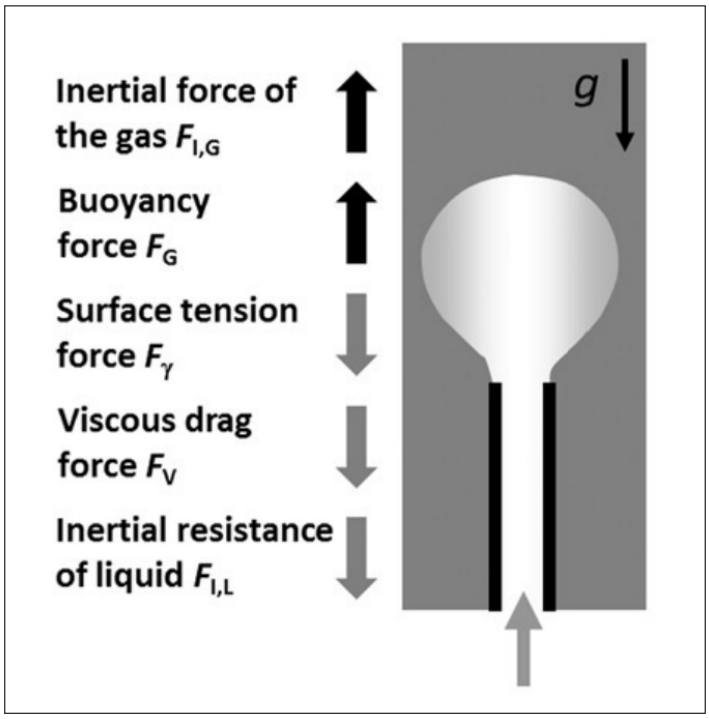

FIGURE A.2: Overview of the different forces working with and against dynamic bubble formation in a quiescent fluid at sufficiently high gas flow rates. Obtained from Drenckhan & Saint-Jalmes [101].

overcome the viscous drag force and liquid inertia since some of the liquid accelerates as the bubble accelerates upward [108]. The above leads to the following relation, corresponding to the middle column of Figure A.1 [101]:

$$R_b \sim \left(\frac{\mu_L Q_G}{\Delta\rho g}\right)^{\frac{1}{4}} \sim R_o \left(\frac{Ca}{Bo}\right)^{\frac{1}{4}}. \tag{A.8}$$

Drenckhan & Saint-Jalmes [101] describe that in contrast to the quasi-static regime, the bubble size now additionally depends on the viscosity of the liquid and the gas flow rate while not being dependent on the surface tension anymore. The bubble expands as Q_G or μ_L increases, as one might expect. When the gas flow rate is increased further to the point where $We_G > 1$, the inertial forces cannot be ignored. As these inertial forces gradually become more significant over the restoring surface tension forces for an increasing Weber number, the bubble that is being created starts to elongate, as can be seen in the right column of Figure A.1. Because of the increased inertial forces, the location of bubble detachment moves further away from the orifice, resulting in the formation of a gas jet that breaks up into bubbles at its tip, as shown in Figure A.1 [101].

There are currently two limit regions that can be defined: one driven by inertial forces as described above, and one driven by gravitational and viscous forces ($Bo > 1$). The latter is generally referred to as the 'dripping' regime, while the inertial-driven region is also known as the 'jetting' regime. In most cases, however, gravity and inertia act together, creating an operating region between the two extreme regimes. Both the Bond and Weber number are used in this region to predict the flow conditions for which bubble detachment occurs, as can be seen from Figure A.3 [101].

In most dynamic cases, however, gravity, surface tension, viscosity and inertia act simultaneously, yielding a more complex model. One of the most frequently used models is the one

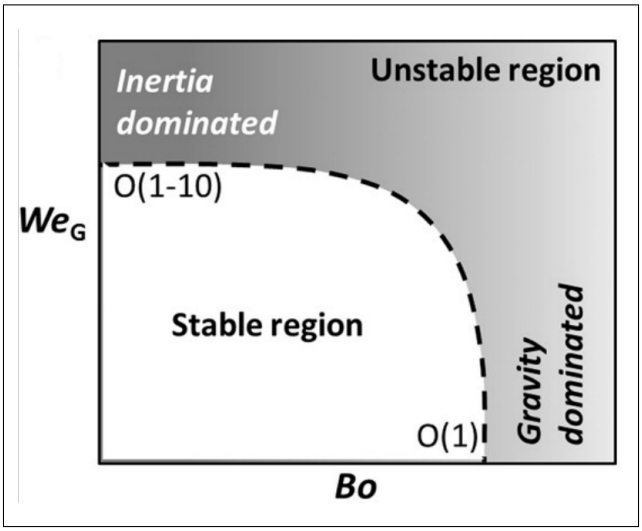

FIGURE A.3: Stability diagram of the bubbling process showing the bubbles detach if either the Bond number or the Weber number of the gas exceeds a critical value [109]. Obtained from Drenckhan & Saint-Jalmes [101].

described by Jamialahmadi et al. [110] [101]:

$$R_B = R_o \left[\frac{5.0}{\mathrm{Bo}^{1.08}} + \frac{9.261\mathrm{Fr}_\mathrm{G}^{0.36}}{\mathrm{Ga}_\mathrm{G}^{0.39}} + 2.14\mathrm{Fr}_\mathrm{G}^{0.51} \right]^{\frac{1}{3}}. \tag{A.9}$$

Here, the Galilei number (Ga) describes the ratio between gravitational and viscous stress, given by [101]:

$$\mathrm{Ga} = \frac{g\rho_\mathrm{L}^2 L^3}{\mu_\mathrm{L}^2}. \tag{A.10}$$

The Froude number (Fr) describes the ratio between inertial and gravitational stresses. It can be written as a function of the Weber number and the Bond number via [101]:

$$\mathrm{Fr} = \sqrt{\frac{\mathrm{We}}{\mathrm{Bo}}}. \tag{A.11}$$

A.2.2 Bubbling into a Flowing Liquid

With the addition of an actively flowing liquid, extra viscous and inertial forces have to be taken into account. Two standard techniques for the generation of bubbles into a flowing liquid are co-flow and cross-flow, as shown in Figure A.1 [101]. In industry, cross-flowing liquids are frequently used for two generally favourable effects. First, the liquid flow results in early bubble detachment due to the liquid drag force, increasing the bubble formation frequency and thus decreasing the resulting bubble size. Second, the coalescence probability (discussed in Section A.3) is reduced as bubbles are swept away from the orifice by the moving flow [101]. These effects enhance the interfacial area between the gas and the liquid and the boundary layer transport [111]. As stated by Drenckhan & Saint-Jalmes [101], it is vital to notice that the effect of the flowing liquid depends on the geometry in which the system is confined. The geometry fixes the flow field and, therefore, the dynamic forces as well. For the discussion of the quasi-static and dynamic regimes, the influence of gravity will be ignored. Due to the small dimensions ($\mathrm{Bo} \ll 1$) or the significance of the dynamic forces ($\mathrm{Ca} \gg 1/\mathrm{We} \gg 1$) in the system, the gravitational effect can be neglected.

The Quasi-static Regime

Assuming a low enough gas and liquid flow rate and therefore neglecting the dynamic forces, unconfined flow yields the same results as a bubble flowing into a stationary liquid [101], as discussed in the sections above. In a confined flow, however, the bubble might block the entire channel, leading to pinching off. The slow flow carries the bubble away, after which the periodic process restarts [101]. This regime is deemed the 'squeezing' regime [112] as it is controlled by the normal pressures acting on the interface. The final bubble volume V_B can be expressed as a function of both the constant liquid and gas flow rate (Q_L and Q_G, respectively) and the constriction volume V_C [101, 113, 114]:

$$V_B \sim V_C \frac{Q_G}{Q_L}, \tag{A.12}$$

in which the value of proportionality depends on the exact geometry used [101].

The Dynamic Regime

Similar to dynamic bubbling into a stationary liquid, multiple cases exist for dynamic bubbling into a flowing liquid. The simplest of these cases is when the viscous drag on the bubble exerted by the moving liquid overcomes the force that keeps the bubble connected to the orifice (the capillary force) [101]. By equating the viscous drag given by Stokes' drag equation $F_V = 6\pi R_b \mu_L u_L$ [72] and the capillary force, which is equal to the surface tension force as defined in Section A.2.1, one obtains [101]:

$$\begin{aligned} 6\pi R_b \mu_L u_L &= 2\pi\sigma R_o \\ \rightarrow R_b &= \frac{2\sigma R_o}{6\mu_L u_L} \sim \frac{\sigma}{\mu_L u_L} R_o = \frac{1}{Ca_L} R_o. \end{aligned} \tag{A.13}$$

From the above expression, it can be seen that the bubble size depends linearly on the orifice radius R_o and is inversely proportional to the Capillary number of the liquid (Ca_L) [101]. Increasing the gas or liquid flow rate will result in bubble detachment away from the orifice, which can be seen as a transition from the 'dripping' to the 'jetting' regime [115–117]. As described by Drenckhan & Saint-Jalmes [101], break-up in the squeezing and dripping regimes is caused by an instability that invades the entire system such that detachment always occurs at the orifice. In the jetting regime, where viscous and inertial forces cannot be neglected, the instability evolution is slowed down. Thus, the instability can be convected with the flow while a jet is created that breaks at the point where it has 'aged' enough.

Additionally, Drenckhan & Saint-Jalmes [101] define two extreme regimes for the jetting phenomenon, being either dominated by the external fluid flow or by the inertial flow of the inner fluid. The former leads to the acceleration of the inner fluid, thinning the jet away from the orifice and generating bubbles smaller than the orifice diameter. On the other hand, the latter yields a deceleration of the inner fluid by the outer fluid, causing a jet of increased thickness and, thus, bubbles of a size larger than the orifice.

Bubbling into a Shear Flow

In fluid mechanics, shear stress can be introduced into a flow by a Couette flow, which is a type of flow between two parallel plates with one plate fixed and the other moving. This type of flow can often be seen in lubrication applications, in which the outer cylinder of a concentric cylinder rotates while the inner one remains fixed, creating a Couette flow and thus a shear stress in the fluid [118], which influences bubble generation. The study from Mirsandi et al.

[111] focuses on bubble generation in a cross-flow, which is further elaborated in the following section.

Influence of Operating Conditions

A shear flow passing a bubble being generated at an orifice creates a drag force, flattening the bubble. Additionally, the drag force advances both the formation of the neck and the bubble detachment as the neck collapses. Increasing the gas flow rate results in a larger bubble surface area, which causes the deformation and displacement of the bubble to become more significant due to the liquid drag force. Altering the gas flow rate is one of the operating conditions that has an effect on the bubble formation process, the other being the shear rate [111]. The shear rate influences multiple parts of bubble formation, of which a number are discussed below.

Bubble Shape during Growth and Detachment

In Figures A.4.a & A.4.b, the velocity field plots of bubble formation into a quiescent fluid and a shear flow can be seen. As discussed in Section A.2.1, the bubble process in the quasi-static regime is governed only by the gravitational and surface tension forces, causing a symmetric bubble shape. Upon the introduction of a shear flow, however, both the flow field and bubble shape become significantly more complex, where the shear flow distorts the bubble shape during its growth. Increasing the shear rate will lead to more intense downstream bubble motion and flattening [111].

Detached Bubble Volume and Formation Time

The influence of the shear rate on both the detached bubble volume V_B and the formation time t_{det} can be seen in Figures A.5.a & A.5.b. For an increasing shear rate, the bubble volume and the formation time decrease exponentially. At the highest shear rate, both values are reduced by 88% compared to formation under quiescent conditions. Additionally, one can notice V_B and t_{det} becoming independent of the shear rate for higher shear rates. Here, the drag force created by the shear flow advances the neck formation, causing detachment due to the collapsing of the neck [111].

Influence of Fluid Properties

Besides operating conditions, fluid properties influence the bubble generation process as well. As was shown in Section A.2.1, the bubble size under quiescent conditions increases as a function of decreasing liquid density, increasing surface tension, and increasing liquid viscosity. For a shear flow, however, the effects of these fluid properties become less pronounced, especially at high shear rates [111].

A.2.3 Bubbling from multiple Orifices

The analysis of bubble generation has so far been focused on single orifices. Drenckhan & Saint-Jalmes [101] describe the dynamics for bubbling through multiple orifices (to generate an increased amount of bubbles) as well. The resulting behaviour of the orifices depends on whether the bubbles are blown from the same gas reservoir. Considering the case where two orifices are fed by a separate gas injection and the orifices are located sufficiently far away from each other, both orifices behave independently [101], following the behaviour described in the previous sections. Once the distance between the orifices is reduced below a critical spacing, hydrodynamic interactions start to occur [119, 120]. As a result, both orifices may synchronise their bubble generation in an alternating fashion [101].

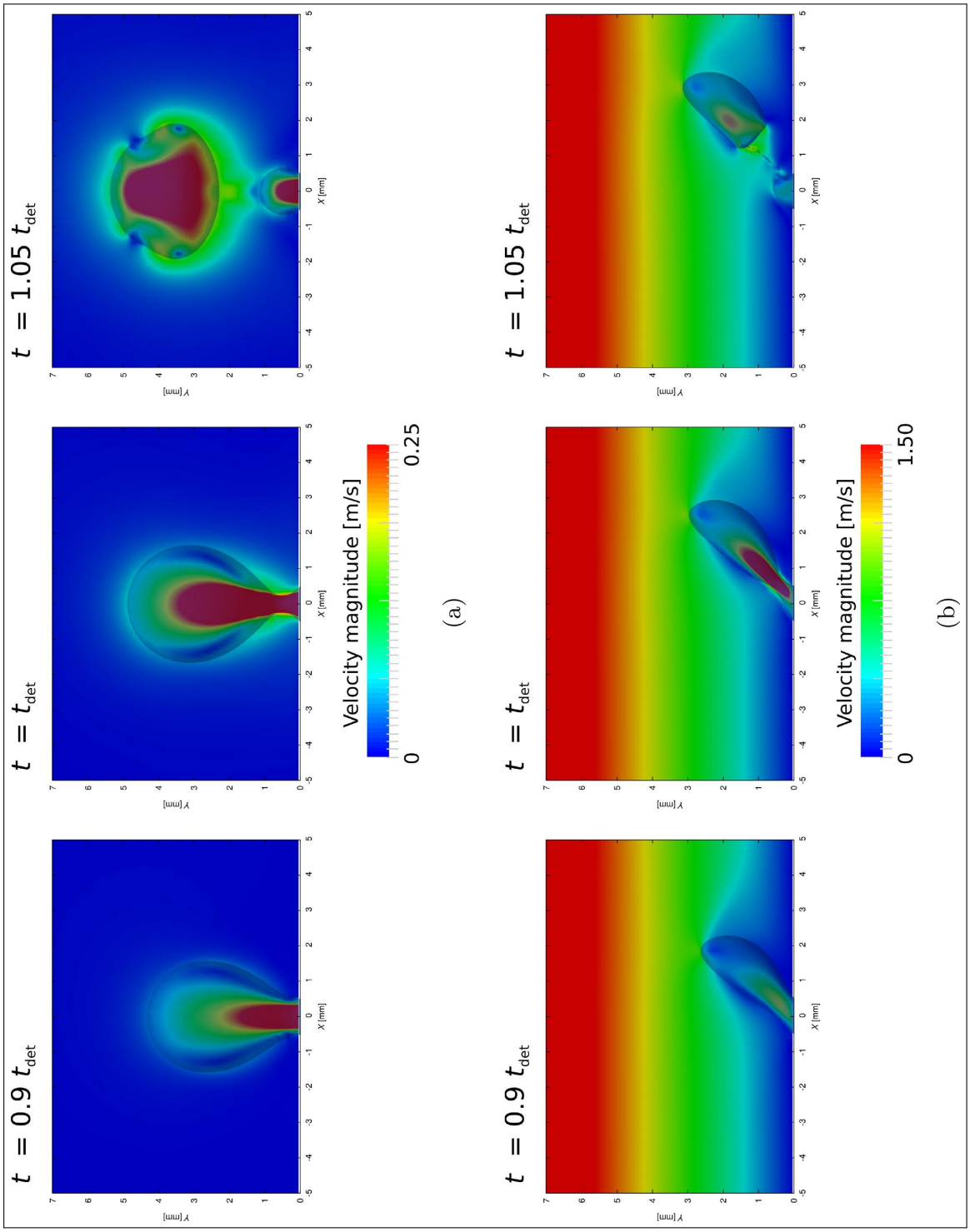

FIGURE A.4: Velocity fields in water for an air bubble growing until detachment takes place in a shear flow with a shear rate of 0 s^{-1} (a) and $2.67{\cdot}10^2$ s^{-1} (b). The formation times t_{det} are $1.32 \cdot 10^{-1}$ s and $2.53 \cdot 10^{-2}$ s for (a) and (b), respectively. Obtained from Mirsandi et al. [111].

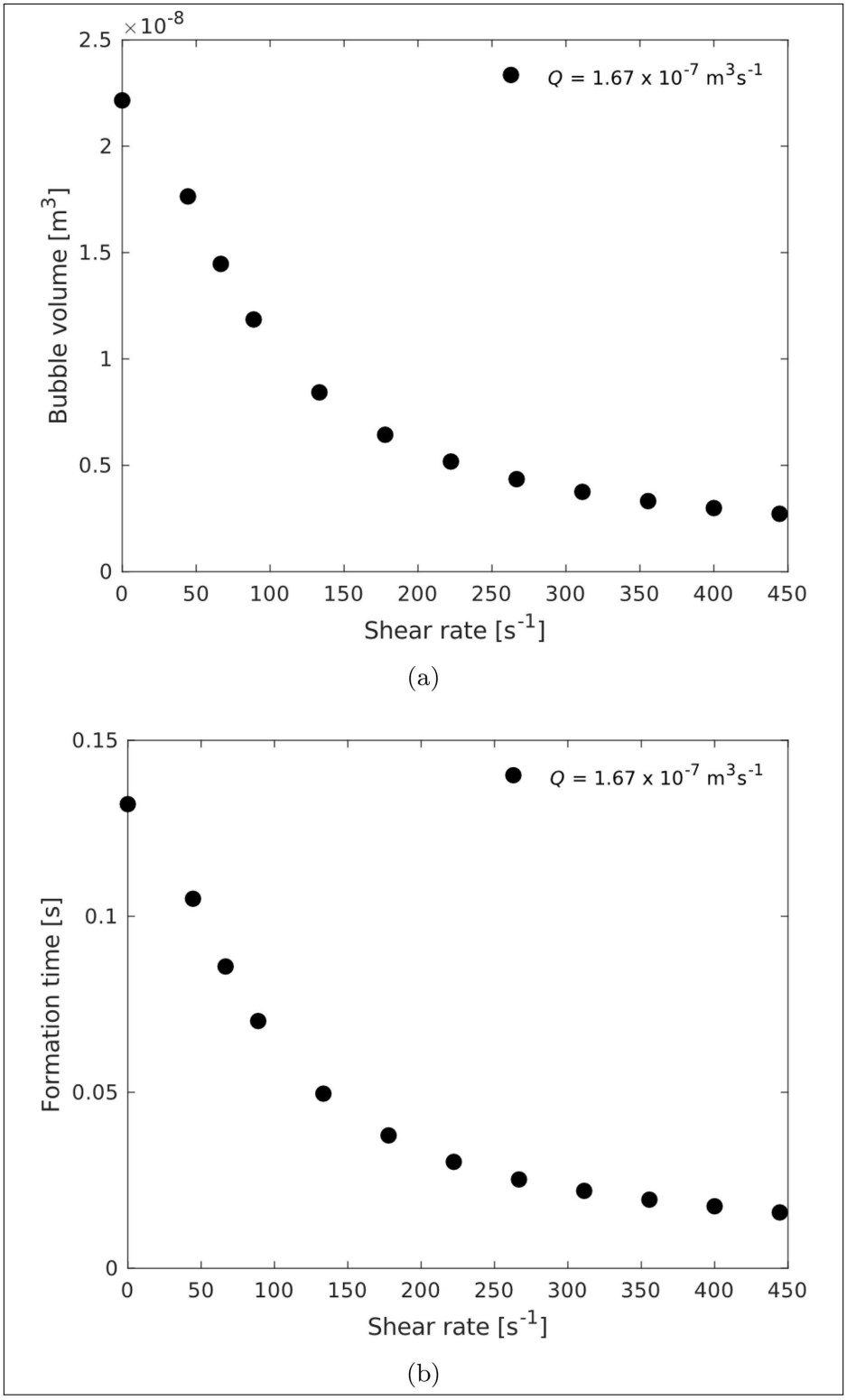

FIGURE A.5: Influence of the shear rate on the detached bubble volume (a) and the formation time (b) for an orifice radius R_o of 0.5 mm. Obtained from Mirsandi et al. [111].

Feeding the orifices from the same reservoir, as is the case with a perforated plate, leads to coupling between the orifices through pressure fluctuations as explained by Drenckhan & Saint-Jalmes [101]. Starting from a configuration in which the orifices are initially closed, an increase in pressure within the reservoir leads to the gas-liquid interface at the orifices to curve outward until the maximum pressure is reached. After this point, the bubble grows quickly, leading to a pressure drop in the underlying reservoir. This pressure drop can cause the formation of other bubbles to stagnate as they will not be able to reach the maximum pressure, such that only a limited number of holes participate in bubble formation for low flow rates. In general, bubbles will initially be created at larger holes. As the flow rate increases, an increasing amount of holes will be involved in the bubbling process due to two reasons. An increasing flow velocity causes an increased dynamic pressure drop at each hole [121]. Once the dynamic pressure reaches the capillary pressure, all holes can generate bubbles. Second, for sufficiently high flow rates, inertial forces are the dominant effect in bubble formation, leading to the formation of a gas jet. Thus, the holes remain permanently open, causing the maximum capillary pressure to become meaningless once bubbles are being formed at the hole [101].

To prevent the pressure-coupling in a system with multiple orifices, the flow resistance may be increased in the reservoir, which can be achieved by employing long slender orifices (increasing flow resistance) or by using a porous medium instead of the reservoir [101, 121].

A.3 Bubble Coalescence

Once a bubble has detached after bubble generation, the bubble has a primitive size in the system [122]. While moving with the flow of the continuous phase or rising purely by buoyancy, the final bubble size is determined by the balance between break-up (discussed in Section A.4) and coalescence [123]. Coalescence is the act of two bubbles merging into one larger bubble, which has proven to be a highly complex phenomenon to model. The rate of coalescence, also called the coalescence frequency, depends on two phenomena; the collision frequency and the coalescence efficiency [124]. In other words, the coalescence frequency is dependent upon how often collisions occur (collision frequency), as well as which fraction of these collisions lead to coalescence (coalescence efficiency) [125]. Combining the coalescence efficiency (λ) and the collision frequency (h) yields the coalescence frequency (Γ) according to the following formula as a function of the diameter of the two bubbles (D_1 and D_2) [126]:

$$\Gamma(D_1, D_2) = h(D_1, D_2)\lambda(D_1, D_2). \tag{A.14}$$

In the following sections, the most frequently used models for the collision frequency and coalescence efficiency will be elaborated.

A.3.1 Collision Frequency

A variety of mechanisms exist in turbulent bubbly flows that cause collisions between bubbles [126]. Turbulent bubbly flows are a type of two-phase flow in which tiny bubbles (such as air) are dispersed as discrete substances in a continuous liquid (such as water) [127]. Two collision mechanisms will be studied in-depth, turbulent random motion-induced collisions and velocity gradient-induced collisions.

Turbulent Random Motion-induced Collisions

One of the most commonly reported mechanisms is the collision of bubbles caused by the fluctuating turbulent velocity of the surrounding liquid [126]. Based on the assumption that particle collisions are equivalent to the random movement of gas molecules in an ideal gas

[128], the collision frequency can be expressed as a function of the bubble size and relative velocity:

$$h(D_1, D_2) = S_{12} u_{rel}, \tag{A.15}$$

in which u_{rel} is the relative velocity between the bubbles and S_{12} is equal to the collision cross-sectional area of the two bubbles, given by [126]:

$$S_{12} = \frac{\pi}{4} (D_1 + D_2)^2. \tag{A.16}$$

It is essential to notice that relative motion between bubbles (and thus collisions) due to turbulent random motion created by eddy motion is heavily influenced by the size of the eddy. While small eddies will not have sufficient energy to affect bubble motion, large eddies will transport entire bubble groups without leading to relative motion between the two bubbles [129]. The above leads to the assumption that the approach velocity of the bubbles is often taken as the velocity of an equal-sized eddy, which is shown by:

$$u_{rel} = \left(u_{t1}^2 + u_{t2}^2\right)^{\frac{1}{2}}, \tag{A.17}$$

where it can be seen that the relative velocity between two bubbles depends on the eddy velocity u_t of sizes D_1 and D_2 for bubbles of those respective sizes [126].

To determine the eddy velocity, two essential assumptions are required, the first being that the turbulence is isotropic [129]. Isotropic turbulence is a state where the turbulent fluctuations are uniform in all directions. One can think of a turbulent flow far away from boundaries, such that the problem becomes manageable [129, 130]. Even for non-isotropic applications, the isotropic turbulence assumption may be used. Experimental evidence from Hinze [131] has shown that the fine-scale structure of most non-isotropic turbulent flows is locally nearly isotropic, indicating that the fine-scale structure determines phenomena in actual turbulence [124]. To further simplify the problem, it has to be assumed that the bubble size lies in the inertial subrange of isotropic turbulence [129]. This assumption means that the bubbles are much larger than the micro scale of turbulence while being much smaller than the diameter of the equipment, which is usually satisfied [124]. By making use of the two above assumptions, the turbulent eddy velocity (u_t) can be stated as [125, 132]:

$$u_t^2 = 2.0 \epsilon^{\frac{2}{3}} D_b^{\frac{2}{3}}, \tag{A.18}$$

where ϵ is the turbulent eddy dissipation rate and D_b the bubble diameter. Filling in the expression for the collision-sectional area and the relative velocity into Equation (A.15) gives:

$$\begin{aligned} h(D_1, D_2) &= \sqrt{2.0} \frac{\pi}{4} (D_1 + D_2)^2 \left(D_1^{\frac{2}{3}} + D_2^{\frac{2}{3}}\right)^{\frac{1}{2}} \epsilon^{\frac{1}{3}} \\ &\approx 1.11 (D_1 + D_2)^2 \left(D_1^{\frac{2}{3}} + D_2^{\frac{2}{3}}\right)^{\frac{1}{2}} \epsilon^{\frac{1}{3}}, \end{aligned} \tag{A.19}$$

which is the most used calculation for the collision frequency [126], with sometimes changing pre-factors.

Velocity Gradient-induced Collisions

As described earlier, the collisions due to turbulent random motion are examined most frequently, which means that the effects of other mechanisms are usually neglected without further validation [126]. Shear flows create a velocity gradient in which collisions can occur due

to the relative motion of the particles [133]. By assuming straight streamlines and rectilinear particle motion, Friedlander [133] derived an equation for the collision frequency due to shear in laminar flow [126]:

$$h(R_1, R_2) = \frac{4}{3} (R_1 + R_2)^3 \dot{\gamma}, \tag{A.20}$$

in which $\dot{\gamma}$ indicates the shear rate and R_1 & R_2 the radius of bubbles 1 and 2.

A.3.2 Coalescence Efficiency

The coalescence frequency of bubbles and their collision frequency can be coupled by the coalescence efficiency, which describes what fraction of collisions lead to coalescence. The most popular model is the film drainage model developed by Shinnar & Church [134]. In addition, the energy model and critical approach velocity model will be discussed as well.

Film Drainage Model

The film drainage model states that two bubbles may collide, trapping a thin film of liquid between them. While the bubbles are in contact, the liquid drains from its initial film thickness (h_i) until it reaches a critical thickness (h_f). Once this critical thickness is reached, the film ruptures, leading to coalescence of the bubbles [129]. Marrucci [135] reports that the decrease in film thickness is driven by the pressure difference between the liquid in the film and the liquid outside the border of the film, which has two main contributions. The first is the capillary pressure, i.e., the pressure due to curvature differences. The pressure in the fluid (p) and the bubbles ($p + 2\sigma/r$) leads to a pressure difference of $2\sigma/r$. Capillary pressure causes drainage of the film until it is sufficiently thin ($\sim$ 1000Å). At this point, the Van der Waals forces become non-negligible, now also contributing to the pressure difference [135].

The coalescence efficiency is based on two characteristic times: the contact/interaction time (t_c) and the drainage time (t_d) [129, 136]. The contact time describes the duration for which two bubbles are in contact. If the time required to thin the film between the bubbles (drainage time) is lower than the contact time, rupture of the film will occur, leading to coalescence. The expressions for t_c and t_d vary greatly depending on the local flow conditions, such as the incidence of the colliding particles, turbulent fluctuations, and the collision force and velocity [136]. Ross [137] developed an initial model, which was later simplified by Coulaloglou [138], that tends to zero for large values of the ratio t_d/t_c and to unity for small ones, given by [126, 136]:

$$\lambda(D_1, D_2) = \exp\left(-\frac{t_d}{t_c}\right). \tag{A.21}$$

The problem that remains is the definition of these two timescales. They are dependent on a variety of variables, such as the collision forces, approach velocities, and surface properties of the bubbles [124].

Drainage time

As film drainage might differ based on viscous or inertial processes, multiple expressions for the film drainage time exist [139]. Lee & Hodgson [140] have defined various regimes for film drainage in an air-liquid system, depending on the mobility of the contact interfaces and the flexibility of the bubble surfaces [126], as will be discussed below.

Non-deformable Rigid Spheres

Bubbles can be considered to be non-deformable if they are small ($D_b < 1.0$ mm). According to Chesters [136], the drainage time can be derived by using the Poiseuille relation, which is

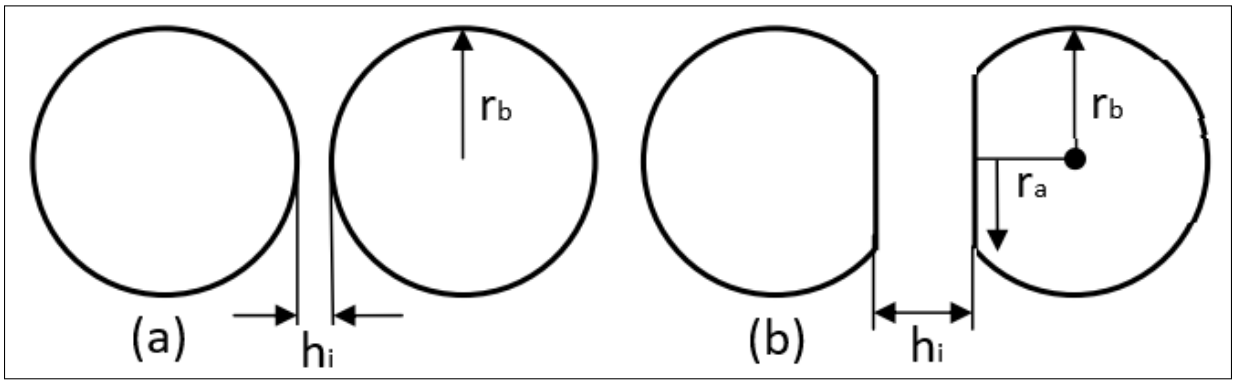

FIGURE A.6: Two bubbles with non-deformable surfaces (a) and deformable surfaces (b), in which r_a is the film radius and h_i the initial film thickness. Obtained from Simon [142].

extended by taking into account the case of unequal sized bubbles [126, 141]:

$$t_d = \frac{6\pi\mu_L}{F_i}\left(\frac{R_1R_2}{R_1+R_2}\right)^2 \ln\left(\frac{h_i}{h_f}\right), \tag{A.22}$$

where F_i is the interaction force exerted by one particle on another (further elaborated below) [126, 136].

In most situations, however, Equation (A.22) will not be reasonable as it only holds for small bubbles [126]. With the addition of larger bubbles into the system, one has to consider the deformation of the bubble surface during the collision [142]. The film drainage model for deformable interfaces that is used most frequently is a so-called parallel model in which the surfaces of the coalescing bubbles are assumed to be two parallel discs, as can be seen in Figure A.6 [126].

Deformable Bubbles, Immobile Interfaces

In the case of deformable bubbles, the mobility of the interfaces determines the formulation of the drainage time. For immobile interfaces, film drainage is controlled by viscous thinning, resulting in a laminar flow being expelled from between the two rigid surfaces [126]. Chesters [136] derived the drainage time based on the work of Mackay & Mason [143], which leads to the following expression when taking into account unequal bubble sizes [126]:

$$t_d = \frac{3\mu_L F_i}{16\pi\sigma^2}\left(\frac{D_1D_2}{D_1+D_2}\right)^2\left(\frac{1}{h_f^2}-\frac{1}{h_i^2}\right). \tag{A.23}$$

In contrast to the case of non-deformable rigid spheres, the surface tension now also directly plays a role in determining the drainage time. The film thinning rate, and thus the drainage time, is heavily dependent on the length of the liquid film. For an increase in surface tension, the bubbles become less susceptible to deformation, causing a shorter film length and thus a higher film thinning rate [136].

The assumption of immobile interfaces, however, is only applicable to systems with significant dispersed phase viscosities or systems containing a surfactant [136]. In these systems, surfactants (also see Section A.5) stabilise the interface between the two bubbles [142].

Deformable Bubbles, Fully Mobile Interfaces

The drainage process for fully mobile interfaces is the most complex, as it is governed by both inertial and viscous forces [126]. Drainage will no longer be controlled by the dispersed phase if

it has a low viscosity, instead, the resistance offered by the film to acceleration and deformation will control the drainage [136].

For unequal bubbles sizes in the inertia-controlled limit, as is the case with gas bubbles in turbulent flow, Luo [124] derived the following model, based on the expression developed by Chesters [136] [126]:

$$t_d = 0.5 \frac{u_{12} \rho_c D_1^2}{\left(1 + \frac{D_1}{D_2}\right)^2 \sigma}, \tag{A.24}$$

where ρ_c is the density of the continuous phase and u_{12} is equal to the bubble approach velocity between the two bubbles, given by:

$$u_{12} = \left(\bar{u}_1^2 + \bar{u}_2^2\right)^{\frac{1}{2}}, \tag{A.25}$$

in which $\bar{u}_1$ and $\bar{u}_2$ are the bubble velocities [124].

Interaction Force F_i

In the expressions for the drainage time t_d, an interaction force F_i, which is usually not constant, is often used. Due to a change of contact area during approach or oscillation of the bubble, for instance, the force might vary over time [126]. Chesters [136] derived an expression for the collision force in turbulent flows for both viscous and inertial collisions. In the viscous regime, the force between two colliding particles is typically expected to be proportional to the turbulent shear rate $\sqrt{\epsilon / \nu_L}$ [126]:

$$F_i \sim 6\pi \mu_L R_b^2 \sqrt{\epsilon / \nu_L}, \tag{A.26}$$

in which ν_L is the liquid kinematic viscosity.

As the interaction force in the inertial regime is larger than that in the viscous regime due to inertia, Chesters [136] defined the following relation for inertial collisions [126]:

$$F_i \sim \pi R_a^2 \left(\frac{2\sigma}{R_b}\right). \tag{A.27}$$

Contact Time

An initial definition for the contact time was defined by Levich [86], based on dimensional analysis [126]:

$$t_c \sim \frac{D_b^{\frac{2}{3}}}{\epsilon^{\frac{1}{3}}}. \tag{A.28}$$

The above formulation is based on the hypothesis from Levich that the interaction is proportional to the characteristic lifetime of an eddy with a size equal to the sum of the approaching particles [124]. A more fundamental expression which also holds for particles of unequal size was later derived by Luo [124], based on a parallel film model [126]:

$$t_{\text{contact}} = (1 + \xi_{12}) \left(\frac{\left(\frac{\rho_d}{\rho_c} + C_m\right) \rho_c D_1^3}{3\left(1 + \xi_{12}^2\right)\left(1 + \xi_{12}^3\right)\sigma} \right)^{\frac{1}{2}}. \tag{A.29}$$

In the above equation, ρ_d is the density of the dispersed phase, C_m the added mass coefficient (usually between 0.5 and 0.8), and ξ_{12} is equal to R_1 / R_2. The added mass coefficient is required as not all initial kinetic energy is transformed to increase the surface energy for unequal-sized particles [124].

Additionally, Kamp & Chesters [144] defined a different expression for unequal bubble sizes. Their definition is given as the interval between the onset of film formation and the moment at which the bubbles begin to bounce back. Assuming a balance between the increasing surface energy and the reducing kinetic energy, the contact time is defined as [126]:

$$t_{\text{contact}} = \frac{\pi}{4}\left(\frac{\rho_c C_m D_{eq}^3}{3\sigma}\right)^{1/2}, \tag{A.30}$$

where D_{eq} is given by $\frac{2D_1D_2}{D_1+D_2}$.

Initial and Critical Film Thickness

As described by Kim & Lee [145], estimating values for both h_i and h_f is a challenging task. While Kirkpatrick & Lockett [146] used an initial film thickness of 10^{-4} m, Marrucci [135] determined it to be 10^{-5} m [145]. For the film rupture thickness h_f, Mackay & Mason reported that the minimum thickness at which a film ruptures is typically less than 500 Å. Vrij [147] described the theoretical and experimental thicknesses of water films to be 410 Å and 270 Å, respectively. Furthermore, Kirkpatrick & Lockett [146] assumed a value of 250 Å, based on previous work [135]. Although the reported values differ, the consensus in literature is that h_i should be of the order $10^{-4} - 10^{-5}$ m, while h_f is of the order 10^{-8} m.

Energy Model

The energy model was proposed by Howarth [148], confirmed by Park & Blair [149] and Kuboi et al. [150] and developed by Sovova [151] [126]. Howarth's model is based on the fact that for coalescence to occur, the relative velocity along the line of centres has to exceed a critical value at the instant of collision [148]. Sovova related a drop's surface tension energy E_σ to its kinetic collision energy E_{kin} [126]:

$$\lambda(D_1, D_2) = \exp\left(-\frac{C_1 E_\sigma}{E_{kin}}\right), \tag{A.31}$$

in which the interfacial energy of the drops is proportional to the interfacial tension and the surface area of the drop [126]:

$$E_\sigma = \sigma\left(V_1^{\frac{2}{3}} + V_2^{\frac{2}{3}}\right). \tag{A.32}$$

The kinetic collision energy is taken to be proportional to the average volume $\overline{V}$ and the relative velocity of two colliding drops u_{rel} (Eq. (A.17)) [126]:

$$E_{kin} = \frac{1}{2}\rho_d \overline{V} u_{rel}^2, \text{ in which } \overline{V} = \frac{V_1 V_2}{V_1 + V_2}. \tag{A.33}$$

Substituting the expression for E_σ and E_{kin} into Equation (A.31) leads to:

$$\lambda\left(D_1, D_2\right) = \exp\left(-C_2 \frac{\sigma\left(V_1^{2/3} + V_2^{2/3}\right)\left(V_1 + V_2\right)}{\rho_d \varepsilon^{2/3} V_1 V_2 \left(V_1^{2/9} + V_2^{2/9}\right)}\right). \tag{A.34}$$

Critical Approach Velocity Model

In contrast to the energy model that states that coalescence occurs once the approach velocity exceeds a critical value at collision, Doubliez [152] and Duineveld [153] showed that coalescence favours gentle collisions. Lehr et al. [154] and Lehr & Mewes [155] defined a relationship

for the coalescence efficiency as a function of the approach velocity [126]:

$$\lambda(D_1, D_2) = \max\left(\frac{u_{crit}}{u_{rel}}, 1\right), \tag{A.35}$$

in which u_{crit} has to be determined experimentally. For the case of distilled water and air, Lehr et al. [154] found it to be equal to 0.08 m/s and independent of the bubble size.

Liao & Lucas [126], however, criticized the above equation as the coalescence efficiency $\lambda(D_1, D_2)$ approaches a value of infinity when the relative velocity approaches zero. Therefore, they proposed the following corrected formulation:

$$\lambda(D_1, D_2) = \min\left(\frac{u_{crit}}{u_{rel}}, 1\right). \tag{A.36}$$

A.4 Bubble Break-up

In contrast to the coalescence process, break-up reduces the size of bubbles, controlling the maximum stable bubble size [156]. According to Hinze [157], hydrodynamic stresses cause bubble break-up, while surface tension counteracts the deformation caused by these stresses. Multiple mechanisms can cause break-up, among which break-up due to turbulent fluctuations and break-up due to viscous shear forces. Which break-up mechanism transpires depends on the regime in which the break-up occurs, i.e., in turbulent flow, laminar flow, or stagnant liquids [156].

A.4.1 Turbulent Flow: Turbulent Fluctuation and Collisions

In turbulent flows, break-up is mainly caused by turbulent pressure fluctuations along the surface. Due to collisions with eddies or variations of the surrounding fluid, the bubble will alter its spherical form [158]. Once the amplitude of the oscillation reaches the point to make the particle unstable, it deforms and stretches, leading to a neck that splits into two or more so-called daughter particles [158].

Liao & Lucas [158] describe that the break-up mechanism in turbulent flows is governed by the balance between the dynamic pressure difference around the particle (τ_i) and the stress due to surface tension (τ_s). Whether or not the bubble breaks depends on the ratio of τ_i/τ_s, i.e., the amount of deformation. In literature, at least five cases are distinguished as break-up criterion [158], which will be elaborated on below. In these cases, the mentioned critical values are the surface energy of the bubble before break-up, the increase in surface energy from before to after break-up, or the mean value of the surface energy increase upon break-up resulting in daughter particles [123].

Turbulent Kinetic Energy Greater than a Critical Value

Coulaloglou & Tavlarides [159] derived a break-up model by considering drop deformation under the influence of local pressure field fluctuations and the time required for a critically deformed drop to break up. An oscillating, deformed drop breaks once the kinetic energy transmitted from an eddy collision exceeds its surface energy. The break-up frequency or efficiency Ω as a function of the volume of the parent bubble V_i is given by [159]:

$$\Omega(V_i) = \left(\frac{1}{\text{breakage time}}\right)\left(\frac{\text{fraction of}}{\text{drops breaking}}\right), \tag{A.37}$$

in which the fraction of drops breaking is assumed to be proportional to the fraction of turbulent eddies colliding with the droplet with a turbulent kinetic energy larger than its surface energy. This fraction can be derived by considering the relative velocity and approach direction at collision [159]. Based on Batchelor's isotropic turbulence theory, the break-up time (t_b) is estimated with the assumption that the motion of the daughter droplets is similar to the relative motion of turbulent eddies, and can be written as [158–160]:

$$t_b \sim C_3 D_b^{\frac{2}{3}} \epsilon^{-\frac{1}{3}}. \tag{A.38}$$

Prince & Blanch [129] criticized Equation (A.37) as the break-up rate is a function of the dispersed phase density (included in the fraction of the drops breaking). In gas-liquid systems, however, break-up is governed by the density of the surrounding fluid, causing Equation (A.37) to give break-up rates several orders of magnitude lower than experimental observations. This disagreement led to the development of a model for the break-up rate based on the continuous phase density by Prince & Blanch [129], which is discussed below.

Turbulent Kinetic Energy of the Colliding Eddy Greater than a Critical Value

The criterion that is described most in literature is based on examining the interaction of bubbles with turbulent eddies, which mainly revolves around the theory of Hinze [157]. The theory states that bubble break-up occurs through bubble interactions with turbulent eddies. The size of the turbulent eddies is of great importance for the break-up process. Eddies larger than the bubble size will transport the bubble without causing break-up, while small eddies do not possess enough energy to initiate break-up. Only eddies equal to or slightly smaller than the bubble size hold the correct amount of energy for break-up [129].

Similar to coalescence, Prince & Blanch [129] considered the break-up efficiency to be a function of the collision frequency (w) and the collision efficiency (P_b). First, a bubble has to collide with a turbulent eddy of the right size (collision frequency), after which the turbulent eddy also requires enough energy to cause rupture (collision efficiency).

Collision Frequency

As was also done in Equation (A.15), the collision frequency of a bubble i with a turbulent eddy e is given by [129]:

$$w(D_i, D_e) = S_{ie} u_{rel}, \tag{A.39}$$

Multiplying the above expression by the number densities n_i and n_e of the bubbles and the eddies, respectively, gives the collision frequency per unit volume [125].

Collision Efficiency

The collision efficiency can be seen as the probability that a turbulent eddy has sufficient energy to cause break-up [158]. Prince & Blanch [129] describe the criterion as a relation between eddy energy and the surface tension of a bubble, which can be seen as the ratio between disruptive and cohesive forces, given by the Weber number. For a critical Weber number of 2.3 for air bubbles in water, the cohesive surface tension forces and disruptive turbulent eddy forces balance, leading to a maximum stable bubble size. This Weber number is subsequently used to derive a relation for the critical eddy velocity (u_{ci}) as a function of the bubble radius R_i:

$$u_{ci} = 1.52 \left(\frac{\sigma}{R_i} \right)^{\frac{1}{2}}. \tag{A.40}$$

What remains to be determined is the number of eddies with a velocity higher than the above value, which can be done by using an energy distribution function. An expression is given by Angelidou et al. [161] for the random distribution of energy χ:

$$\chi(E_e) = \frac{1}{\bar{E}_e} \exp\left(\frac{-E_e}{\bar{E}_e}\right), \tag{A.41}$$

where E_e is the kinetic energy of an eddy and $\bar{E}_e$ the mean kinetic energy of the eddy. The energy of the eddy is taken to be proportional to the square of the velocity, yielding the following function for the fraction of eddies with sufficient energy for bubble break-up [159]:

$$P_b = \exp\left(-\frac{u_{ci}^2}{u_{te}^2}\right), \tag{A.42}$$

where u_{te} describes the turbulent velocity of an eddy with diameter D_e as in Eq. (A.18) ($u_{te}^2 = 2.0\epsilon^{\frac{2}{3}} D_e^{\frac{2}{3}}$).

The collision frequency and collision efficiency are subsequently used to yield an expression for the break-up efficiency due to eddies from various sizes [129]:

$$\Omega(V_i) = \sum_i \sum_e S_{ie} u_{rel} \exp\left(-\frac{u_{ci}^2}{u_{te}^2}\right). \tag{A.43}$$

Liao [158] noticed that the density of the continuous phase ρ_c was not included in Equation (A.40) from Prince & Blanch [129], which can be checked by dimensional analysis. Introducing ρ_c underneath the fraction bar will lead to a dimensionally correct expression.

Luo & Svendsen [162] applied a similar approach as Prince & Blanch [129] to determine the break-up frequency [158]. The main difference comes from the definition of the critical energy E_c, now defined as surface energy increase during break-up. Luo & Svendsen [162] pointed out that their model does not require any unknown parameters as isotropic turbulence theory is used to determine all constants in the model.

Inertial Force of the Colliding Eddy Greater than the Surface Force of the Smallest Bubbles

In contrast to the models above using an energy criterion, Lehr & Mewes [155] developed a model based on a force balance between the inertial force of the arriving eddy and the interfacial force of the daughter bubble [158]. According to Wang et al. [163], the capillary pressure of a tiny droplet will be very high due to its radius of curvature tending to zero, such that an eddy with a large enough energy according to the previous models might not produce enough dynamic pressure to overcome the capillary pressure, thus not leading to break-up.

Combination of the two above Mechanisms

By combining both the force and the energy criterion, Wang et al. [163] intended to obtain a more suitable model for the break-up frequency. They argued that the force balance approach designed by Lehr et al. [154, 155] may not be satisfied during break-up as the inertial force of the colliding eddy usually exceeds the inertial force until breakage occurs [158].

Wang et al. [163] criticized the energy model of Luo & Svendsen [162] as well. In their model, Luo & Svendsen [162] define the so-called breakage volume fraction f_{BV} as the ratio between the volume of one of the daughter bubbles (V_1) to that of the parent bubble (V):

$$f_{BV} = \frac{V_1}{V} = \frac{D_1^3}{D^3} = \frac{D_1^3}{D_1^3 + D_2^3}. \tag{A.44}$$

The values for f_{BV} lie between 0 and 1, where $f_{BV} = 0.5$ indicates equal binary breakage and $f_{BV} = 0$ or 1 meaning no breakage. Luo & Svendsen [162] considered the probability for a bubble to break with break-up fraction f_{BV} when hit by eddy of size D_e to be equal to the probability of the kinetic energy of the eddy to be larger than or equal to the minimum energy required to cause break-up fraction f_{BV} for an eddy of size D_e [163]. Wang et al. [163], however, argued that break-up might also occur for break-up fractions lower than or equal to f_{BV} [158]. The resulting model of Wang et al. [163] takes into account both criteria and is based on extending the energy model of Luo & Svendsen [162] by adding the capillary constraint used by Lehr et al. [154, 155] for the force balance [158]:

$$P_b\left(D_i, D_j, D_e\right) = \int_0^\infty \frac{1}{f_{BV,\max} - f_{BV,\min}} \chi(E_e) dE_e, \tag{A.45}$$

where $f_{BV,\max}$ and $f_{BV,\min}$ are determined by the energy and force constraints, respectively. $\bar{E}_e$ (in $\chi(E_e)$, Eq. (A.41)) is given by [163]:

$$\bar{E}_e = \frac{\pi}{6} D_e^3 \rho_c \frac{u_{te}^2}{2}. \tag{A.46}$$

Velocity Fluctuation Around the Bubble Surface Greater than a Critical Value

If the density and viscosity of the dispersed phase are similar, the stochastic model developed by Narsimhan & Gupta [164] can be used. Due to a difference in velocity fluctuations near the bubble surface, oscillations and, subsequently, break-up is caused [158]. However, since the density of water is approximately 1000 times higher than that of air, the velocity fluctuation criterion will not be of significant importance for the current research.

A.4.2 Laminar Flow: Viscous Shear Forces

In laminar flow, viscous shear forces at the bubble surface elongate the bubble, causing break-up [156]. These viscous shear forces are generated by the viscosity difference along the interface of the bubble, which attempts to distort the interface against the resistance created by the surface tension [123]. Therefore, this break-up mechanism can be seen as a balance between external viscous stresses (τ_v) and surface tension forces (τ_s), which can be described by the Capillary number ($\mathrm{Ca} = \tau_v / \tau_s$). If the Capillary number exceeds a critical value, the surface tension forces are not able to withstand the hydrodynamic stresses anymore, leading to the deformation of the bubble, after which it will rupture [158]. In addition, Tucker & Moldenaers [165] derived that the break-up depends on the viscosity ratio when the Capillary number is slightly larger than the critical value. If the ratio is much smaller than one, break-up initiates from the tip of the bubble. For a ratio around unity, break-up through necking occurs. When the Capillary number is much larger than the critical value (i.e., the external viscous stresses are significantly larger than the surface tension), however, the bubble elongates rapidly into a cylindrical thread, breaking into small fragments afterwards [165].

Shearing-off Process

If the bubble size increases to approximately 5 mm, the viscous shear break-up changes to a shearing-off process [123, 158]. In this process, multiple smaller bubbles are sheared off from a large bubble, also called erosive breakage [158]. Fu & Ishii [166] observed that skirts are formed around the cap of the bubble in a highly viscous flow. Once the balance between the viscous shear force and the surface tension is not realized anymore due to the high relative velocity between gas and liquid, the bubble skirts become unstable and break into small bubbles, as shown in Figure A.7.

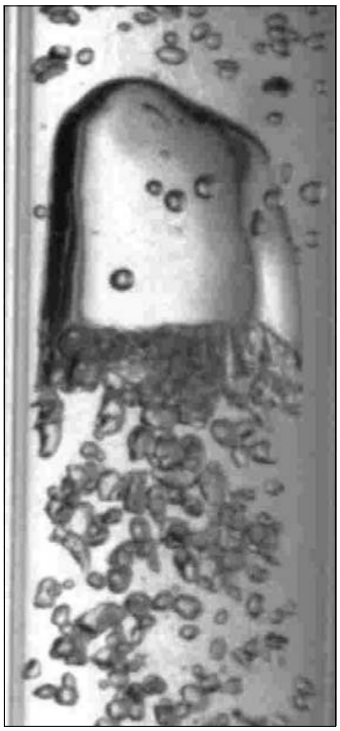

FIGURE A.7: Break-up of a large bubble due to shear-off. Obtained from Fu & Ishii [166].

In systems with low interfacial shear forces, such as an air-water flow, an alternative mechanism causes shear-off. Gases inside the bubble move at the terminal velocity, while the velocity of the gases at the boundary (near the air-water interface) approaches the liquid film velocity. Penetration from the gas in the boundary layer into the liquid film may subsequently occur, forming little bubbles [123].

A.4.3 Stagnant Flow: Interfacial Instability

In the stagnant liquid regime, break-up behaviour is determined by interfacial instabilities and wake vortices [156]. In the absence of a net flow, a large air bubble rising in a quasi-static water system may break into several smaller bubbles due to interfacial instabilities. Additionally, the presence of surfactants can cause interfacial instabilities as well. As discussed by Chu et al. [123], the gradient in surface tension caused by different surfactant concentrations leads to the Marangoni effect. This surface tension gradient leads to a convective motion of the fluid from regions of low surface tension towards high surface tension regions as high surface tension regions pull more strongly on the surrounding liquid, also called Marangoni flow [169]. Under certain conditions, the local stresses created by the Marangoni flow may enhance surface instabilities, promoting interface disintegration [123]. It is argued that a force is generated at the position where a surfactant molecule is located. A tearing action is produced as the force points away from the surfactant, yielding the formation of a bulge when multiple surfactant molecules are involved. Upon break-way, the bulge forms into a bubble [123], as shown by Figure A.8.

Although the stimulation of break-up by surfactants is discussed above, it is argued as well that surfactants act in the opposite direction to lower the effect of the bulge [123]. Miller & Neogi [167] discuss the 'calming' effect of surfactants. They suggest that the difference in response might originate from the intensity of the disturbance: minor disturbances (or deformations) lead to the effect of surfactants opposing the growth of the deformation, while surfactants make them grow in the case of major disturbances.

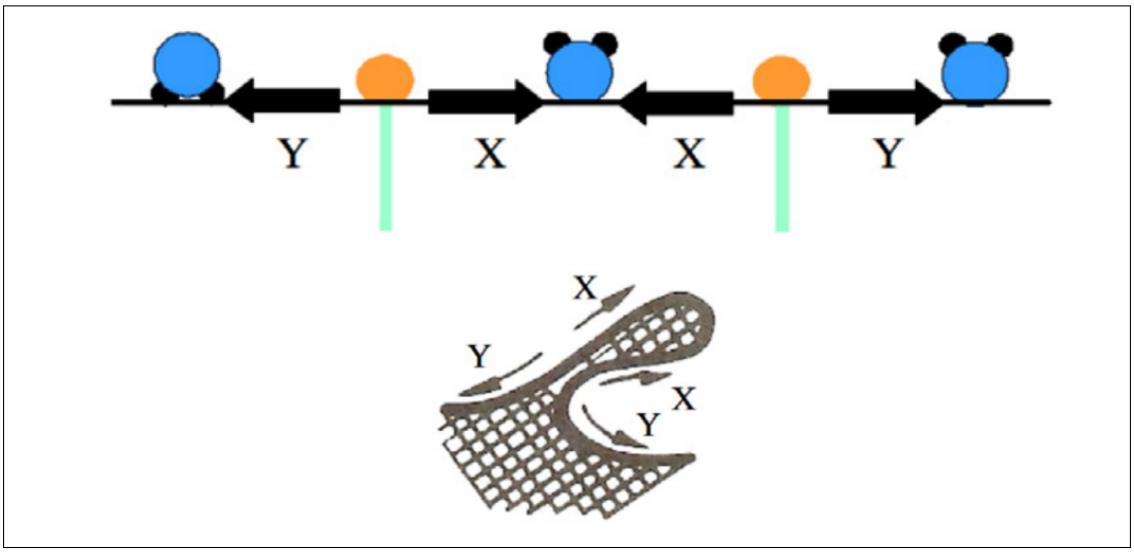

FIGURE A.8: The upper diagram displays the tearing action caused by two surfactant molecules while the lower diagram shows a liquid break-up model proposed by Miller & Neogi [167, 168]. Obtained from Chu et al. [123].

A.4.4 Coalescence-induced Break-up

After two bubbles have coalesced, break-up can occur relatively quickly due to the disruptive energy provided by the oscillation of the interface [123]. The process can be seen in Figure A.9, as proposed by Tse et al. [170]. Once the film separating the bubbles (Figure A.9.a) ruptures, a neck develops between the two bubbles (Figure A.9.b). The neck expands over time, representing the radial expansion of the bubble (Figure A.9.c, d). Additionally, small surface waves travel outwards as well, creating an unstable extension at the end of the bubble (Figure A.9.e). Under the condition that this extension is sufficiently long and thin, it ruptures and creates a daughter bubble (Figure A.9.f) [123].

Tse et al. [170] and Chu et al. [123] describe the coalescence-driven break-up mechanism to be caused by the propagation of an annular wave. The purpose of the annular wave is to dissipate the energy of the system. It may, however, also cause the formation of capillary waves on the bubble surface. Due to the decrease of surface area at the instant of coalescence, an oscillatory motion is introduced. This oscillatory motion can generate several small surface waves, which may be the cause of the breakaway of a small bubble [171].

A.5 Effect of Surfactants

As already briefly touched upon, surfactants reduce the surface tension of a liquid, caused by breaking the strong cohesive interaction between water molecules when the surfactants are absorbed [172]. Surfactants can intentionally be added to the system (e.g., as a detergent in cleaning applications), but many impurities in water can also act as surfactants [173]. The adsorption of surfactants affects multiple mechanisms of bubble behaviour.

A.5.1 Effect on Bubble Generation

Although surfactants affect bubble generation from an orifice, it should be noted that changing the surface tension does not fundamentally modify the global characteristics of the dynamics of bubble formation [174]. However, the addition of surfactants into the fluid affects multiple components of bubble generation, which are addressed below.

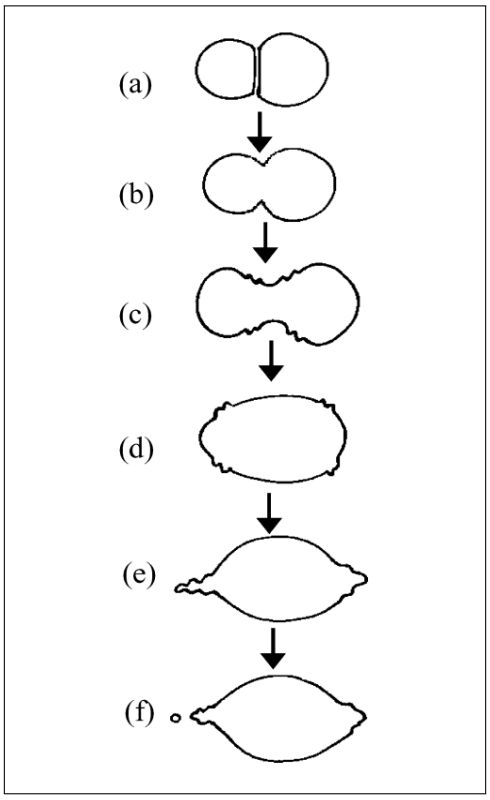

FIGURE A.9: Schematic representation of coalescence-induced break-up over several steps. Obtained from Tse et al. [170].

Effects on Bubble Diameter

For a gas velocity above a critical value (6 m/s in the research of Loubière & Hébrard [174] for a rigid orifice with a diameter of 0.7 mm), changing the surface tension does not affect the bubble diameter. Below that velocity, however, the bubble diameter in a surfactant solution (of a non-ionic, cationic or anionic surfactant) is significantly lower than is the case for water. It is hypothesized that this is caused by the fast diffusion kinetics and the low static surface tension of the used surfactants [174].

Effects on Bubble Frequency

The bubble frequency shows the combined effect of the bubble growth time and the time-out between the two bubbles. In the research of Loubière & Hébrard [174], it could be seen that the bubbling frequency in a surfactant solution is, on average, higher than in the case of pure water. Due to the lower liquid cohesion, gas is more easily introduced into the surfactant solutions, causing a lower time-out between two bubbles and thus giving rise to a higher bubbling frequency [174].

A.5.2 Effect on Coalescence

Surfactants have a significant impact on the coalescence between bubbles. Both the film drainage time and the coalescence rate after contact are affected by the presence of surfactants. The effect on these different parts of coalescence will be discussed.

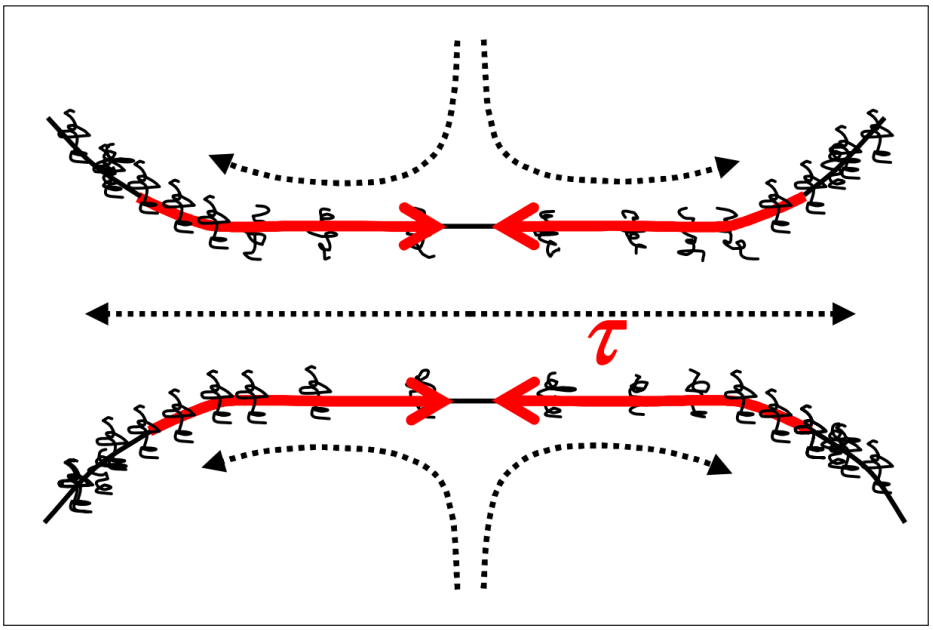

FIGURE A.10: The effect of the surfactants concentration on film drainage during coalescence, slowing down film drainage. Obtained from Dai & Leal [175].

Effect on Film Drainage Time

Surfactants can delay coalescence by slowing the drainage of the liquid film that exists between two approaching bubbles before contact is made [176]. The current consensus is that the outflow of the thin film produces a gradient in the surfactant concentration. While the lowest concentration (and thus the highest surface tension) occurs at the centre of the film, the highest takes place near the edges of the film, as can be seen in Figure A.10. The gradient that follows yields Marangoni stresses that immobilise the interfaces within the film, thus slowing down the film drainage and coalescence process [175].

Additionally, the stability of the liquid film depends upon the magnitude of the disjoining pressure, which arises from forces between the two interfaces of the liquid film [177, 178]. According to Damodaran [179], when two interfaces of the thin liquid film contain adsorbed surfactants, the generation of interaction forces between the surfactant layers causes a disjoining pressure. The creation of this pressure tends to increase the film thickness and, therefore, prevents its thinning.

Effect on Coalescence Rate after Contact

Next to altering the film drainage time, the coalescence rate is also lowered by surfactants after the bubbles have come into contact with each other. Once this contact occurs, a small bridge is formed between the bubbles, also called the meniscus bridge. Surfactants accumulate on the bridge when the bubbles have started to coalesce due to the rapid contraction of the interface [176]. This locally increased concentration of surfactants on the bubble surface leads to the Marangoni effect [180]. On the surface of the bubble, the surface tension gradient develops Marangoni stresses that pull the fluid adjacent to the interface towards the back of the bubble. At the back of the bubble, regions of high surface tension, and thus low concentrations of surfactants, are now developed. These coupled transport mechanisms retard the coalescence rate of two bubbles [176].

A.5.3 Effect on Bubble Break-up and Size

As described earlier, bubble break-up can be caused by hydrodynamic stresses that can disrupt the bubble surface if they have a sufficient size and magnitude [157]. Once surfactants are added to the fluid, the dynamic elasticity of the air-liquid interface determines whether the bubble can resist the hydrodynamic stresses [156]. In the study of Jávor et al. [181], four different surfactants were used (a weakly surface-active alcohol (1-Pentanol), a highly surface-active polyglycol (PPG425) and two polyglycol frothers[1] (DF200 & DF250)) to determine their effect on bubble break-up. It was shown that 1-Pentanol and DF200 do not have a significant impact on the bubble size distribution compared to the case of water; however, the results suggested more frequent break-ups. In solutions with PPG425 and DF250, only bubbles of small size and with the initial diameter were found, indicating coalescence prevention due to the addition of the surfactants [181].

According to Walter & Blanch [156], the maximum stable bubble size and surface tension have a direct relationship, given by:

$$D_m = 1.13 \frac{\sigma^{0.6}}{(P/V)^{0.4} \rho_L^{0.2}} \left[\frac{\mu_L}{3\mu_G} \right]^{0.1}, \tag{A.47}$$

in which P/V indicates the power per unit volume and μ_G the gas viscosity. According to the above formula, reducing the surface tension by 50% will lead to a reduction in maximum stable bubble size of 34%. They found, however, that the surfactant replenishment rate at the surface of the bubble is involved as well. As the bubble elongates at the onset of break-up, the amount of surfactant per unit area decreases. The decrease in surfactant concentration subsequently leads to an increase in surface tension unless the surfactant on the surface is replenished. The results from Walter & Blanch [156] suggested that low molecular weight surfactants ($< C_s$: surfactant concentration in bulk) replenish the surface of the bubble quickly, while long chain length surfactants ($> C_s$) replenish slowly. Due to the fast replenishment rate of the small molecular weight surfactants, the surface tension remains reduced, keeping the maximum stable bubble size low [156].

A.6 Numerical Methods

To solve multiphase flows with numerical models, it is necessary to determine the optimal approach on how to tackle the dynamics and phenomena that occur in such flows [183]. There are two main methods used in numerical simulations: the Lagrangian and Eulerian approach. Whereas the Lagrangian approach deals with individual particles and calculates their trajectories separately, the Eulerian approach deals with large concentrations of particles, calculating the overall diffusion and convection of several particles. For the same problem with multiple particles, the Eulerian method will often be less time-consuming than the Lagrangian method as it can model the average behaviour of particles instead of modelling the behaviour per separate particle [184]. As fluid mechanics often deals with large deformations, Eulerian field descriptions are frequently used. For the coupling, however, one can choose either a Lagrangian or an Eulerian representation of the interface. Lagrangian interface representations possess simple and accurate transport between the surface (interface) and the volume. For the phenomena described in this study (coalescence and break-up), however, large deformations occur, which leads to difficulties when applying the Lagrangian representation. For that reason, Eulerian interface descriptions are often used for such phenomena as they can deal with changes in topology [185]. They, however, also produce more complex transport schemes [185].

[1] A frother is a surface-active agent with the primary aim to reduce the size and the rising velocity of bubbles [182].

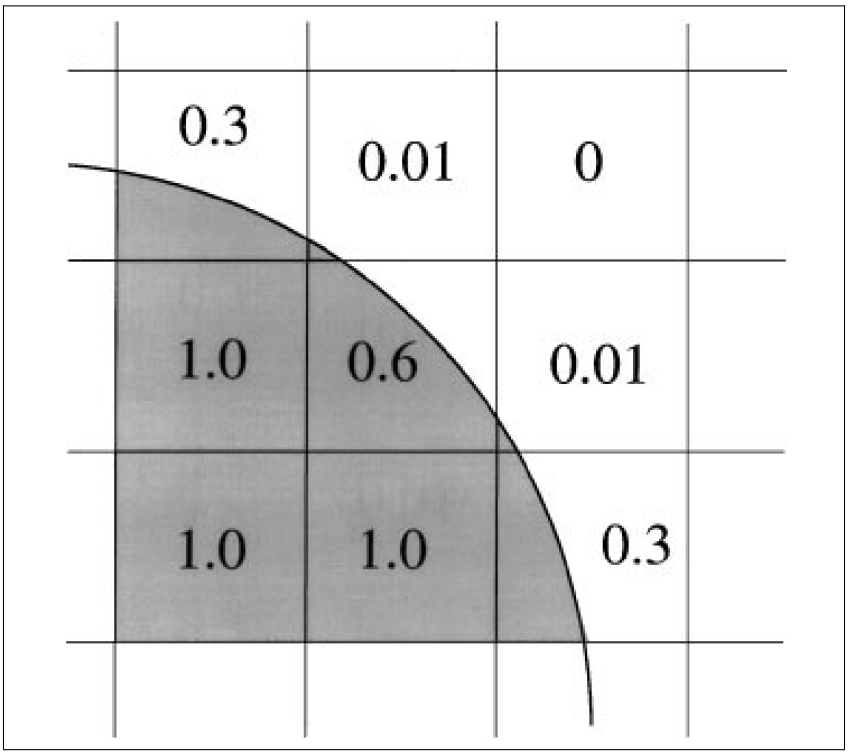

FIGURE A.11: The VOF method applied over a square grid. Values of unity indicate the full presence of a fluid, while a value of zero indicates no fluid presence. Intermediate values posses the interface. Obtained from Scardovelli & Zaleski [186].

Amongst the Eulerian interface representation, one can find the volume-of-fluid (VOF) method (Scardovelli & Zaleski [186]), the level set method (Sussman et al. [187], Sethian & Smereka [188]) and the phase-field method (Anderson et al. [189]). To deal with the more complex transport schemes, multiple new methods have been developed over the past decades. These include higher-order geometric VOF methods for sharp interface motion (Gueyffier et al. [190]), conservative level set methods (Desjardins et al. [191], Xiao et al. [192]) and coupled VOF-level set methods (Sussman & Pucket [193]) [185].

A.6.1 Volume of Fluid Method

The volume of fluid (VOF) method, created by Hirt & Nichols [194], employs a step-function $F(\mathbf{x}, t)$ whose value is unity at any point occupied by fluid and is zero otherwise. By taking the average value of F in a cell, the fractional fluid volume in that cell is represented. Any value between zero and one means the presence of fluid in the cell, implying that it contains a free surface [194], as can also be seen in Figure A.11 and its definition [195]:

$$F(\mathbf{x}, t) = \begin{cases} 1, & \text{in the liquid,} \\ 0 < F(\mathbf{x}, t) < 1, & \text{at the interface,} \\ 0, & \text{in the gas.} \end{cases} \tag{A.48}$$

Besides describing which cells contain fluid, the VOF method is also capable of describing where the fluid in a cell is located. As the value of F changes most rapidly in the direction normal to the boundary, the derivatives of the step-function can be used to determine the normal direction to the boundary [194]. Based on the combination of the value of F and the direction normal to the boundary, a line can be constructed that approximates the interface [186]. This

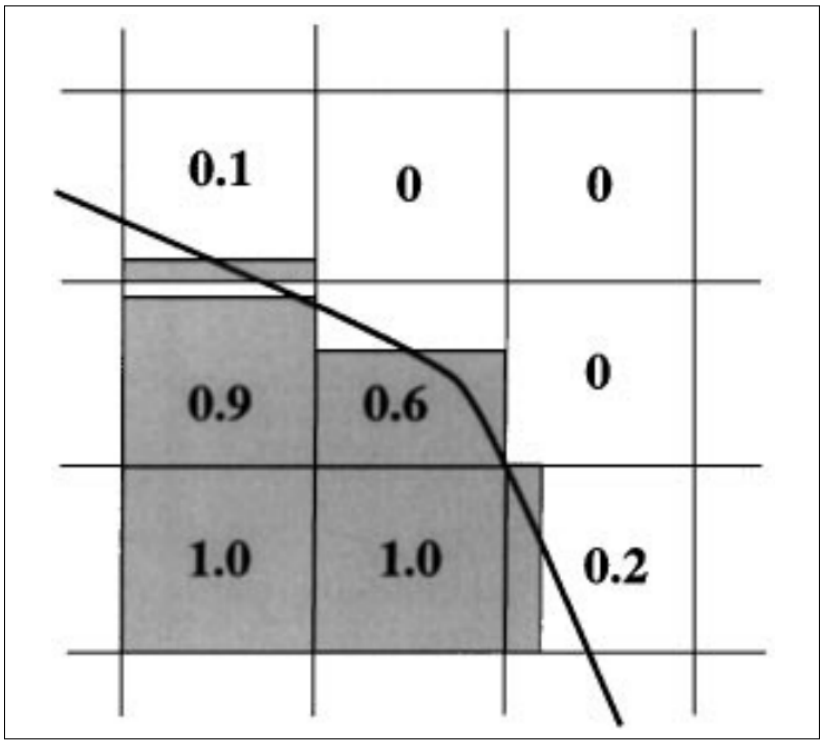

FIGURE A.12: First-order reconstruction of the interface shown in Figure A.11. Obtained from Scardovelli & Zaleski [186].

reconstruction method can achieve different orders of accuracy. The most simple methods, such as simple line interface calculation (Noh & Woodward [196]) or the SOLA-VOF algorithm (Hirt & Nichols [194]) are first-order accurate, where the line segments are straight lines and are aligned with the grid, as can be seen in Figure A.12. In the figure, it can be seen that the reconstruction is a relatively rough approximation of the real interface shown in Figure A.11, which immediately indicates its main disadvantage. The VOF method becomes cumbersome for any smooth property, such as curvature of the interface, leading to an interface of low resolution [183, 197].
To overcome the curvature problem, one may choose to use higher-order accurate reconstruction methods. Wang et al. [195] utilized a second-order accurate distance function, yielding better numerical results than the benchmark VOF method.

A.6.2 Level Set Method

As described by Vasconcelos et al. [183], the level set method (developed by Osher & Sethian [198]) treats the interface as a zero level set of a continuous function in contrast to the VOF method. The level set method has the advantage of being a smooth geometric function and thus providing increased accuracy for the calculation of smooth properties of the interface, such as the curvature. This approach, however, does have the drawback that the aforementioned advantage comes at the cost of mass conservation calculations due to its susceptibility to numerical dissipation [183]. Advection of the level set function leads to smoothening of the sharp edges, causing mass loss [195]. The level set function ϕ_{LS} is a scalar field that indicates the distance to the nearest interface or boundary, with each fluid within the grid being assigned an opposite sign of ϕ_{LS}, causing ϕ_{LS} to vary smoothly across the interface [199]. Because of this, key parameters, such as the normal vector of the interface and curvature, are easily accessible within the level set function without requiring interface reconstruction [199]. The function is

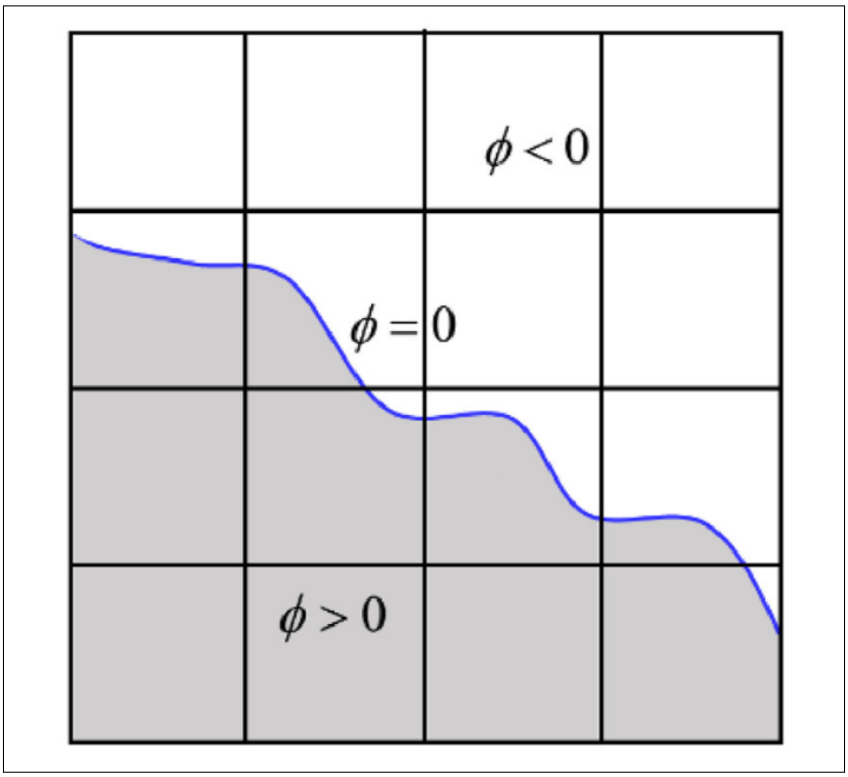

FIGURE A.13: Illustration of the level set function, where the blue line indicates the interface and the grey area the liquid phase. Obtained from Luo et al. [202].

defined as follows [200, 201]:

$$\phi_{LS} = \begin{cases} -d, & \text{for fluid 1,} \\ 0, & \text{at the interface,} \\ d, & \text{for fluid 2,} \end{cases} \tag{A.49}$$

where d indicates the shortest distance between a grid point and the moving front. From the above definition, it can be seen that the interface is represented by the zero level sets [200], also see Figure A.13.

A.6.3 Coupled Level Set and Volume of Fluid Method

Both the VOF and level set methods possess advantages and drawbacks, as discussed before. Therefore, techniques were developed that combine both interface representations, leading to an improvement in accuracy and mass conservation properties [185]. One such technique is the coupled level set and volume of fluid method (CLSVOF) developed by Sussman & Puckett [193]. The CLSVOF technique uses the VOF method to calculate the volume fraction field and the level set method to compute the geometrical properties at the interface and update the physical properties (density and viscosity) [183, 203]. Because ϕ_{LS} from the level set method is continuous, calculating the interface normal and curvature is simple and accurate, in contrast to the techniques used in the purely VOF method [200]. However, due to the coupling between the two techniques, the implementation of the CLSVOF method becomes increasingly complex [195]. Furthermore, as with many mixed methods, switching between interface representations is difficult without losing accuracy of the interface position [185].

A.6.4 Phase-field Method

Anderson et al. [189] discuss the fact that the bulk fluids and their interface can be distinguished by the density ρ in many gas-liquid situations. Such a parameter is also called an order parameter. When one's intention is to model the solidification of a single-component material (such as dendritic growth), the phase field ϕ_{PF} is used to characterise the phases. Distinct constant values of ϕ_{PF} are assigned to each bulk phase [189, 201]:

$$\phi_{PF}(x,t) = \begin{cases} -1, & \text{in the solid,} \\ -1 < \phi_{PF}(x,t) < 1, & \text{at the interface,} \\ 1, & \text{in the liquid.} \end{cases} \tag{A.50}$$

As the method is designed for solidification purposes, and not necessarily for gas-liquid modelling, the focus for application in bubble behaviour will lie mainly on the two methods described in the first two sections and their combination

A.7 Conclusion

In this literature study, multiple components of bubble behaviour have been investigated. Several regimes exist for bubble generation, where the classification, and thus the generated bubble size, depends on whether one is dealing with a quiescent or a flowing liquid and a quasi-static or dynamic case. For these regimes, different expressions exist with which the bubble size can be approximated, often depending on the Capillary, Bond, or Weber number.

After bubble generation, coalescence might occur, increasing bubble sizes. Whether coalescence occurs or not depends on the collision frequency and the coalescence efficiency. Both effects can be described by multiple mechanisms. Most models, however, assume one of the mechanisms to be dominant, neglecting the others without validation [126]. Similarly, various models for bubble break-up frequently assume that the inertial force or energy constraint is dominant, ignoring the effect of, amongst others, viscous shear force [158]. Currently, however, incorporating multiple or all mechanisms for coalescence or break-up into a single model appears to be too difficult.

Surfactants influence the three stages of bubble behaviour described in the study. By lowering a liquid's surface tension, generated bubbles may be smaller, coalescence may occur more slowly, or the break-up frequency may be increased.

To model the behaviour of bubbles, numerical solvers are often utilised. Two main approaches, the Lagrangian approach and the Eulerian approach, are applied often in numerical simulations. Since they can handle large deformations well, Eulerian descriptions for the interface of a two-phase flow are frequently used. Within the Eulerian approach, the volume of fluid (VOF) method and the level set method are often applied. Whereas the VOF method proves cumbersome when dealing with smooth properties, such as the curvature of an interface, the level set method is susceptible to numerical dissipation, causing the loss of mass conservation. The combination of both methods leads to the coupled level set and volume of fluid method (CLSVOF) which aims to improve on both separate methods. The coupling of the two mechanisms, however, leads to an increase in complexity. Therefore, one should carefully select a modelling method for their application based on the advantages and disadvantages of each method.

Bibliography

[1] Herrada, M. A. and Eggers, J. G. "Path instability of an air bubble rising in water". In: *Proceedings of the National Academy of Sciences* 120.4 (2023). DOI: 10.1073/pnas.2216830120.

[2] Tripathi, M. K. et al. "Two initially spherical bubbles rising in quiescent liquid". In: *Physical Review Fluids* 2.7 (2017). DOI: 10.1103/PhysRevFluids.2.073601.

[3] Prosperetti, A. "Bubbles". In: *Physics of Fluids* 16.6 (2004), pp. 1852–1865. DOI: 10.1063/1.1695308.

[4] Aboulhasanzadeh, B. and Tryggvason, G. "Effect of bubble interactions on mass transfer in bubbly flow". In: *International Journal of Heat and Mass Transfer* 79 (2014), pp. 390–396. DOI: 10.1016/j.ijheatmasstransfer.2014.08.027.

[5] W. D. Deckwer. *Bubble Column Reactors*. Singapore: Wiley, 1992.

[6] Tripathi, M. K.; Sahu, K. C. and Govindarajan, R. "Dynamics of an initially spherical bubble rising in quiescent liquid". In: *Nature Communications* 6.1 (2015), p. 6268. DOI: 10.1038/ncomms7268.

[7] Duineveld, P. C. "The rise velocity and shape of bubbles in pure water at high Reynolds number". In: *J. Fluid Mech.* 292 (1995), pp. 325–332. DOI: 10.1017/S0022112095001546.

[8] Haberman, W. and Morton, R. *An experimental investigation of the drag and shape of air bubbles rising in various liquids*. Tech. rep. Washington: David Taylor Model Basin Rep. 802, 1953.

[9] A.W.G. de Vries. "Path and Wake of a Rising Bubble". PhD thesis. Enschede: University of Twente, 2001. URL: https://ris.utwente.nl/ws/portalfiles/portal/6074159/t0000018.pdf.

[10] Schiller, L. "Handbuch der Experimentalphysik". In: *Nature* 131.3313 (1933), pp. 602–603. DOI: 10.1038/131602a0.

[11] Saffman, P. G. "On the motion of small spheroidal particles in a viscous liquid". In: *J. Fluid Mech.* 1.5 (1956), pp. 540–553. DOI: 10.1017/S0022112056000354.

[12] Mougin, G. and Magnaudet, J. "Path Instability of a Rising Bubble". In: *Physical Review Letters* 88.1 (2001), p. 014502. DOI: 10.1103/PhysRevLett.88.014502.

[13] Vries, A. de; Biesheuvel, A. and Wijngaarden, L. van. "Notes on the path and wake of a gas bubble rising in pure water". In: *Int. J. Multiphase Flow* 28.11 (2002), pp. 1823–1835. DOI: 10.1016/S0301-9322(02)00036-8.

[14] Cano-Lozano, J. C. et al. "Paths and wakes of deformable nearly spheroidal rising bubbles close to the transition to path instability". In: *Physical Review Fluids* 1.5 (2016), p. 053604. DOI: 10.1103/PhysRevFluids.1.053604.

[15] Legendre, D.; LAUGA, E. and Magnaudet, J. "Influence of slip on the dynamics of two-dimensional wakes". In: *J. Fluid Mech.* 633 (2009), pp. 437–447. DOI: 10.1017/S0022112009008015.

[16] Leal, L. G. "Vorticity transport and wake structure for bluff bodies at finite Reynolds number". In: *Physics of Fluids A: Fluid Dynamics* 1.1 (1989), pp. 124–131. DOI: 10.1063/1.857540.

[17] Marsden, J. and McCracken, M. *The Hopf Bifurcation and Its Applications*. Ed. by F. John et al. Vol. 19. New York: Springer-Verlag, 1976. DOI: https://doi.org/10.1007/978-1-4612-6374-6.

[18] Bonnefis, P.; Fabre, D. and Magnaudet, J. "When, how, and why the path of an air bubble rising in pure water becomes unstable". In: *Proceedings of the National Academy of Sciences* 120.11 (2023), e2300897120. DOI: 10.1073/pnas.2300897120.

[19] Magnaudet, J. and Eames, I. "The Motion of High-Reynolds-Number Bubbles in Inhomogeneous Flows". In: *Annual Review of Fluid Mechanics* 32.1 (2000), pp. 659–708. DOI: 10.1146/annurev.fluid.32.1.659.

[20] Tagawa, Y.; Takagi, S. and Matsumoto, Y. "Surfactant effect on path instability of a rising bubble". In: *J. Fluid Mech.* 738 (2014), pp. 124–142. DOI: 10.1017/jfm.2013.571.

[21] Clift, R.; Grace, J. and Weber, M. *Bubbles, Drops, and Particles*. Mineola: Dover, 2005.

[22] Bhaga, D. and Weber, M. "Bubbles in viscous liquids : shapes, wakes and velocities". In: *J. Fluid Mech* (1981), pp. 61–85. DOI: https://doi.org/10.1017/S002211208100311X.

[23] Cano-Lozano, J. C.; Bohorquez, P. and Martínez-Bazán, C. "Wake instability of a fixed axisymmetric bubble of realistic shape". In: *Int. J. Multiphase Flow* 51 (2013), pp. 11–21. DOI: 10.1016/j.ijmultiphaseflow.2012.11.005.

[24] Cano-Lozano, J. C. et al. "A global stability approach to wake and path instabilities of nearly oblate spheroidal rising bubbles". In: *Physics of Fluids* 28.1 (2016). DOI: 10.1063/1.4939703.

[25] Legendre, D.; Magnaudet, J. and Mougin, G. "Hydrodynamic interactions between two spherical bubbles rising side by side in a viscous liquid". In: *J. Fluid Mech.* 497 (2003), pp. 133–166. DOI: 10.1017/S0022112003006463.

[26] Filella, A.; Ern, P. and Roig, V. "Interaction of two oscillating bubbles rising in a thin-gap cell: Vertical entrainment and interaction with vortices". In: *J. Fluid Mech.* 888 (2020). DOI: 10.1017/jfm.2020.4.

[27] Duineveld, P. E. "Bouncing and Coalescence of Bubble Pairs Rising at High Reynolds Number in Pure Water or Aqueous Surfactant Solutions". In: *Applied Scientific Research* 58 (1998), pp. 409–439. DOI: https://doi.org/10.1023/A:1000825909824.

[28] Wijngaarden, L. van. "The mean rise velocity of pairwise-interacting bubbles in liquid". In: *J. Fluid Mech* 251 (1993), pp. 55–78. DOI: https://doi.org/10.1017/S0022112093003337.

[29] Sanada, T. et al. "Motion and coalescence of a pair of bubbles rising side by side". In: *Chemical Engineering Science* 64.11 (2009), pp. 2659–2671. DOI: 10.1016/j.ces.2009.02.042.

[30] Kong, G. et al. "Hydrodynamic interaction of bubbles rising side-by-side in viscous liquids". In: *Experiments in Fluids* 60.10 (2019), p. 155. DOI: 10.1007/s00348-019-2798-y.

[31] Kusuno, H. and Sanada, T. "Flow Structure and Deformation of Two Bubbles Rising Side by Side in a Quiescent Liquid". In: *Fluids* 6.11 (2021), p. 390. DOI: 10.3390/fluids6110390.

[32] Kusuno, H. and Sanada, T. "Wake-induced lateral migration of approaching bubbles". In: *Int. J. Multiphase Flow* 139 (2021). DOI: 10.1016/j.ijmultiphaseflow.2021.103639.

[33] Zhang, J.; Ni, M.-J. and Magnaudet, J. "Three-dimensional dynamics of a pair of deformable bubbles rising initially in line. Part 1: Moderately inertial regimes". In: *J. Fluid Mech.* 920.A16 (2021). DOI: 10.1017/jfm.2021.429.

[34] Zhang, J.; Ni, M.-J. and Magnaudet, J. "Three-dimensional dynamics of a pair of deformable bubbles rising initially in line. Part 2: Highly inertial regimes". In: *J. Fluid Mech.* 943.A10 (2022). DOI: 10.1017/jfm.2022.416.

[35] Watanabe, M. and Sanada, T. "In-Line Motion of a Pair of Bubbles in a Viscous Liquid". In: *JSME Int. J., Ser. B* 49.2 (2006), pp. 410–418. DOI: 10.1299/jsmeb.49.410.

[36] Kusuno, H.; Yamamoto, H. and Sanada, T. "Lift force acting on a pair of clean bubbles rising in-line". In: *Physics of Fluids* 31.7 (2019), p. 072105. DOI: 10.1063/1.5100183.

[37] Harper, J. F. "On bubbles rising in line at large Reynolds numbers". In: *J. Fluid Mech* (1970), pp. 751–758. DOI: https://doi.org/10.1017/S0022112070000897.

[38] Yuan A N, H. and Prosperetti, D. A. "On the in-line motion of two spherical bubbles in a viscous fluid". In: *J. Fluid Mech* (1994), pp. 325–349. DOI: https://doi.org/10.1017/S0022112094003733.

[39] Mirsandi, H. et al. "Numerical study on the interaction of two bubbles rising side-by-side in viscous liquids". In: *Chemical Engineering Journal* 410 (2021), p. 128257. DOI: 10.1016/j.cej.2020.128257.

[40] Katz, J. and Meneveau, C. "Wake-induced relative motion of bubbles rising in line". In: *Int. J. Multiphase Flow* 22.2 (1996), pp. 239–258. DOI: https://doi.org/10.1016/0301-9322(95)00081-X.

[41] Harper, J. "Bubbles rising in line: why is the first approximation so bad?" In: *J. Fluid Mech* 351 (1997), pp. 289–300. DOI: https://doi.org/10.1017/S0022112097007118.

[42] Ramírez-Muñoz, J. et al. "Hydrodynamic interaction on large-Reynolds-number aligned bubbles: Drag effects". In: *Nuclear Engineering and Design* 241.7 (2011), pp. 2371–2377. DOI: 10.1016/j.nucengdes.2011.03.051.

[43] Gumulya, M. et al. "Interaction of bubbles rising inline in quiescent liquid". In: *Chemical Engineering Science* 166 (2017), pp. 1–10. DOI: 10.1016/j.ces.2017.03.013.

[44] Hallez, Y. and Legendre, D. "Interaction between two spherical bubbles rising in a viscous liquid". In: *J. Fluid Mech.* 673 (2011), pp. 406–431. DOI: 10.1017/S002211201000635X.

[45] Sanada, T. et al. "Behavior of a single coherent gas bubble chain and surrounding liquid jet flow structure". In: *Chemical Engineering Science* 60.17 (2005), pp. 4886–4900. DOI: 10.1016/j.ces.2005.04.010.

[46] Bunner, B. and Tryggvason, G. "Dynamics of homogeneous bubbly flows part 1. Rise velocity and microstructure of the bubbles". In: *J. Fluid Mech.* 466 (2002), pp. 17–52. DOI: 10.1017/S0022112002001179.

[47] Adoua, R.; Legendre, D. and Magnaudet, J. "Reversal of the lift force on an oblate bubble in a weakly viscous linear shear flow". In: *Journal of Fluid Mechanics* 628 (2009), pp. 23–41. DOI: 10.1017/S0022112009006090.

[48] J.F. Harper. "Harper". In: *Bubbles in Food 2*. Ed. by G. M. Campbell; M.G. Scanlon and D. L. Pyle. AACC International Press, 2008. Chap. 15, pp. 147–152. DOI: https://doi.org/10.1016/B978-1-891127-59-5.50019-5.

[49] Wu, M. and Gharib, M. "Experimental studies on the shape and path of small air bubbles rising in clean water". In: *Physics of Fluids* 14.7 (2002). DOI: 10.1063/1.1485767.

[50] Li, C. et al. "Numerical simulation on the terminal rise velocity and mass transfer rate of single sub-millimeter bubbles". In: *Chemical Engineering Science* 246 (2021). DOI: 10.1016/j.ces.2021.116963.

[51] Zhang, J.; Chen, L. and Ni, M.-J. "Vortex interactions between a pair of bubbles rising side by side in ordinary viscous liquids". In: *Phys. Rev. Fluids* 4 (4 2019), p. 043604. DOI: 10.1103/PhysRevFluids.4.043604.

[52] Martín, M. et al. "Shape oscillating bubbles: hydrodynamics and mass transfer - a review". In: *Bubble Science, Engineering & Technology* 3.2 (2011), pp. 48–63. DOI: 10.1179/1758897911Y.0000000006.

[53] Baz-Rodriguez, S.; Aguilar-Corona, A. and Soria, A. "Rising velocity for single bubbles in pure liquids". In: *Revista Mexicana de Ingeniería Química* 11.2 (2012), pp. 269–278. URL: https://www.redalyc.org/pdf/620/62026895006.pdf.

[54] Van Der Lans, R. "Hydrodynamics of a Bubble Column Loop Reactor". PhD thesis. Delft: Delft University of Technology, 1985. URL: https://repository.tudelft.nl/islandora/object/uuid:33d1d9d9-0cd9-455e-87b5-18606319974d/datastream/OBJ/download.

[55] Shah, Y. T. et al. "Design parameters estimations for bubble column reactors". In: *AIChE Journal* 28.3 (1982), pp. 353–379. DOI: https://doi.org/10.1002/aic.690280302.

[56] Ruzicka, M. et al. "Homogeneous–heterogeneous regime transition in bubble columns". In: *Chemical Engineering Science* 56.15 (2001), pp. 4609–4626. DOI: https://doi.org/10.1016/S0009-2509(01)00116-6.

[57] Park, S. H. et al. "A Simple Parameterization for the Rising Velocity of Bubbles in a Liquid Pool". In: *Nuclear Engineering and Technology* 49.4 (2017), pp. 692–699. DOI: 10.1016/j.net.2016.12.006.

[58] Manica, R.; Klaseboer, E. and Chan, D. Y. "The hydrodynamics of bubble rise and impact with solid surfaces". In: *Advances in Colloid and Interface Science* 235 (2016), pp. 214–232. DOI: 10.1016/j.cis.2016.06.010.

[59] Manica, R.; Klaseboer, E. and Chan, D. Y. "The impact and bounce of air bubbles at a flat fluid interface". In: *Soft Matter* 12.13 (2016), pp. 3271–3282. DOI: 10.1039/c5sm03151f.

[60] Morente, A.; Laviéville, J. and Legendre, D. "A penalization method for the simulation of bubbly flows". In: *Journal of Computational Physics* 374 (2018), pp. 563–590. DOI: 10.1016/j.jcp.2018.07.042.

[61] Yang, B.; Prosperetti, A. and Takagi, S. "The transient rise of a bubble subject to shape or volume changes". In: *Physics of Fluids* 15.9 (2003), pp. 2640–2648. DOI: 10.1063/1.1592800.

[62] Bugg, J. D. and Rowe, R. D. "Modelling the initial motion of large cylindrical and spherical bubbles". In: *International Journal for Numerical Methods in Fluids* 13 (1991), pp. 109–129. DOI: 10.1002/fld.1650130107.

[63] Walters, J. and Davidson, J. "The initial motion of a gas bubble formed in an inviscid liquid Part 2. The three-dimensional bubble and the toroidal bubble". In: *Journal of Fluid Mechanics* 17.3 (1963), pp. 321–336. DOI: 10.1017/S0022112063001373.

[64] Walters, J. K. and Davidson, J. F. "The initial motion of a gas bubble formed in an inviscid liquid Part 1. The two-dimensional bubble". In: *Journal of Fluid Mechanics* 12.3 (1962), pp. 408–416. DOI: 10.1017/S0022112062000300.

[65] Dominik, M. and Cassel, K. W. "Analysis of Initial Bubble Acceleration Using the Level-Set Method". In: *The Journal of Computational Multiphase Flows* 7.3 (2015), pp. 129–142. DOI: 10.1260/1757-482X.7.3.129.

[66] Popinet, S. "An accurate adaptive solver for surface-tension-driven interfacial flows". In: *Journal of Computational Physics* 228.16 (2009), pp. 5838–5866. DOI: 10.1016/j.jcp.2009.04.042.

[67] Popinet, S. "A quadtree-adaptive multigrid solver for the Serre-Green-Naghdi equations". In: *Journal of Computational Physics* 302 (2015). DOI: 10.1016/j.jcp.2015.09.009.

[68] Hooft, J. A. van et al. "Towards Adaptive Grids for Atmospheric Boundary-Layer Simulations". In: *Boundary-Layer Meteorology* 167.3 (2018), pp. 421–443. DOI: 10.1007/s10546-018-0335-9.

[69] Manica, R.; Klaseboer, E. and Chan, D. Y. C. "Force Balance Model for Bubble Rise, Impact, and Bounce from Solid Surfaces". In: *Langmuir* 31.24 (2015), pp. 6763–6772. DOI: 10.1021/acs.langmuir.5b01451.

[70] Moore, D. W. "The velocity of rise of distorted gas bubbles in a liquid of small viscosity". In: *J. Fluid Nech* 4 (1965), pp. 749–766. DOI: https://doi.org/10.1017/S0022112065001660.

[71] Parkinson, L. et al. "The terminal rise velocity of 10-100 μm diameter bubbles in water". In: *Journal of Colloid and Interface Science* 322.1 (2008), pp. 168–172. DOI: 10.1016/j.jcis.2008.02.072.

[72] Stokes, G. "On the Effect of the Internal Friction of Fluids on the Motion of Pendulums". In: *Transactions of the Cambridge Philosophical Society* 9 (1851), pp. 120–218. URL: https://ui.adsabs.harvard.edu/abs/1851TCaPS...9....8S.

[73] Oseen, C. W. "Über die Stokes'sche formel und über eine verwandte Aufgabe in der Hydrodynamik". In: *Arkiv för matematik, astronomi och fysik* 7.1 (1911). URL: https://books.google.nl/books?id=SB64nQEACAAJ.

[74] Oseen, C. W. *Neuere Methoden und Ergebnisse in der Hydrodynamik*. Leipzig: Akademische Verlagsgesellschaft, 1927. URL: https://archive.org/details/in.ernet.dli.2015.80409/page/n7/mode/2up.

[75] Mazur, P. and Weisenborn, A. J. "The Oseen drag on a sphere and the method of induced forces". In: *Physica A: Statistical Mechanics and its Applications* 123.1 (1984), pp. 209–226. DOI: https://doi.org/10.1016/0378-4371(84)90112-2.

[76] Batchelor, G. *An introduction to fluid dynamics*. Cambridge: Cambridge University Press, 2000, pp. 240–246. DOI: https://doi.org/10.1017/CBO9780511800955.

[77] Levich, V. "The motion of bubbles at high Reynolds numbers". In: *Zh. Eksp. Teor. Fiz* 19.18 (1949), 436ff.

[78] Moore, D. W. "The boundary layer on a spherical gas bubble". In: *J. Fluid Mech.* 16.2 (1963), pp. 161–176. DOI: https://doi.org/10.1017/S0022112063000665.

[79] Kang, I. S. and Leal, L. G. "The drag coefficient for a spherical bubble in a uniform streaming flow". In: *The Physics of Fluids* 31.2 (1988), pp. 233–237. DOI: 10.1063/1.866852.

[80] Mei, R.; Klausner, J. F. and Lawrence, C. J. "A note on the history force on a spherical bubble at finite Reynolds number". In: *Physics of Fluids* 6.1 (1994), pp. 418–420. DOI: 10.1063/1.868039.

[81] Rastello, M.; Marié, J. L. and Lance, M. "Drag and lift forces on clean spherical and ellipsoidal bubbles in a solid-body rotating flow". In: *J. Fluid Mech.* 682 (2011), pp. 434–459. DOI: 10.1017/jfm.2011.240.

[82] Taylor, T. D. and Acrivos, A. "On the deformation and drag of a falling viscous drop at low Reynolds number". In: *J. Fluid Mech* 18.3 (1964), pp. 466–476. DOI: https://doi.org/10.1017/S0022112064000349.

[83] Loth, E. "Quasi-steady shape and drag of deformable bubbles and drops". In: *Int. J. Multiphase Flow* 34.6 (2008), pp. 523–546. DOI: 10.1016/j.ijmultiphaseflow.2007.08.010.

[84] Jamialahmadi, M.; Branch, C. and Müller-Steinhagen, H. "Terminal bubble rise velocity in liquids". In: *Chemical Engineering Research & Design* 72 (1994), p. 119. URL: https://www.scopus.com/record/display.uri?eid=2-s2.0-0028139516&origin=inward&txGid=f402fbbafb33295339010ec9ec0f269f.

[85] Wallis, G. B. "The terminal speed of single drops or bubbles in an infinite medium". In: *Int. J. Multiphase Flow* 1 (1974), pp. 491–511. DOI: https://doi.org/10.1016/0301-9322(74)90003-2.

[86] Levich, V. *Physicochemical hydrodynamics*. Prentice-Hall Englewood Cliffs, 1962. DOI: 10.1149/1.2425619.

[87] Lehrer, I. H. "A rational terminal velocity equation for bubbles and drops at intermediate and high Reynolds numbers". In: *Journal of Chemical Engineering of Japan* 9.3 (1976), pp. 237–240. DOI: https://doi.org/10.1252/jcej.9.237.

[88] Sanada, T. et al. "Motion and drag of a single bubble in super-purified water". In: *Fluid Dynamics Research* 40.7-8 (2008), pp. 534–545. DOI: 10.1016/j.fluiddyn.2007.12.005.

[89] Pawliszak, P. et al. "Mobile or Immobile? Rise Velocity of Air Bubbles in High Purity Water". In: *The Journal of Physical Chemistry C* 123.24 (2019), pp. 15131–15138. DOI: 10.1021/acs.jpcc.9b03526.

[90] Klaseboer, E. et al. "Model and experiments of a drop impinging on an immersed wall". In: *Physics of Fluids* 13.1 (2001), pp. 45–57. DOI: 10.1063/1.1331313.

[91] Legendre, D.; Zenit, R. and Velez-Cordero, J. R. "On the deformation of gas bubbles in liquids". In: *Physics of Fluids* 24.4 (2012). DOI: 10.1063/1.4705527.

[92] Zawala, J. and Malysa, K. "Influence of the impact velocity and size of the film formed on bubble coalescence time at water surface". In: *Langmuir* 27.6 (2011), pp. 2250–2257. DOI: 10.1021/la104324u.

[93] Boussinesq, V. "Sur la résistance qu'oppose un liquide indéfini en repos". In: *C.R. Acad. Sci. Paris* 100 (1885), pp. 935–937.

[94] Basset, A. *A Treatise on Hydrodynamics: with Numerous Examples*. Deighton: Bell and Co, 1888. URL: https://archive.org/details/atreatiseonhydr02bassgoog/page/n4/mode/2up.

[95] Takagi, S. and Matsumoto, Y. "Force acting on a rising bubble in a quiescent liquid". In: *American Society of Mechanical Engineers, Fluids Engineering Division (Publication) FED* 236 (1996), pp. 575–580. URL: https://www.scopus.com/inward/record.uri?eid=2-s2.0-0030361773&partnerID=40&md5=12e59b3f60f362592e160d446996408c.

[96] Kok, J. "Dynamics of a pair of gas bubbles moving through liquid, part II. Experiment." In: *Eur. J. Mech. B/Fluids* 12.4 (1993), pp. 541–560.

[97] Van Wijngaarden, L. "Hydrodynamic interaction between gas bubbles in liquid". In: *J. Fluid Mech* 71.1 (1976), pp. 21–44. DOI: https://doi.org/10.1017/S0022112076001110.

[98] Magnaudet, J. and Mougin, G. "Wake instability of a fixed spheroidal bubble". In: *J. Fluid Mech.* 572 (2007), pp. 311–337. DOI: 10.1017/S0022112006003442.

[99] Kok, J. "Dynamics of gas bubbles moving through liquid part I. Theory." In: *Eur. J Mech., B/Fluids* 12.4 (1993), pp. 515–540.

[100] Vasseur, P. and Cox, R. G. "The lateral migration of spherical particles sedimenting in a stagnant bounded fluid". In: *J. Fluid Mech* 80 (1977), pp. 561–591. DOI: https://doi.org/10.1017/S0022112077001840.

[101] Drenckhan, W. and Saint-Jalmes, A. "The science of foaming". In: *Advances in Colloid and Interface Science* 222 (2015), pp. 228–259. DOI: 10.1016/j.cis.2015.04.001.

[102] Pugh, R. J. "Generation of bubbles and foams". In: *Bubble and Foam Chemistry*. Cambridge University Press, 2016, pp. 155–193. DOI: 10.1017/CBO9781316106938.006.

[103] Satter, A. and Iqbal, G. M. "Reservoir rock properties". In: *Reservoir Engineering*. Elsevier, 2016, pp. 29–79. DOI: 10.1016/B978-0-12-800219-3.00003-6.

[104] Kumaran, V. and Koch, D. L. "The effect of hydrodynamic interactions on the average properties of a bidisperse suspension of high Reynolds number, low Weber number bubbles". In: *Physics of Fluids A: Fluid Dynamics* 5.5 (1993), pp. 1123–1134. DOI: 10.1063/1.858598.

[105] Gennes, P.-G. de; Brochard-Wyart, F. and Quéré, D. *Capillarity and Wetting Phenomena*. 1st. New York, NY: Springer New York, 2004. DOI: 10.1007/978-0-387-21656-0.

[106] Bresme, F. "Theoretical approaches to investigate anisotropic particles at fluid interfaces". In: *Anisotropic Particle Assemblies*. Elsevier, 2018, pp. 233–260. DOI: 10.1016/B978-0-12-804069-0.00008-3.

[107] Bari, S. D. and Robinson, A. J. "Experimental study of gas injected bubble growth from submerged orifices". In: *Experimental Thermal and Fluid Science* 44 (2013), pp. 124–137. DOI: 10.1016/j.expthermflusci.2012.06.005.

[108] Davidson, J. and Schüler, B. "Bubble formation at an orifice in a viscous liquid". In: *Chemical Engineering Research and Design* 75 (1960), S105–S115. DOI: 10.1016/S0263-8762(97)80008-1.

[109] Berghmans, J. "Stability of gas bubbles rising in inviscid fluids". In: *Chemical Engineering Science* 28.11 (1973), pp. 2005–2011. DOI: 10.1016/0009-2509(73)85044-4.

[110] Jamialahmadi, M. et al. "Study of Bubble Formation Under Constant Flow Conditions". In: *Chemical Engineering Research and Design* 79.5 (2001), pp. 523–532. DOI: 10.1205/02638760152424299.

[111] Mirsandi, H. et al. "Bubble formation from an orifice in liquid cross-flow". In: *Chemical Engineering Journal* 386 (2020), p. 120902. DOI: 10.1016/J.CEJ.2019.01.181.

[112] Garstecki, P.; Gañán-Calvo, A. and Whitesides, G. "Formation of Droplets and Bubbles in Microfluidic Systems". In: *Bulletin of the Polish Academy of Sciences: Technical Sciences* 53.4 (2005), pp. 361–372. DOI: 10.1007/978-90-481-9029-4{_}9.

[113] Raven, J.-P.; Marmottant, P. and Graner, F. "Dry microfoams: formation and flow in a confined channel". In: *The European Physical Journal B* 51.1 (2006), pp. 137–143. DOI: 10.1140/epjb/e2006-00197-6.

[114] Lorenceau, E. et al. "A high rate flow-focusing foam generator". In: *Physics of Fluids* 18.9 (2006), p. 097103. DOI: 10.1063/1.2353799.

[115] Nunes, J. K. et al. "Dripping and jetting in microfluidic multiphase flows applied to particle and fibre synthesis". In: *Journal of Physics D: Applied Physics* 46.11 (2013), p. 114002. DOI: 10.1088/0022-3727/46/11/114002.

[116] Guillot, P. et al. "Droplets and jets in microfluidic devices". In: *Comptes Rendus Chimie* 12.1-2 (2009), pp. 247–257. DOI: 10.1016/j.crci.2008.07.005.

[117] Utada, A. S. et al. "Dripping to Jetting Transitions in Coflowing Liquid Streams". In: *Physical Review Letters* 99.9 (2007), p. 094502. DOI: 10.1103/PhysRevLett.99.094502.

[118] Munson, B.; Young, D. and Okiishi, T. *Fundamentals of Fluid Mechanics*. 4th. New Jersey: Wiley, 2001.

[119] Mosdorf, R. and Wyszkowski., T. "Self-organising structure of bubble departures". In: *International Journal of Heat and Mass Transfer* 61 (2013), pp. 277–286. DOI: 10.1016/j.ijheatmasstransfer.2013.02.008.

[120] Pereira, F. A. C.; Colli, E. and Sartorelli, J. C. "Synchronization of two bubble trains in a viscous fluid: Experiment and numerical simulation". In: *Physical Review E* 87.2 (2013), p. 022917. DOI: 10.1103/PhysRevE.87.022917.

[121] Loimer, T.; Machu, G. and Schaflinger, U. "Inviscid bubble formation on porous plates and sieve plates". In: *Chemical Engineering Science* 59.4 (2004), pp. 809–818. DOI: 10.1016/j.ces.2003.10.020.

[122] Amol A. Kulkarni and Joshi, J. B. "Bubble Formation and Bubble Rise Velocity in Gas-Liquid Systems: A Review". In: *Ind. Eng. Chem. Res.* 44.16 (2005), pp. 5873–5931. DOI: 10.1021/IE049131P.

[123] Chu, P. et al. "A review of bubble break-up". In: *Advances in Colloid and Interface Science* 270 (2019), pp. 108–122. DOI: 10.1016/J.CIS.2019.05.010.

[124] Luo, H. "Coalescence, breakup and liquid circulation in bubble column reactors". PhD thesis. Trondheim: The Norwegian Institute of Technology, 1993. URL: https://ntrl.ntis.gov/NTRL/dashboard/searchResults/titleDetail/DE95772440.xhtml.

[125] Lee, C.-H.; Erickson, L. and Glasgow, L. "Bubble breakup and coalescence in turbulent gas-liquid dispersions". In: *Chemical Engineering Communications* 59.1-6 (1987), pp. 65–84. DOI: 10.1080/00986448708911986.

[126] Liao, Y. and Lucas, D. "A literature review on mechanisms and models for the coalescence process of fluid particles". In: *Chemical Engineering Science* 65.10 (2010), pp. 2851–2864. DOI: 10.1016/J.CES.2010.02.020.

[127] Kataoka, I. and Serizawa, A. "Bubble Flow". In: *A-to-Z Guide to Thermodynamics, Heat and Mass Transfer, and Fluids Engineering* (2010). DOI: 10.1615/ATOZ.B.BUBBLE{_}FLOW.

[128] Kennard, E. *Kinetic Theory of Gases, with an Introduction to Statistical Mechanics*. 1st. New York: McGraw-Hill, 1938. URL: https://www.scirp.org/(S(lz5mqp453edsnp55rrgjct55))/reference/ReferencesPapers.aspx?ReferenceID=1349982.

[129] Prince, M. J. and Blanch, H. W. "Bubble coalescence and break-up in air-sparged bubble columns". In: *AIChE Journal* 36.10 (1990), pp. 1485–1499. DOI: 10.1002/AIC.690361004.

[130] Edinburgh Datashare. *Isotropic Turbulence*. URL: https://datashare.ed.ac.uk/handle/10283/775.

[131] Hinze, J. *Turbulence: An Inotrduction to Its Mechanism and Theory*. New York: McGraw-Hill, 1959.

[132] Rotta, J. C. *Turbulente Strömungen*. 1st ed. Wiesbaden: Vieweg+Teubner Verlag, 1972. DOI: 10.1007/978-3-322-91206-0.

[133] Friedlander, S. K. *Smoke, Dust, and Haze*. 2nd. New York: Oxford University Press, 2000. URL: https://www.eng.uc.edu/~beaucag/Classes/Properties/Books/(Topics%20in%20Chemical%20Engineering)%20Sheldon%20K.%20Friedlander%20-%20Smoke,%20Dust,%20and%20Haze_%20Fundamentals%20of%20Aerosol%20Dynamics-Oxford%20University%20Press%20(2000).pdf.

[134] Shinnar, R. and Church, J. M. "Statistical Theories of Turbulence in Predicting Particle Size in Agitated Dispersions". In: *Industrial and Engineering Chemistry* 52.3 (1960), pp. 253–256. DOI: 10.1021/IE50603A036/ASSET/IE50603A036.FP.PNG{_}V03.

[135] Marrucci, G. "A theory of coalescence". In: *Chemical Engineering Science* 24.6 (1969), pp. 975–985. DOI: 10.1016/0009-2509(69)87006-5.

[136] Chesters, A. "The modelling of coalescence processes in fluid-liquid dispersions : a review of current understanding". In: *Chemical Engineering Research and Design* 69.A4 (1991). Ed. by G. Balint et al., pp. 259–270. DOI: 10.2/JQUERY.MIN.JS.

[137] Ross, S. L. "Measurements and Models of the Dispersed Phase Mixing Process". PhD thesis. Michigan: University of Michigan, 1971. DOI: 10.7302/Z2028PQ6.

[138] Coulaloglou, C. "Dispersed phase interactions in an agitated flow vessel". PhD thesis. Chicago: Illinois Institute of Technology, 1975. URL: https://www.proquest.com/openview/cccc5ab44a92696db5b10d2d78c8738a/1?pq-origsite=gscholar&cbl=18750&diss=y.

[139] Boshenyatov, B. "Laws of Bubble Coalescence and their Modeling". In: *New Developments in Hydrodynamics Research*. Ed. by M. Ibragimov and M. Anisimov. New York: Nova Science Publishers, 2012, pp. 211–240.

[140] Lee, J. and Hodgson, T. "Film flow and coalescence-I Basic relations, film shape and criteria for interface mobility". In: *Chemical Engineering Science* 23.11 (1968), pp. 1375–1397. DOI: 10.1016/0009-2509(68)89047-5.

[141] Chesters, A. K. and Hofman, G. "Bubble coalescence in pure liquids". In: *Applied Scientific Research* 38.1 (1982), pp. 353–361. DOI: 10.1007/BF00385965.

[142] Simon, M. "Koaleszenz von Tropfen und Tropfenschwarmen". PhD thesis. die Teschinschen Universtitat Kaiserslautern, 2004. URL: http://nbn-resolving.de/urn:nbn:de:hbz:386-kluedo-18968.

[143] Mackay, G. D. M. and Mason, S. G. "The gravity approach and coalescence of fluid drops at liquid interfaces". In: *The Canadian Journal of Chemical Engineering* 41.5 (1963), pp. 203–212. DOI: 10.1002/cjce.5450410504.

[144] Kamp, A. et al. "Bubble coalescence in turbulent flows: A mechanistic model for turbulence-induced coalescence applied to microgravity bubbly pipe flow". In: *Int. J. Multiphase Flow* 27.8 (2001), pp. 1363–1396. DOI: 10.1016/S0301-9322(01)00010-6.

[145] Kim, J. W. and Lee, W. K. "Coalescence behavior of two bubbles in stagnant liquids." In: *Journal of Chemical Engineering of Japan* 20.5 (1987), pp. 448–453. DOI: 10.1252/jcej.20.448.

[146] Kirkpatrick, R. and Lockett, M. "The influence of approach velocity on bubble coalescence". In: *Chemical Engineering Science* 29.12 (1974), pp. 2363–2373. DOI: 10.1016/0009-2509(74)80013-8.

[147] Vrij, A. "Possible mechanism for the spontaneous rupture of thin, free liquid films". In: *Discussions of the Faraday Society* 42 (1966), p. 23. DOI: 10.1039/df9664200023.

[148] Howarth, W. "Coalescence of drops in a turbulent flow field". In: *Chemical Engineering Science* 19.1 (1964), pp. 33–38. DOI: 10.1016/0009-2509(64)85003-X.

[149] Park, J. and Blair, L. "The effect of coalescence on drop size distribution in an agitated liquid-liquid dispersion". In: *Chemical Engineering Science* 30.9 (1975), pp. 1057–1064. DOI: 10.1016/0009-2509(75)87007-2.

[150] Kuboi, R.; Komasawa, I. and Otake, T. "Collision and coalescence of dispersed drops in turbulent liquid flow". In: *Journal of Chemical Engineering of Japan* 5.4 (1972), pp. 423–424. DOI: 10.1252/jcej.5.423.

[151] Sovová, H. "Breakage and coalescence of drops in a batch stirred vessel—II comparison of model and experiments". In: *Chemical Engineering Science* 36.9 (1981), pp. 1567–1573. DOI: 10.1016/0009-2509(81)85117-2.

[152] Doubliez, L. "The drainage and rupture of a non-foaming liquid film formed upon bubble impact with a free surface". In: *Int. J. Multiphase Flow* 17.6 (1991), pp. 783–803. DOI: 10.1016/0301-9322(91)90056-9.

[153] Duineveld, P. "Bouncing and coalescence of two bubbles in water". PhD thesis. Enschede: University of Twente, 1994. DOI: https://doi.org/10.1007/978-94-011-0938-3_43.

[154] Lehr, F.; Millies, M. and Mewes, D. "Bubble-Size distributions and flow fields in bubble columns". In: *AIChE Journal* 48.11 (2002), pp. 2426–2443. DOI: 10.1002/aic.690481103.

[155] Lehr, F. and Mewes, D. "A transport equation for the interfacial area density applied to bubble columns". In: *Chemical Engineering Science* 56.3 (2001), pp. 1159–1166. DOI: 10.1016/S0009-2509(00)00335-3.

[156] Walter, J. F. and Blanch, H. W. "Bubble break-up in gas—liquid bioreactors: Break-up in turbulent flows". In: *The Chemical Engineering Journal* 32.1 (1986), B7–B17. DOI: 10.1016/0300-9467(86)85011-0.

[157] Hinze, J. O. "Fundamentals of the hydrodynamic mechanism of splitting in dispersion processes". In: *AIChE Journal* 1.3 (1955), pp. 289–295. DOI: 10.1002/aic.690010303.

[158] Liao, Y. and Lucas, D. "A literature review of theoretical models for drop and bubble breakup in turbulent dispersions". In: *Chemical Engineering Science* 64.15 (2009), pp. 3389–3406. DOI: 10.1016/J.CES.2009.04.026.

[159] Coulaloglou, C. and Tavlarides, L. "Description of interaction processes in agitated liquid-liquid dispersions". In: *Chemical Engineering Science* 32.11 (1977), pp. 1289–1297. DOI: 10.1016/0009-2509(77)85023-9.

[160] Batchelor, G. "The effect of homogeneous turbulence on material lines and surfaces". In: *Proceedings of the Royal Society of London. Series A. Mathematical and Physical Sciences* 213.1114 (1952), pp. 349–366. DOI: 10.1098/rspa.1952.0130.

[161] Angelidou, C.; Psimopoulos, M. and Jameson, G. "Size distribution functions of dispersions". In: *Chemical Engineering Science* 34.5 (1979), pp. 671–676. DOI: 10.1016/0009-2509(79)85112-X.

[162] Luo, H. and Svendsen, H. F. "Theoretical model for drop and bubble breakup in turbulent dispersions". In: *AIChE Journal* 42.5 (1996), pp. 1225–1233. DOI: 10.1002/aic.690420505.

[163] Wang, T.; Wang, J. and Jin, Y. "A novel theoretical breakup kernel function for bubbles/droplets in a turbulent flow". In: *Chemical Engineering Science* 58.20 (2003), pp. 4629–4637. DOI: 10.1016/j.ces.2003.07.009.

[164] Narsimhan, G.; Gupta, J. and Ramkrishna, D. "A model for transitional breakage probability of droplets in agitated lean liquid-liquid dispersions". In: *Chemical Engineering Science* 34.2 (1979), pp. 257–265. DOI: 10.1016/0009-2509(79)87013-X.

[165] Tucker III, C. L. and Moldenaers, P. "Microstructural evolution in polymer blends". In: *Annual Review of Fluid Mechanics* 34.1 (2002), pp. 177–210. DOI: 10.1146/annurev.fluid.34.082301.144051.

[166] Fu, X. and Ishii, M. "Two-group interfacial area transport in vertical air–water flow". In: *Nuclear Engineering and Design* 219.2 (2003), pp. 143–168. DOI: 10.1016/S0029-5493(02)00285-6.

[167] Miller, C. and Neogi, P. *Interfacial Phenomena: Equilibrium and Dynamic Effects*. 2nd. CRC Press, 2007. DOI: 10.1201/9781420044430.

[168] Finch, J. A.; Nesset, J. E. and Acuña, C. "Role of frother on bubble production and behaviour in flotation". In: *Minerals Engineering* 21.12-14 (2008), pp. 949–957. DOI: 10.1016/j.mineng.2008.04.006.

[169] Baroud, C. N. "Marangoni Convection". In: *Encyclopedia of Microfluidics and Nanofluidics*. Boston, MA: Springer US, 2013, pp. 1–8. DOI: 10.1007/978-3-642-27758-0{_}852-4.

[170] Tse, K. et al. "Small bubble formation via a coalescence dependent break-up mechanism". In: *Chemical Engineering Science* 58.2 (2003), pp. 275–286. DOI: 10.1016/S0009-2509(02)00528-6.

[171] Zhang, F. H. and Thoroddsen, S. T. "Satellite generation during bubble coalescence". In: *Physics of Fluids* 20.2 (2008), p. 022104. DOI: 10.1063/1.2835664.

[172] Laurén, S. *What are surfactants and how do they work?* 2018. URL: https://www.biolinscientific.com/blog/what-are-surfactants-and-how-do-they-work.

[173] Basařová, P. and Zedníková, M. "Effect of Surfactants on Bubble-Particle Interactions". In: *Surfactants and Detergents*. IntechOpen, 2019. DOI: 10.5772/intechopen.85436.

[174] Loubière, K. and Hébrard, G. "Influence of liquid surface tension (surfactants) on bubble formation at rigid and flexible orifices". In: *Chemical Engineering and Processing: Process Intensification* 43.11 (2004), pp. 1361–1369. DOI: 10.1016/j.cep.2004.03.009.

[175] Dai, B. and Leal, L. G. "The mechanism of surfactant effects on drop coalescence". In: *Physics of Fluids* 20.4 (2008), p. 040802. DOI: 10.1063/1.2911700.

[176] Lu, J. et al. "Coalescence of small bubbles with surfactants". In: *Chemical Engineering Science* 196 (2019), pp. 493–500. DOI: 10.1016/j.ces.2018.11.002.

[177] Bergeron, V. "Forces and structure in thin liquid soap films". In: *Journal of Physics: Condensed Matter* 11.19 (1999), R215–R238. DOI: 10.1088/0953-8984/11/19/201.

[178] Stubenrauch, C. and Klitzing, R. v. "Disjoining pressure in thin liquid foam and emulsion films—new concepts and perspectives". In: *Journal of Physics: Condensed Matter* 15.27 (2003), R1197–R1232. DOI: 10.1088/0953-8984/15/27/201.

[179] Damodaran, S. "Protein Stabilization of Emulsions and Foams". In: *Journal of Food Science* 70.3 (2006), R54–R66. DOI: 10.1111/j.1365-2621.2005.tb07150.x.

[180] Takagi, S. and Matsumoto, Y. "Surfactant Effects on Bubble Motion and Bubbly Flows". In: *Annual Review of Fluid Mechanics* 43.1 (2011), pp. 615–636. DOI: 10.1146/annurev-fluid-122109-160756.

[181] Jávor, Z.; Schreithofer, N. and Heiskanen, K. "Multi-scale analysis of the effect of surfactants on bubble properties". In: *Minerals Engineering* 99 (2016), pp. 170–178. DOI: 10.1016/j.mineng.2016.09.026.

[182] Zhang, W. et al. "Characterizing Frothers through Critical Coalescence Concentration (CCC)95-Hydrophile-Lipophile Balance (HLB) Relationship". In: *Minerals* 2.3 (2012), pp. 208–227. DOI: 10.3390/min2030208.

[183] Vasconcelos, D.; Silva, A. and Barata, J. "Comparison of Commercial and Open-Source CFD Solvers on Surface Tension Dominated Flows". In: *International Conference on Liquid Atomization and Spray Systems (ICLASS)* 1.1 (2021). DOI: 10.2218/iclass.2021.5981.

[184] Saidi, M. et al. "Comparison between Lagrangian and Eulerian approaches in predicting motion of micron-sized particles in laminar flows". In: *Atmospheric Environment* 89 (2014), pp. 199–206. DOI: 10.1016/j.atmosenv.2014.01.069.

[185] Popinet, S. "Numerical Models of Surface Tension". In: *Annual Review of Fluid Mechanics* 50.1 (2018), pp. 49–75. DOI: 10.1146/annurev-fluid-122316-045034.

[186] Scardovelli, R. and Zaleski, S. "Direct numerical simulation of free-surface and interfacial flow". In: *Annual Review of Fluid Mechanics* 31.1 (1999), pp. 567–603. DOI: 10.1146/annurev.fluid.31.1.567.

[187] Sussman, M.; Smereka, P. and Osher, S. "A Level Set Approach for Computing Solutions to Incompressible Two-Phase Flow". In: *Journal of Computational Physics* 114.1 (1994), pp. 146–159. DOI: 10.1006/jcph.1994.1155.

[188] Sethian, J. A. and Smereka, P. "Level Set Methods for Fluid Interfaces". In: *Annual Review of Fluid Mechanics* 35.1 (2003), pp. 341–372. DOI: 10.1146/annurev.fluid.35.101101.161105.

[189] Anderson, D. M.; McFadden, G. B. and Wheeler, A. A. "Diffuse-interface methods in fluid mechanics". In: *Annual Review of Fluid Mechanics* 30.1 (1998), pp. 139–165. DOI: 10.1146/annurev.fluid.30.1.139.

[190] Gueyffier, D. et al. "Volume-of-Fluid Interface Tracking with Smoothed Surface Stress Methods for Three-Dimensional Flows". In: *Journal of Computational Physics* 152.2 (1999), pp. 423–456. DOI: 10.1006/jcph.1998.6168.

[191] Desjardins, O.; Moureau, V. and Pitsch, H. "An accurate conservative level set/ghost fluid method for simulating turbulent atomization". In: *Journal of Computational Physics* 227.18 (2008), pp. 8395–8416. DOI: 10.1016/j.jcp.2008.05.027.

[192] Xiao, F.; Ii, S. and Chen, C. "Revisit to the THINC scheme: A simple algebraic VOF algorithm". In: *Journal of Computational Physics* 230.19 (2011), pp. 7086–7092. DOI: 10.1016/j.jcp.2011.06.012.

[193] Sussman, M. and Puckett, E. G. "A Coupled Level Set and Volume-of-Fluid Method for Computing 3D and Axisymmetric Incompressible Two-Phase Flows". In: *Journal of Computational Physics* 162.2 (2000), pp. 301–337. DOI: 10.1006/jcph.2000.6537.

[194] Hirt, C. and Nichols, B. "Volume of fluid (VOF) method for the dynamics of free boundaries". In: *Journal of Computational Physics* 39.1 (1981), pp. 201–225. DOI: 10.1016/0021-9991(81)90145-5.

[195] Wang, Z.; Yang, J. and Stern, F. "A new volume-of-fluid method with a constructed distance function on general structured grids". In: *Journal of Computational Physics* 231.9 (2012), pp. 3703–3722. DOI: 10.1016/j.jcp.2012.01.022.

[196] Noh, W. and Woodward, P. *SLIC (simple line interface calculation). [Usable in 1, 2, or 3 space dimensions]*. Tech. rep. Livermore, CA: Lawrence Livermore National Laboratory (LLNL), 1976. DOI: 10.2172/7261651.

[197] Katopodes, N. D. "Level Set Method". In: *Free-Surface Flow*. Elsevier, 2019, pp. 804–828. DOI: 10.1016/B978-0-12-815485-4.00019-X.

[198] Osher, S. and Sethian, J. A. "Fronts propagating with curvature-dependent speed: Algorithms based on Hamilton-Jacobi formulations". In: *Journal of Computational Physics* 79.1 (1988), pp. 12–49. DOI: 10.1016/0021-9991(88)90002-2.

[199] Joshi, J. B. et al. "Computational fluid dynamics". In: *Advances of Computational Fluid Dynamics in Nuclear Reactor Design and Safety Assessment*. Elsevier, 2019, pp. 21–238. DOI: 10.1016/B978-0-08-102337-2.00002-X.

[200] Yang, X. et al. "An adaptive coupled level-set/volume-of-fluid interface capturing method for unstructured triangular grids". In: *Journal of Computational Physics* 217.2 (2006), pp. 364–394. DOI: 10.1016/j.jcp.2006.01.007.

[201] Zeneli, M. et al. "Numerical methods for solid-liquid phase-change problems". In: *Ultra-High Temperature Thermal Energy Storage, Transfer and Conversion*. Elsevier, 2021, pp. 165–199. DOI: 10.1016/B978-0-12-819955-8.00007-7.

[202] Luo, K. et al. "Level set method for atomization and evaporation simulations". In: *Progress in Energy and Combustion Science* 73 (2019), pp. 65–94. DOI: 10.1016/j.pecs.2019.03.001.

[203] Meng, W. et al. "An enhanced CLSVOF method with an algebraic second-reconstruction step for simulating incompressible two-phase flows". In: *Int. J. Multiphase Flow* 154 (2022), p. 104151. DOI: 10.1016/j.ijmultiphaseflow.2022.104151.